

LOW OPTICAL SIGNAL DETECTION IN
BIOLOGICAL MATERIALS: SNR
CONSIDERATIONS AND NOVEL
TECHNIQUES

Thesis by

Emily Jayne McDowell

In Partial Fulfillment of the Requirements for the

Degree of

Doctor of Philosophy

CALIFORNIA INSTITUTE OF TECHNOLOGY

Pasadena, California

2010

(Defended October 9, 2009)

© 2010

Emily Jayne McDowell

All Rights Reserved

Acknowledgements

I am so incredibly grateful to my advisor, Changhuei Yang. I would not have come close to completing this body of work without his guidance and support. Yang's enthusiasm and passion for our work are contagious, and importantly, he has always been ready with a pep talk when I needed one. Yang has helped me grow as both a researcher and as a person, and I am indebted to him for his patience, motivation, and understanding.

No research is done in isolation, particularly not experimental work. I am appreciative for the camaraderie, teamwork, and support of my research group, both past and present: Jigang Wu, Meng Cui, Xiquan Cui, Lapman Lee, Jian Ren, Guoan Zheng, Sean Pang, Yin Min Wang, Zahid Yaqoob, Marinko Sarunic, Vahan Senekerimyan, and Xin Heng. Our group could not function on a daily basis without our incredibly helpful administrative assistants and lab managers: Anne Sullivan, Agnes Tong, Christine Garske, and Yayun Lui. Additionally, collaborators Snow Tseng and Ivo Vellekoop have provided extremely useful advice and insights.

Although it has been 4 years, I would not have reached this goal without the support of my undergraduate research group headed by Joseph Izatt. His group introduced me to biomedical optics, helped me grow confident in my abilities as a researcher, and introduced me to Yang. Thanks to Mike Choma, Audrey Ellerbee, Marinko Sarunic, and Brian Applegate. Special thanks to Marinko for answering all of the questions that I thought were too stupid to ask as a new graduate student.

I'd also like to acknowledge my thesis committee including Scott Fraser, Rob Phillips, and John Dabiri. I greatly appreciate the time taken from your busy lives to listen and ask thoughtful questions. I'm particularly grateful to John Dabiri for giving me the opportunity to TA Ae104 for the past two years. John has kept me well paid, and has been a great source of advice on all things, both academic and life-related.

Caltech proved to be a much more fun experience than I could ever have predicted. I couldn't have survived on a day-to-day basis without my roommates Andrew Tchieu, Jeff Hanna, Kakani Young, and Won Tae Joe. Thank you so much for helping me keep things in perspective and distracting me often. I'm also grateful to my boyfriend, Chris Kovalchick, for sharing the everyday ups and downs of grad school and always making sure to plan an 'up' on weeks full of 'downs'.

My Duke girlfriends receive an extra special thanks for making sure that there was always an interesting email in my inbox when I arrived in lab every morning.

I'm grateful to my family, for supporting and encouraging me along this journey. Mom and Dad, thank you for being so confident that I could do anything I set my mind to, for funding everything I set my mind to, and for reminding me to make sure to have some fun along the way. I'm sorry I had to move so far away to do it. Ruth and Kettie, I will enjoy the next four years of being the only doctor in the family, but will be happy when you both join me. Graby, I think your prayers have paid off. Thank you so much. I love you.

Finally, I'd like to acknowledge funding from a Caltech first year fellowship, an NIH Ruth L. Kirschstein national research service award fellowship, and an NSF graduate research fellowship.

Abstract

Light scattering poses significant challenges for biomedical optical imaging techniques. Diffuse scattering scrambles wavefront information, confounding easy analysis of signals reflected from or transmitted through biological tissues. For optical imaging techniques that employ only unscattered light components, the penetration depth is severely limited. In this thesis, we develop and discuss two general methods for dealing with large levels of light scattering in tissue. The first involves optimization of the signal-to-noise ratio (SNR) of coherence domain optical tomography techniques. The majority of the signal measured in these techniques is singly scattered. Thus, an improvement in SNR will improve the penetration depth of the system by picking out the weak signal contribution from increasing depths that would otherwise be buried in noise. We show that the SNR can be optimized in terms of image reconstruction algorithms, and in terms of detection parameters. An important detection parameter, the integration time, determines the dominant noise source of the measurement, and can be varied to obtain the maximal SNR. A second general method that will be discussed involves the time-reversal of scattered light components in tissues through the process of optical phase conjugation (OPC). OPC has long been used to remove optical aberrations and distortions, but has never before been applied to light scattering in tissues. We show that we are capable of time reversing light scattering in both chicken tissue sections and tissue phantoms, and characterize both the amplitude and resolution trends of the process. Finally, we provide the first successful results of OPC in living tissues.

Table of Contents

Acknowledgements	iii
Abstract.....	vi
Table of Contents	vii
List of Figures.....	xiii
List of Tables	xvi
Abbreviations	xvii
Chapter 1. Introduction.....	1
1.1 Advantages and Challenges Associated with Optical Imaging.....	1
1.2 Optical Properties of Tissues	2
1.2.1 Absorption.....	2
1.2.2 Scattering.....	4
1.2.3 Scattering Regimes	6
1.2.4 Relative Strength and Values.....	7
1.3 Typical Methods to Deal with Light Scattering	8
1.3.1 Gating Methods.....	8
1.3.2 Diffuse Optical Methods.....	10
1.4 Goals and Layout of the Thesis	11
Chapter 2. Coherence Domain Imaging Systems.....	13
2.1 Optical Coherence Tomography.....	13
2.1.1 Time Domain OCT	13

2.1.2 Fourier Domain OCT	16
2.2 Common Noise Sources and SNR Optimization.....	18
2.3 Extensions of Traditional OCT	20
Chapter 3. Algorithms for Optimizing SNR	22
3.1 Introduction.....	22
3.2 3x3 Homodyne OCT Theory	25
3.3 Theoretical SNR Corresponding to Image Reconstruction Algorithms.....	26
3.3.1 Optimal SNR in Common Interferometric Topologies	28
3.3.2 Method 1.....	32
3.3.3 Method 2.....	32
3.3.4 Method 3.....	33
3.3.5 Methods 4 and 5	35
3.4 Experimental Methods	38
3.5 Results and Discussion.....	39
3.5.1 Experimental SNR Results.....	39
3.5.2 Imaging Results.....	40
3.5.3 Robustness to Phase Error.....	43
3.6 Conclusions.....	44
Chapter 4. Modeling the Effects of 1/f noise	46
4.1 Introduction.....	46
4.2 Theoretical Noise Model	48

4.2.1 Choice of f_{min}	52
4.2.2 Influence of the Noise Exponent, α	54
4.3 Experimental Methods.....	58
4.4 Results and Discussion.....	61
4.4.1 Measured Power Spectrum.....	61
4.4.2 Experimental SNR Versus Integration Time	61
4.4.3 Characteristic Time.....	64
4.4.4 1/f Noise Power Dependence	65
4.4.5 Sources of 1/f Noise.....	66
4.5 Conclusions	67
Chapter 5. Dark 1/f Noise in Direct Detection Schemes.....	70
5.1 Introduction	70
5.2 Background	73
5.3 Problem Statement	75
5.4 Experimental Verification.....	77
5.5 Theory	78
5.6 Results	83
5.7 Discussion	85
5.7.1 Summary of Analysis.....	85
5.7.2 Application of Analysis	86
5.8 Conclusions	88

Chapter 6. 1/f Noise in FDOCT	90
6.1 Introduction.....	90
6.2 SNR of M-mode Data.....	92
6.3 SNR of FDOCT Images	96
6.4 Conclusions.....	98
Chapter 7. Turbidity Suppression Through Optical Phase Conjugation	99
7.1 Optical Phase Conjugation	99
7.1.1 OPC Based on Static Holography.....	100
7.1.2 OPC Based on Dynamic Holography Through Degenerate Four-Wave Mixing	103
7.2 Previous Work.....	104
Chapter 8. TSOPC System Characterization.....	107
8.1 Introduction.....	107
8.2 Materials and Methods	109
8.3 Results.....	112
8.3.1 Chicken Breast Tissue Experiments	112
8.3.2 Tissue Phantom Experiments.....	115
8.3.3 Resolution Trends	116
8.4 Discussion.....	118
8.4.1 Amplitude Trends in Tissue Samples	118
8.4.2 Amplitude Trends in Tissue Phantoms.....	120
8.4.3 Origins of Amplitude Trends	120

8.4.4 Resolution Trends	124
8.4.5 Significance and Future work.....	126
8.5 Conclusions	127
Chapter 9. TSOPC in Living Tissues.....	128
9.1 Introduction	129
9.2 Experimental Methods	130
9.3 Results and Discussion.....	132
9.4 Conclusions	136
Chapter 10. Potential Applications and Future Work for TSOPC	137
10.1 Potential Applications	137
10.1.1 Light Concentrating Applications	137
10.1.2 Absorption Amplification Applications	139
10.1.3 Wavelength Tuning for Light Selection.....	140
10.2 Future Work	142
Chapter 11. Conclusions	144
References	145
Appendix D1: Chapter 3 Derivations	155
D1.1 Derivation of Variance for Heterodyne Detection	155
D1.2 Derivation of Variance for Heterodyne Detection with Phase Knowledge	156
D1.3 Derivation of Variance for Method 1	157
D1.4 Derivation of Variance for Method 2	157

D1.5 Derivation of Variance for Method 3.....	158
D1.6 Derivation of Variance for Method 3, n Ports	158
D1.7 Derivation of Variance for Methods 4 and 5	159
Appendix D2: Chapter 8 Derivation and Model.....	160

List of Figures

Number	Page
1.1 Therapeutic window in the optical absorption spectrum of tissue components.....	3
1.2 Time-resolved light scattering in tissues.....	4
2.1 Time domain OCT	14
2.2 Spectrometer-based Fourier domain OCT.....	17
2.3 SNR as a function of reference arm reflectivity.....	19
3.1 3x3 fiber-coupler-based homodyne optical coherence tomography	25
3.2 2x2 (50/50) interferometric setups.....	28
3.3 Reconstructed signals from an attenuated mirror.....	39
3.4 Reconstructed images of a highly attenuated Air Force target.....	40
3.5 Reconstructed images of a <i>Xenopus laevis</i> tadpole	42
3.6 SNR versus phase error	43
4.1 Influence of the total time frame, T, of an experiment	53
4.2 Theoretical noise standard deviation versus integration time.....	55
4.3 Theoretical SNR versus integration time	56
4.4 τ dependence of 1/f noise variance	58
4.5 Power spectrum of interferometric noise	61
4.6 Experimental SNR versus integration time	62
4.7 Homodyne vs. heterodyne SNR.....	63
4.8 1/f noise Amplitude.....	65

4.9 Power spectra and SNR for two types of detectors.....	67
5.1 A comparison of the measurement scenarios in Chapters 3 and 4	76
5.2 Power spectral density of the dark noise count of an APD.....	77
5.3 SNR versus integration time for a combination of white and 1/f noise.....	83
5.4 Dependence of τ_{opt} on the relative amplitudes of white and 1/f noise	84
6.1 System schematic for common path FDOCT	92
6.2 Power spectrum of the system noise.....	93
6.3 M-mode SNR as a function of time	95
6.4 Image SNR as a function of integration time.....	97
7.1 A conventional mirror compared to a phase conjugate mirror	100
7.2 OPC through static holography.....	101
7.3 Proof-of-concept TSOPC experiment.....	105
8.1 TSOPC system schematic.....	111
8.2 Chicken tissue samples	112
8.3 Experimental TSOPC amplitude data in chicken tissue samples	114
8.4 Experimental TSOPC amplitude data in tissues phantoms.....	115
8.5 Focused beam sample arm geometry	116
8.6 Resolution trends for chicken tissue samples	117
8.7 Resolution trends for tissue phantoms	118
8.8 Model fits for both chicken tissue and tissue phantom data	124
9.1 The ear of a New Zealand rabbit mounted in the TSOPC system.....	131
9.2 Reconstructed spots through living and dead rabbit tissue, and a tissue	

phantom of comparable properties.....	132
9.3 TSOPC signal versus sample displacement during playback.....	133
9.4 Histology of the rabbit ear	134
9.5 Signal decay through the rabbit tissue	135
10.1 Diagram depicting potential light concentrating experiments.....	137
10.2 Diagram depicting potential absorption amplification experiments.....	139
10.3 Diagram depicting wavelength tuning experiments	141
10.3 A potential experimental implementation of a reflection mode TSOPC system.....	142

List of Tables

Number	Page
1.1 Scattering and absorption properties of tissues.....	7
3.1 Comparison of theoretical and experimental reconstruction results.....	37
5.1 A comparison of the important equations in Chapters 4 and 5.....	86

Abbreviations

APD	Avalanche photodiode
CCD	Charge-coupled device
DFWM	Degenerate four-wave mixing
FDOCT	Fourier domain optical coherence tomography
FWHM	Full-width at half-maximum
FWM	Four-wave mixing
NA	Numerical aperture
OCT	Optical coherence tomography
OPC	Optical phase conjugation
PMT	Photomultiplier tube
PrC	Photorefractive crystal
PSD	Power spectral density
sFDOCT	Spectrometer-based Fourier domain optical coherence tomography
SLD	Superluminescent diode
SLM	Spatial light modulator
SNR	Signal-to-noise ratio
TDOCT	Time domain optical coherence tomography
TSOPC	Turbidity suppression through optical phase conjugation

Chapter 1. Introduction

1.1 Advantages and Challenges Associated with Optical Imaging

Optical methods are uniquely suited to biological imaging for several distinct reasons. The non-contact nature of light delivery provides for an extremely non-invasive and non-destructive imaging modality that can be implemented at relatively low cost. Second, optical techniques are generally capable of providing resolution on the order of the wavelength of light. This provides for high-resolution (sub-micron) cellular and tissue level imaging. Finally, the energy quanta associated with visible and near infrared photons are ideal for interacting with biological molecules. Such molecular interactions provide the basis for techniques including fluorescence, multi-photon microscopy, second harmonic generation, and Raman spectroscopy, allowing for functional or molecule-specific imaging of biological tissues. Thus, light can provide for non-contact, high-resolution, functional imaging of biological features of interest.

The advantages of optical techniques are accompanied by significant challenges. Some of the above-mentioned techniques rely on a photon being absorbed by a molecule of interest. However, as we will see in the following sections, absorption is dominated in tissues by elastic light scattering. In a biological environment, a photon is hundreds to thousands of times more likely to be scattered than absorbed. This presents a problem for biological imaging, even for optical techniques that rely in part on light scattering for contrast. As photon trajectories become increasingly complicated, it becomes impossible to extract useful information from that photon about where it has been.

1.2 Optical Properties of Tissues

1.2.1 Absorption

Absorption occurs when energy is transferred from light to a molecular species. During this process, the molecular species transitions from a lower to a higher energy level, where the difference in energy between the two levels, ΔE , is equal to the energy of the photon, $h\nu$:

$$h\nu = \Delta E, \quad (1.1)$$

where h is Planck's constant (6.626×10^{-34} J•s), and ν is the optical frequency (light is defined as the portion of the electromagnetic spectrum with frequencies $\nu = c/\lambda = 3 \times 10^{14}$ to 3×10^{15} , where c is the speed of light). From an excited state, the molecular species can release this energy as either heat or in the form of a secondary photon (fluorescence, phosphorescence), or transfer the energy to a neighboring molecule.

Absorption can be quantified through several parameters. For a single type of absorber, the absorption cross section is defined as:

$$P_a = I_0 \sigma_a, \quad (1.2)$$

where P_a is the absorbed power (energy per second) and I_0 is the intensity incident on the absorber (energy per second per area). The absorption cross section, σ_a , is a measure of the area of an incident beam that is absorbed by an absorbing particle, and is generally not equal to the geometric cross section of the particle. If many identical particles exist in an absorbing medium, that medium can be characterized by an absorption coefficient:

$$\mu_a = \rho_a \sigma_a, \quad (1.3)$$

where ρ_a is the number density (number per unit volume) of the absorbers. The absorption coefficient is related to the absorption mean free path, l_a , as:

$$l_a = 1/\mu_a, \quad (1.4)$$

which is a measure of the average distance an individual photon will travel through the medium before being absorbed. The Beer-Lambert law makes use of the absorption coefficient to describe the intensity decay through an absorbing medium (1):

$$I(x) = I_0 \exp(-\mu_a x), \quad (1.5)$$

where I_0 is the intensity at $x=0$.

There are many important absorbers in tissues including water, hemoglobin, melanin, and many others. Figure 1.1 shows the absorption spectrum of some of these important tissue chromophores, as both σ_a and μ_a are functions of wavelength. The majority of optical imaging techniques work in the ‘therapeutic window’ from 600 to 1300 nm (1). This window is bounded by the large absorption of hemoglobin and water on either side. However, within this window, absorption effects are relatively small compared to scattering effects, which we will discuss in the following section. Absorption is diagnostically important for many routine optical techniques such as pulse oximetry and angiography.

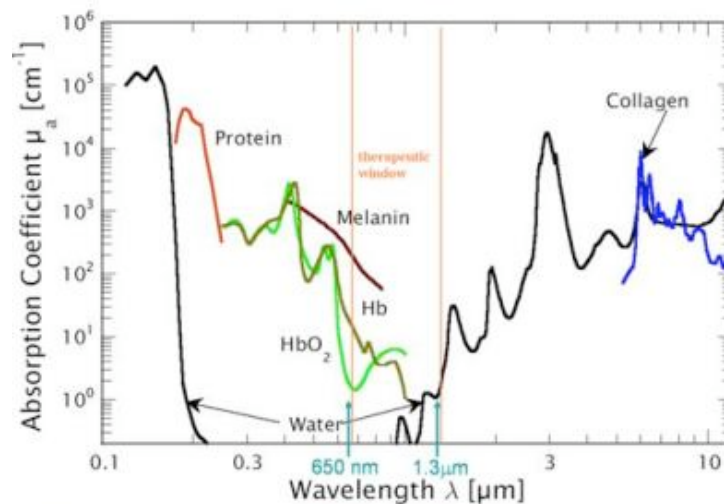


Figure 1.1. Therapeutic window in the optical absorption spectrum of tissue components (Image courtesy of (2))

1.2.2 Scattering

The second major process by which light interacts with tissues is through light scattering. Similar to absorption, a scattering cross section can be defined for a single, spherical scatterer as:

$$P_s = I_0 \sigma_s, \quad (1.6)$$

where P_s is the power of the light that is spatially redirected through scattering. Again, σ_s is not necessarily equal to the geometric cross section of the scatterer. For a uniform medium of particles, a scattering coefficient and mean free path can be defined as in Eqs. 1.3 and 1.4, and Beer's law holds true as well:

$$I_{ballistic}(L) = I_0 \exp(-\rho_s \sigma_s L) = I_0 \exp(-\mu_s L). \quad (1.7)$$

Instead of the total intensity exiting the medium, the left hand side of Eq. 1.7 is a measure of the intensity of the unscattered, or ballistic, light component.

If a pulse of light is incident on a scattering medium or slab of tissue, the exiting photons can be divided into three main components (illustrated in Fig. 1.2). The first to exit the material is the ballistic component, with intensity given by Eq. 1.7. These photons

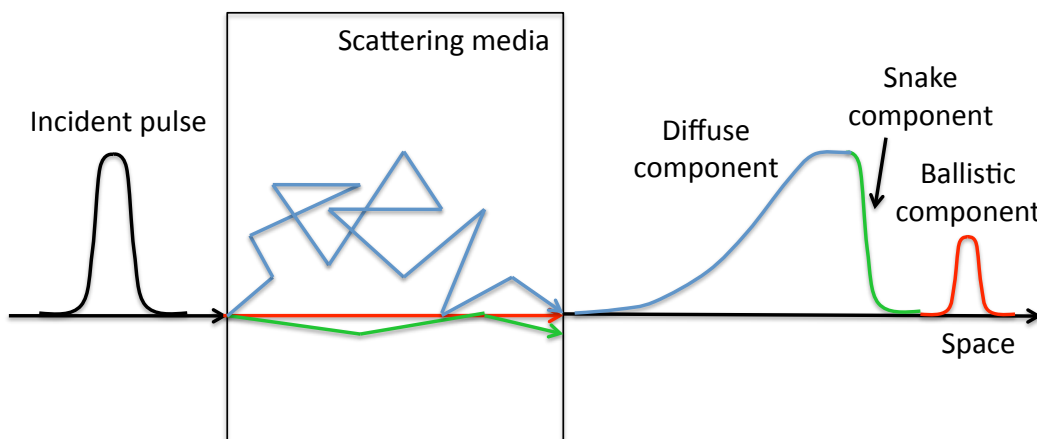


Figure 1.2. Time-resolved light scattering in tissues

have traveled straight through the medium. A second component, consisting of ‘snake’ photons, forward scatter through the medium along an approximately straight path. These are the first of the scattered photons to leave the medium. Finally, the bulk of the light is diffusely scattered, having followed a tortuous path through the medium.

Due to the phenomenon of multiple scattering, Eq. 1.6 cannot be generalized for a medium containing N scatterers except under specific approximations (1). The total power scattered by a scattering media can be written as:

$$P_s = AI_0(1 - \exp(-\mu_s L)) \approx AI_0 \rho_s \sigma_s L = I_0 N \sigma_s, \quad (1.8)$$

only if $\mu_s L \ll 1$. Thus, for a weakly scattering medium, the scattered power is proportional to the number of scatterers. However, when this approximation breaks down, more complicated methods and models must be used to accurately predict the diffuse scattering.

Two types of scattering events are possible (3). The vast majority of scattering events are elastic, meaning that no energy is transferred between the light wave and the particle; the light is simply redirected spatially. Alternatively, for a small fraction of scattering events (1 in 10^6 (1)), inelastic or Raman scattering occurs and the scattered wave undergoes a frequency shift that is specific to the molecular composition of the scatterer. Raman spectroscopy has a wide range of applications through its ability to study molecule-specific vibrational and rotational modes.

A final parameter of interest is the scattering anisotropy factor, g . This factor, defined as the average cosine of the scattering angle ($g = \langle \cos \theta \rangle$), is a measure of the angular spread of scattering distribution. A g value close to 1 implies a high level of forward scattering, while a g value close to 0 corresponds to a nearly isotropic scattering. In general, the scattering anisotropy factor scales with the size of the scattering sphere, such

that scatterers on the order of the wavelength or larger have higher g factors than scatterers smaller than the wavelength, although the parameter also depends on index contrast. Along with the scattering coefficient and cross section, the anisotropy value is a necessary input when light scattering problems are modeled.

1.2.3 Light Scattering Regimes

Light scattering can be generally divided into three classes based on the relative scale of the scattering object with respect to the incident wavelength. The first, and most simple, is the geometric limit, in which case the scattering object is much larger than the incident wavelength. In this case, the scattering cross section is equal to the geometric cross section, and the laws of reflection and refraction are sufficient to characterize the interaction of the object with the optical wave.

A second regime, in which the scatterer is much smaller than the wavelength is termed the Rayleigh limit. In biological tissues, these include membranes and subcellular components. The scattered intensity in this regime can be written in polar coordinates as (1, 3, 4):

$$I(r, \theta) = 8\pi^4 n_m^4 \left(\frac{n_s^2 - n_m^2}{n_s^2 + 2n_m^2} \right) \frac{a^6}{r^2 \lambda^4} (1 + \cos^2 \theta) I_0, \quad (1.9)$$

where n_m and n_s are the refractive indices of the medium and scatterer, respectively, and a is the diameter of the particle. The scattered intensity scales as $1/\lambda^4$. The preferential scattering of shorter wavelengths answers the familiar question of why the sky appears to be blue.

Finally, for spheres of intermediate size, the scattering falls in the Mie regime and is described by Mie theory. Classical methods are used to construct a complete electromagnetic

description of the interaction of an isotropic sphere in a homogeneous medium with a monochromatic plane wave (3). A number of numerical simulation codes have been developed and made available to the public for these types of computations (5). Mie theory is an important tool that has been used, among other applications, to characterize the size of the nucleus as a potential cancer diagnostic (6, 7).

1.2.4 Relative Strength and Values

The following table shows approximate scattering parameters for various types of tissues.

Note that scattering is much stronger than absorption throughout the visible spectrum.

Tissue Type	λ	μ_s (1/cm)	g	μ_a (1/cm)
Stratum Corneum	308	2400	0.9	600
	400	2000	0.9	230
Epidermis	488	600	0.76	50
	800	420	0.85	40
Dermis	488	250	0.76	3.5
	800	175	0.85	2.3
White matter	633	532	0.82	2.2
	1064	469	0.87	3.2
Gray matter	633	354	0.94	2.7
	1064	134	.09	5
Breast — Fatty normal	836	7.27	Not measured	0.11
Breast — Fibrous normal	836	8.1	Not measured	0.05
Breast — Carcinoma	836	9.1	Not measured	0.1

Table 1.1. Scattering and absorption properties of tissues

1.3 Typical Methods to Deal with Light Scattering

Table 1.1 confirms that tissue scattering is quite strong. Thus, imaging through tissues requires effective methods for dealing with light scattering. In both the Mie and Rayleigh regimes, light scatters more strongly at shorter wavelengths. Therefore, one way to minimize scattering is to work at longer wavelengths. There is a limit, however, since Fig. 1.1 shows that water begins to absorb strongly for wavelengths longer than ~ 1300 nm. Two broader strategies will be discussed in this section: gating methods and diffuse optical methods.

1.3.1 Gating Methods

Several optical imaging techniques rely on methods to filter out ‘information bearing’ ballistic or singly scattered photons from the large number of multiply scattered photons that exit the tissue. These include time, directional, and coherence gating (as used in optical coherence tomography). Time gating techniques make use of the fact that ballistic and snake-like photons exit the scattering media at an earlier time than diffuse photons (Fig. 1.2), and can thus be filtered out appropriately. This can be accomplished using fast electronics such as gated optical image intensifiers (8) or holography with femtosecond pulses (9). Additionally, more complex schemes have involved the use of nonlinear optical effects (10, 11) or stimulated Raman scattering (12).

Alternatively, directional gating rejects light whose propagation direction has been sufficiently altered by light scattering. For example, a confocal microscope detects only portions of the transmitted or reflected light that pass through a pinhole. This not only allows for depth selection (since light from planes other than the focal plane will focus to a

different position than the pinhole), but also rejects the bulk of the multiply scattered light. This type of gating technique is not particularly selective to the ballistic component of the light, since the snake-like components travel in approximately the same direction as the ballistic component.

Finally, another commonly used gating method is coherence gating. Coherence is the property of a wave that allows for interference, and can manifest either temporally or spatially. Perfect coherence implies a constant relative phase between two waves, meaning that a perfectly temporally coherent wave is monochromatic. A source with a given spectral bandwidth is said to be partially coherent, since as the waves propagate over time or space, the phase relationship between individual frequencies will change. This is useful in an interferometric setting where a sample beam is interfered with a reference beam. For a partially coherent source, a strong interference signal is only seen when the sample and reference path lengths are exactly matched, and all frequency components are in phase. With the reference path length appropriately set, coherence gating employs a partially coherent light source to select for the light component that has traveled straight through the sample. This topic will be discussed in detail in Chapter 2.

Since the probability of finding ballistic or singly scattered photons decreases exponentially with depth into the sample (Eq. 1.7), these gating techniques suffer from limited penetration depths due to scattering. They rely on systems that operate at very high signal to noise ratios (SNRs) to measure the weak signal contribution from within tissue samples. Even with high SNR, these systems are generally limited to a penetration depth of a few mm at best.

1.3.2 Diffuse Optical Methods

An alternate method for imaging into scattering media involves collecting all of the diffuse photons shown in Fig. 1.2. In these methods, wave effects such as polarization and interference are neglected, and only energy flow through the medium is tracked. Radiation transport theory provides a model to characterize light energy propagation based on three parameters: absorption and scattering coefficients, and a scattering phase function (1). The scattering phase function describes the angular profile of the scattered light. Several approximations exist that are functions of the anisotropy factor, g (13). In the diffusion limit (when absorption is significantly weak), the scattered light disperses in a seemingly random fashion throughout the medium, appearing to take a random walk defined by the diffusion equation. Numerically, these types of computations can also be performed using Monte Carlo methods in which random numbers are drawn from probability distributions, corresponding to average optical properties, to model random walks through a given media (14, 15).

The above methods can be employed for depth resolved imaging through diffuse optical tomography (DOT). This is a difficult endeavor, because it involves solving an ill-posed inverse problem to determine the distribution of the optical properties of a sample based on the measured scattering. Typically a pulse of light enters the sample at a particular source location, and the scattered light is measured at an array of detectors. Then, the source location is moved and the process is repeated. A great deal of information is acquired, and the solution to the forward problem is applied iteratively to an estimate of the sample optical property distribution until the output matches the measured data. Since DOT techniques acquire a large number of photons, they can penetrate deeper in tissues

than the coherence domain techniques mentioned above (several cm at 700 nm (3)). However, in general, DOT is a low-resolution technology with spatial resolution on the order of 20% of the penetration depth (3). DOT has been applied for both breast and brain imaging (16–18), but resolution remains a fundamental limitation.

1.4 Goals and Layout of the Thesis

Taking the above discussion into account, the question remains: how can we optimize optical imaging in biological samples? The work presented in this thesis will describe two main approaches. First, assuming nothing can be done about strong scattering, we can optimize our systems to run with a high signal-to-noise ratio (SNR), making it easier to pick up the weak signal contribution from light that has scattered deep within the sample. Since most of the systems that we will discuss in terms of optimization fall into the category of coherence domain systems, the following chapter will provide background materials on coherence domain imaging. Chapters 3, 4, and 5 include experiments and results that are adapted from published manuscripts, while Chapter 6 is adapted from an as-of-yet unpublished manuscript. Chapter 3 describes SNR optimization based on image processing algorithms for an interferometric system based on the phase shifts inherent to a 3x3 fiber coupler. Chapter 4 discusses the impact of 1/f noise on the same system, and develops a generalized model that accounts for the effects of 1/f noise with the goal of allowing a user to select appropriate operating parameters to achieve optimal SNR. Chapter 5 discusses the adaptation of that model to direct detection schemes, and finally Chapter 6 discusses its application for Fourier domain optical coherence tomography (FDOCT).

The thesis changes directions in Chapter 7 to discuss a second approach for optimizing optical imaging, a novel technique termed turbidity suppression through optical phase conjugation (TSOPC). Through this technique, we attempt to time reverse the process of elastic light scattering in order to recover information about the incident wave. Chapter 7 serves as background for the remainder of the thesis, describing the fundamentals of phase conjugation as well as preliminary work in applying phase conjugation to biological tissues. Chapter 8 is a stand-alone manuscript that has been submitted for publication, which describes a detailed characterization of the TSOPC experiment in terms of amplitude and resolution trends. Chapter 9 discusses a set of results concerning TSOPC in living tissues. Chapter 10 discusses the potential value of our work on TSOPC in terms of biomedical applications. Finally, Chapter 11 will draw brief conclusions based on the entire body of work presented in this thesis.

Chapter 2. Background on Coherence Domain Imaging Systems

This chapter is intended to provide background information for Chapters 3–6, as several of the systems that will be discussed fall into the category of coherence domain imaging systems.

2.1 Optical Coherence Tomography

2.1.1 Time Domain OCT

Optical coherence tomography (OCT) is an increasingly popular imaging modality capable of non-invasively providing depth-resolved images of biological structures with micron-scale resolution in real time (19). OCT is a form of low coherence interferometry, which is based on coherence gating (as briefly described in Section 1.3.1).

A standard, fiber-based, Michelson-type interferometer is depicted in Fig. 2.1(a). Light entering the interferometer is split into two optical paths at a fiber coupler (the fiber equivalent of a beamsplitter). One light path reflects off of a mirror, while the other probes the sample. The two returning light fields are then recombined and interfere at a photodetector. In a time domain implementation of OCT, the reference arm is scanned in time. Let us, for a moment, discuss the detected signal for the case with a mirror as the sample, and a monochromatic light source. In this case, as the reference arm is scanned, the two beams alternately constructively and destructively interfere to form a fringe pattern. The detected interferometric signal can be written as:

$$P_{detected} = P_S + P_R + 2\sqrt{P_S P_R} \cos(2k(x_S - x_R)), \quad (2.1)$$

where P_S and P_R are the powers returning from the sample and reference arm, respectively, k is the wavenumber of the light source ($k=2\pi/\lambda$), and x_S and x_R are the length of the sample and reference arms, respectively.

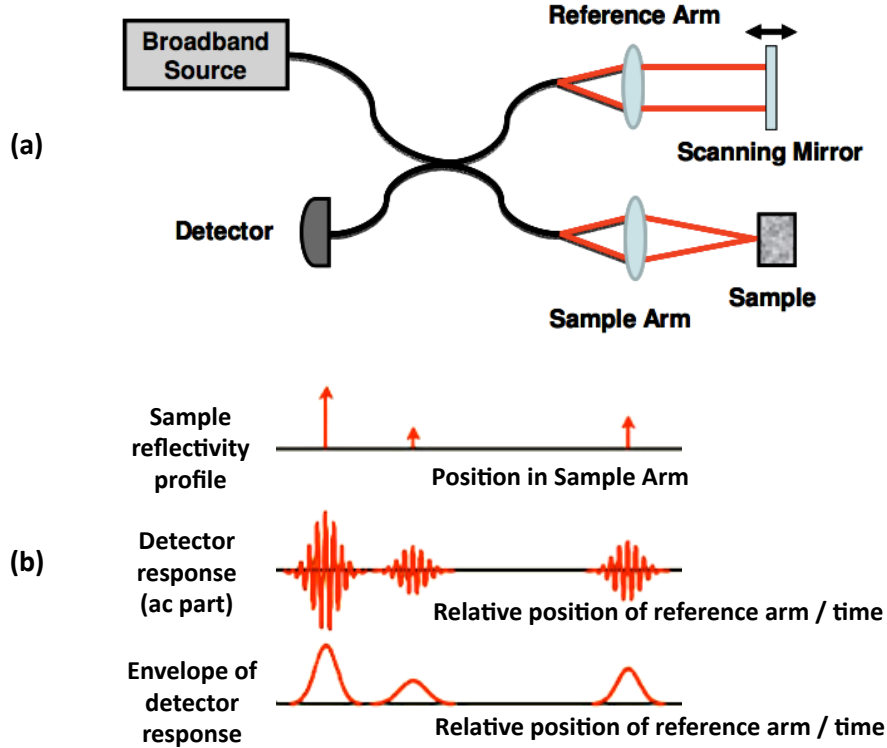


Figure 2.1. Time domain OCT. a) system schematic. b) diagram of detected signals

In the case of a low coherence light source, a strong interference signal is only seen when the reference path length is matched with the position of a sample reflector. This is the only geometry in which all of the wavelengths are guaranteed to interfere constructively with each other. The above equation is modified as follows (20):

$$P_{detected} = P_S + P_R + 2\sqrt{P_S P_R} \exp\left(-\left(\frac{x_S - x_R}{l_c / (2\sqrt{\ln(2)})}\right)^2\right) \cos(2k_0(x_S - x_R)), \quad (2.2)$$

where, again, P_S and P_R are the powers returning from the sample and reference arm, respectively, k_0 is the center wavenumber of the broadband source, and l_c is the coherence length of the light source. The value of P_S is proportional to the reflectivity of the sample reflector, R_S ($P_S = P_{in} R_S$). According to the above equation, as the reference mirror is scanned, a burst of fringes is detected with amplitude corresponding to the reflectivity of each sample reflector (Fig. 2.1(b)). These fringe bursts are then demodulated and subsequent laterally-displaced depth scans are stacked to form an image.

Only backscattered sample light that has traveled a distance within a coherence length of light returning from the reference arm will interfere. Therefore, the coherence length of the light source sets the axial resolution of the imaging system. The coherence length is inversely proportional to the bandwidth of the light source as follows (20, 21):

$$l_c = \frac{2 \ln(2) \lambda_0^2}{\pi \Delta \lambda_{fwhm}} = \frac{4 \ln(2)}{\Delta k_{fwhm}}, \quad (2.3)$$

where λ_0 is the source center wavelength, and $\Delta \lambda_{fwhm}$ and Δk_{fwhm} give the bandwidth of the light source in terms of its full-width at half-maximum (FWHM). Note that this expression assumes a Gaussian source profile. A heavily researched area in recent years has been the development of increasingly broad light sources for superior axial resolution. In OCT systems, the axial resolution is decoupled from the lateral resolution, which is determined by the optics used in the sample arm. The minimum focused beam size incident on the sample is given by:

$$w_0 = 1.22 \frac{\lambda}{2NA} = 1.22 \frac{f\lambda}{D}, \quad (2.4)$$

where NA is the numerical aperture of the focusing and collection optics, f is the focal length, and D is the diameter of the collimated beam that is focused onto the sample. The spot size varies with depth into sample as follows:

$$w(\Delta z) = w_0 \sqrt{1 + \left(\frac{\lambda_0 \Delta z}{\pi w_0^2} \right)^2}, \quad (2.5)$$

where Δz is the axial distance from the minimum beam waist. A relatively low level of focusing is typically employed to limit beam divergence throughout the imaging depth.

If the reference arm in a TDOCT system is capable of moving to any arbitrary distance, then the maximum imaging depth is limited by scattering based on the SNR of the system. The SNR of these types of systems will be discussed in detail in Section 2.1.3.

2.1.2 Fourier Domain OCT

Within the last 10 years, the OCT community realized that there is an alternate way of acquiring the same information. Fourier domain implementations of OCT (FDOCT) sample the interference pattern as a function of wavenumber (k), with a fixed reference path length. A depth scan into the sample is then obtained by Fourier transformation. This can be accomplished in two ways. Spectrometer-based FDOCT systems utilize a spectrometer to spectrally disperse light in the detection arm of the interferometer over a CCD (Fig. 2.2(a)). Alternately, swept source FDOCT systems use a wavelength swept laser source, such that the spectral interferogram is obtained at a single photodetector as a function of time. Spectral encoding can be described in a form similar to Eq. 2.2 as:

$$P_{detected}(k) = \rho S(k) \left[R_S + R_R + 2\sqrt{R_S R_R} \cos(2k(x_S - x_R)) \right] \quad (2.6)$$

where ρ is the detector efficiency (typically assumed to be uniform across k) and $S(k)$ is the source power spectral density in units of watts per wavenumber. Thus, the detected signal at the spectrometer is the source spectrum modulated by interference fringes as shown in Fig. 2.2(b). Fourier transformation of this spectrum results in the same depth scan found after demodulation of the detected TDOCT signals. A Fourier domain implementation is not only advantageous due to the fact that it does not require a moving reference arm, but it also provides an SNR advantage (22–24) due to the fact that information is collected from all depths simultaneously (i.e., none of the incident light is wasted).

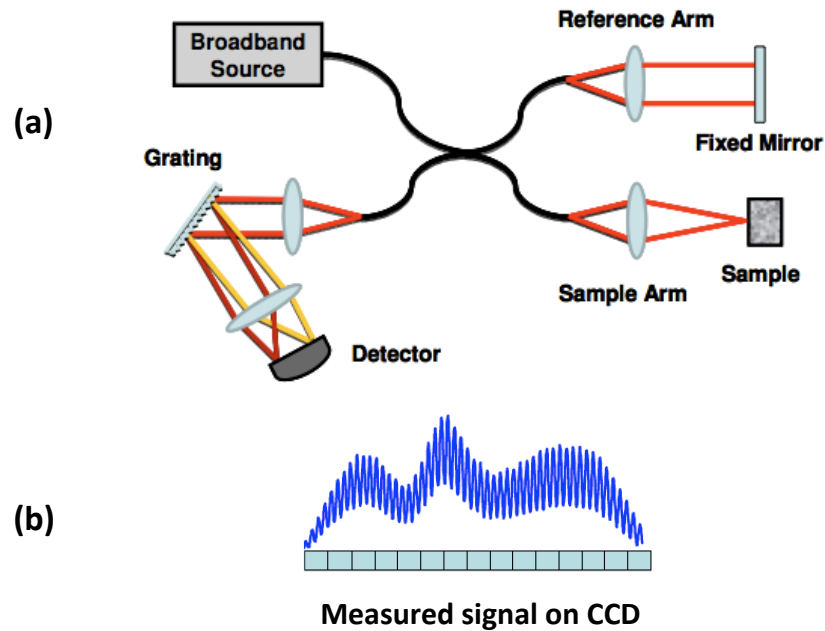


Figure 2.2. Spectrometer-based Fourier domain OCT. a) system schematic. b) detected signal on CCD camera

In FDOCT systems, the maximum imaging depth is fundamentally limited. As mentioned above, the depth scan of the sample is obtained from a Fourier transform of the interferometric portion of the detected signal as a function of wavenumber. The maximum depth is determined by the highest frequency on the spectrum that can be resolved by the

system. For a spectrometer-based system this is a function of the $\delta\lambda$ or δk that corresponds to one spectrometer pixel. For a swept-source system, this is determined by the frequency step that occurs over a single time step.

2.2 Common Noise Sources and SNR Optimization

The maximum detected signal in an OCT system, for a single path-length matched reflector, is given by:

$$P_{\text{detected, max}} = P_S + P_R + 2\sqrt{P_S P_R}. \quad (2.7)$$

The term of interest is the third term, which was the coefficient of the cosine term in Eqs. 2.2 and 2.6. It can be isolated through appropriate subtraction of the DC terms, however noise from these terms will remain. In order to achieve high quality images, we are interested in how the signal term compares to system noise.

The typical noise sources considered in OCT imaging are white noise sources, which include receiver noise, shot noise, and excess intensity noise (25). Receiver noise generally has both white and colored components. The white component is due to Johnson noise in the system circuitry caused by thermal agitation of charge carriers (26, 27). Shot noise is inherent to any beam of light, and is caused by the Poisson distributed arrival time of individual photons. Finally, excess intensity noise is caused by polarization fluctuations in the light source and generally scales with intensity (28). Figure 2.3, from Ref. (25), plots the OCT signal-to-noise ratio (SNR) expected when each of these three noise sources is dominant (inversely proportional to the level of noise). It is typical to optimize OCT systems by adjusting the reference arm power to sit in the shot noise limit. In this case the reference

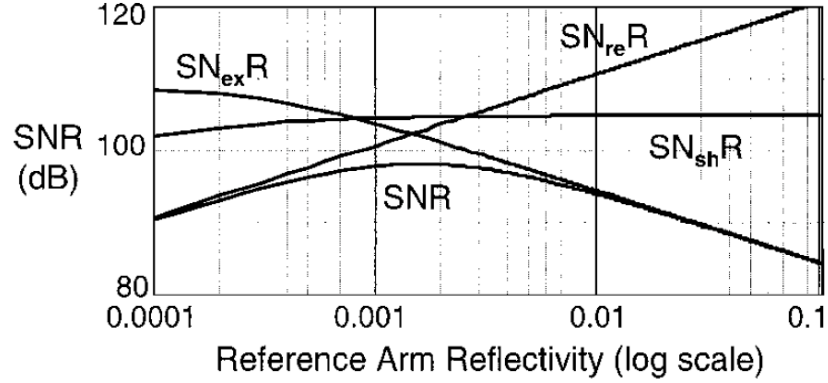


Figure 2.3. SNR as a function of reference arm reflectivity. N_{ex} corresponds to excess intensity noise, N_{re} corresponds to receiver noise, and N_{sh} corresponds to shot noise. This figure is from Rollins et al. (25).

arm power is much greater than the sample arm power, and the dominant term in Eq. 2.7 is the second term, P_R . Since shot noise is a Poisson process, its standard deviation is equal to the square root of its mean. Thus, the standard deviation of the dominant source of shot noise, in terms of number of photons, is given by:

$$\sqrt{\frac{P_R \tau}{h\nu}}, \quad (2.8)$$

where P_R is the detected power returning from the sample arm, τ is the integration time of the detection system, h is Planck's constant, and ν is the optical frequency. Comparing this to our signal we find an SNR given by Eq. 2.9. We note that the convention in the OCT community is to represent SNR as the square of the ratio of signal to noise:

$$SNR_{shot\ noise} = \epsilon \left(\frac{2\tau \sqrt{P_R P_S} / h\nu}{\sqrt{P_R \tau} / h\nu} \right)^2 = \epsilon \frac{4P_S \tau}{h\nu}, \quad (2.9)$$

where ϵ is the quantum efficiency, which describes the efficiency of converting photons to electrons ($\eta \sim 0.5$). Examining Eq. 2.9, we see that to increase the SNR of the system, either the sample arm power or the integration time can be increased. There are obvious

limitations in increasing the power at the sample, since there are standards for living tissue to prevent damage to the sample (29). It is less obvious that there are also limitations on increasing the integration time due to the presence of non-white noise sources, specifically $1/f$ noise. We will discuss the effects of these limitations in the following chapters.

Briefly, the SNR advantage of FDOCT systems stems from the fact that signal is collected from all illuminated depths simultaneously. For a TDOCT system that collects a signal over N depth steps, only a fraction of the light reflected from the sample will be capable of interfering with the reference signal and recorded. This fraction is given by P_s/N , and would serve to reduce the SNR by a factor of N in Eq. 2.8.

2.3 Extensions of Traditional OCT

A number of extensions of traditional OCT have been reported. These include polarization sensitive OCT (30, 31), spectroscopic OCT (32, 33), molecular contrast OCT (34–36), Doppler OCT (37), endoscopic OCT (38, 39), and phase-resolved OCT (40–42).

Here, we will provide a brief conceptual description of a specific extension of OCT that will be discussed extensively in this thesis in the context of noise optimization: 3x3 fiber-coupler based homodyne *en face* OCT. First, the term *en face* refers to imaging in the transverse plane, perpendicular to the imaging beam, as opposed to in depth. *En face* images can be produced from 3D volumetric OCT scans by collecting the data points that correspond to a single depth, or, they can be acquired directly. In the 3x3 system, they will be acquired directly. To produce *en face* scans, we essentially employ a TDOCT system with a stationary reference arm (corresponding to one particular depth plane), and scan the sample in x and y dimensions by steering the sample beam.

A standard TDOCT system is heterodyne in nature. A fringe pattern is produced as the reference arm is scanned, and AC lock-in detection is performed to isolate the envelope of interest. If the reference mirror is stationary, the system is converted to homodyne system, since we no longer acquire full interferometric fringes. The difficulty in performing direct detection of an interferometric signal is that we are unaware of the phase of the signal that we are acquiring, making it impossible to determine the amplitude of the signal through a single measurement. This particular system employs a 3x3 fiber coupler, as the output of the 3 ports are phase shifted 120° from one another. By simultaneously detecting these three signals, we can determine the amplitude of the OCT signal to form an image.

Chapter 3. Algorithms for Optimizing SNR

This chapter is adapted from Ref. (43): E.J. McDowell, M.V. Sarunic, Z. Yaqoob, and C. Yang, 'SNR enhancement through phase dependent signal reconstruction algorithms for phase separated interferometric signals,' Optics Express, 15(16), 10103–10122 (2007).

3.1 Introduction

There are a number of signal acquisition scenarios that involve the measurement of phase separated components, such as quadrature components, that are later recombined in an appropriate manner to extract phase and amplitude information. There are several reported methods by which this extraction can be performed. Interestingly, the choice of signal reconstruction algorithm can have a dramatic impact on the signal-to-noise ratio (SNR) of the resulting image or signal.

Experimental designs in which phase separated components are detected include phase shifting interferometry, optical gyroscopes, harmonic gratings-based free space quadrature interferometers, and 3x3 fiber coupler-based homodyne interferometers. Phase shifting interferometric techniques introduce small phase delays in the form of subwavelength optical path length changes (44, 45). These phase shifted signals can then be used to retrieve phase and amplitude information. In an optical gyroscope, light beams traveling in opposite directions around a rotating path experience slightly different path lengths due to the Sagnac effect (46). The intensity and phase retrieved from the resulting phase shifted signals can be used to determine the rotation rate (47, 48). Harmonically related gratings pairs have recently been demonstrated to be useful in full field quadrature

interferometry (49, 50). In such setups, the interference patterns between various diffraction orders of the two gratings are acquired at multiple detectors. The harmonic relationship between the gratings results in phase separation between the detected signals that is non-trivial. The sensitivity of each of these techniques can benefit by recombining the phase separated components in such a way that the total noise is minimized.

In the case of a 3x3 fiber coupler-based system, the intrinsic, nominally 120°, phase shifts between ports of the fiber coupler can be used to decouple phase and amplitude information (51, 52). These phase shifts arise due to evanescent coupling between fiber waveguides as described by coupled mode theory (53, 54), or more simply for 2x2 and 3x3 fiber couplers through conservation of energy (52). 3x3 fiber coupler-based systems have been employed to construct homodyne *en face* OCT images of biological samples (51) and to remove the complex conjugate ambiguity in swept source OCT images of the ocular anterior segment (55, 56). The simplicity of homodyne systems compared to their heterodyne counterparts is a significant implementation advantage. In addition, a properly performed homodyne experiment can provide a 3 dB improvement in SNR compared to heterodyne techniques (57–59).

Quadrature components are also commonly detected in signal acquisition schemes for other biomedical imaging techniques, such as nuclear magnetic resonance (NMR), magnetic resonance imaging (MRI), and Doppler ultrasound. Like the abovementioned optical techniques, these signals must also be recombined in order to retrieve amplitude and phase information. NMR spectrometers commonly utilize two detectors, acquiring 90° phase shifted signals to allow for improved pulse power efficiency and SNR (60). Likewise, phase shifted signals from multiple coils in MR imaging

systems are combined for phase or amplitude imaging. The MR community is well aware that the SNR of the resulting images is affected by the way the image is reconstructed (61–63). Finally, in Doppler ultrasound systems the real and imaginary parts of the Doppler shift signals are detected in order to determine amplitude and phase, which is necessary to determine Doppler information (64).

In this chapter we will report on the SNR advantage that can be achieved by recombining phase separated signals in an optimal manner. Our goal in each of the reported signal reconstruction algorithms is to determine the amplitude of the signal as accurately as possible. In the process we may or may not determine the phase of the signal as well. That said, we find that methods that make use of the phase information contained in the measurements perform better than those that do not. In Section 3.2 we will describe our 3x3 fiber coupler-based homodyne OCT system. We will then describe five different image reconstruction algorithms in Section 3.3, including two phase-dependent methods. We theoretically determine that these algorithms achieve improved SNR as compared to the other three reconstruction methods, and find that they are capable of achieving comparable SNR to commonly employed heterodyne techniques. Notably, these algorithms are not specific to our 3x3 fiber coupler-based OCT system, but are general techniques applicable for use in signal extraction processing wherever phase separated components are available. In Section 3.4 we will describe our experimental setup. In Section 3.5 we compare our experimentally determined SNR values to those derived in Section 3.3, and discuss the influence of the five methods on reconstructed biological images. Finally, we state our conclusions in Section 3.6.

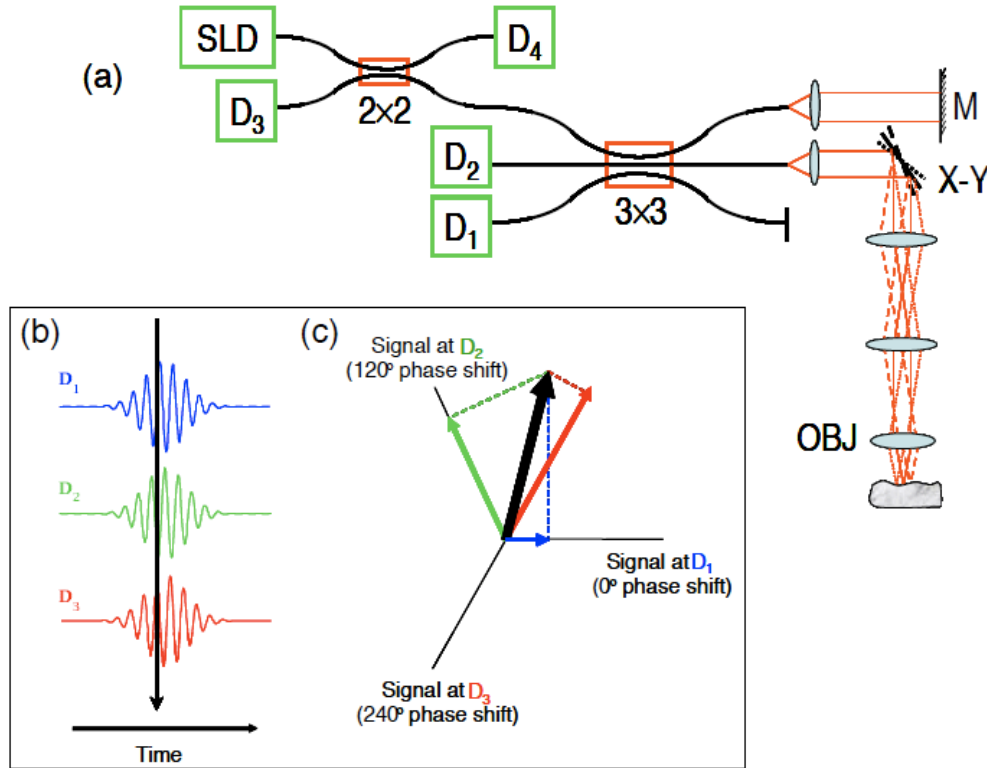


Figure 3.1. 3x3 fiber-coupler-based homodyne optical coherence tomography. a) experimental setup. SLD: superluminescent diode, D_n : nth photodetector, M: mirror, X-Y: x-y scanner, OBJ: 20x microscope objective. b) In this homodyne system the reference mirror (M) is stationary. We can think of the measured signal as a single point (black arrow) on the modulated coherence function that would be obtained if the reference arm was swept. c) These points are the projections of a complex value onto axes separated by 120°.

3.2 3x3 Homodyne OCT Theory

We will first describe the 3x3 homodyne OCT system for high-resolution *en face* imaging of biological samples (following Ref. (51)). This scheme has the ability to decouple amplitude and phase information without the need for complex rapid scanning optical delay mechanisms used in heterodyne systems, or expensive components such as spectrometers or swept laser sources. Figure 3.1(a) shows the experimental setup utilized in this study. Broadband light from an SLD ($\lambda_0=1300$ nm, $\Delta\lambda=85$ nm) enters a 2x2 fiber coupler. Backscattered light from the sample is mixed with reference light to

create an interference pattern at detectors 1–3. Detector 4 is used to monitor and correct for source fluctuations. Figure 3.1(b,c) diagrams the type of data that we are collecting. Using a stationary reference arm, we are essentially measuring a single point on the interferogram (represented by the thick black arrow, Fig. 3.1(b)). Thus, we measure three interferometric signals that can be thought of as the projections of a complex signal onto axes separated by 120° (Fig. 3.1(c)). The optical signal at the j^{th} detector is given by

$$P_j(z) = P_{r,j} + P_{s,j} + 2\left(\frac{1}{s_j}\right)\sqrt{\alpha_{41}\alpha_{4j}\alpha_{51}\alpha_{5j}P_r}\left(\sqrt{P_S(z)} \otimes \gamma(z)\right)\cos(\theta(z) + \varphi_j). \quad (3.1)$$

where $P_{r,j}$ and $P_{s,j}$ represent the total DC power returning from the reference and sample arms, respectively; $1/s_j$ is a scaling factor that accounts for both coupler and detector loss; P_r is the returning reference power; $P_S(z)$ is the returning coherent light from a depth z within the sample; $\gamma(z)$ is the source autocorrelation function; $\theta(z) = 2k_0z + \psi(z)$, is the phase associated with each depth in the sample, where k_0 is the optical wavenumber corresponding to the center wavelength of the source and $\psi(z)$ is the intrinsic reflection phase shift of the sample at depth z ; Finally, φ_j represents the phase shifts between each of the three detectors, attributable to the intrinsic phase shifts of the 3x3 fiber coupler. The signal of interest, which describes the reflectivity profile of the sample, is the coefficient of the cosine term, which can be isolated in several ways following removal of the DC terms. Below we describe several techniques to reconstruct the coefficient of the cosine term.

3.3 Theoretical SNR Corresponding to Image Reconstruction Algorithms

In the following analysis we will determine the theoretical SNR for five different image

reconstruction algorithms. For comparison, we will also derive the SNR corresponding to both optimal and commonly employed homodyne and heterodyne techniques. In each of the following derivations we will make the assumption that the signal at each detection port in terms of number of detected photons, is given by:

$$S_i = \frac{2}{n} \sqrt{P_R P_S} \frac{\varepsilon \tau}{h\nu} \cos(\theta + \varphi_i) \pm N_i, \quad (3.2)$$

where P_R and P_S are the power returning from the reference and sample arms, respectively, n is the number of detection ports ($n \geq 2$), ε is the detector quantum efficiency, τ is the integration time, h is Planck's constant, and ν is the optical frequency. N_i represents a fluctuating noise term that is zero mean, and assumed to be Gaussian distributed with standard deviation as expected given shot noise limited detection:

$$\sigma_{N_i} = \sqrt{\frac{P_r \varepsilon \tau}{nh\nu}}. \quad (3.3)$$

Finally, we assume that the optical power returning from the reference arm is much greater than that returning from the sample arm ($P_R \gg P_S$), which is typical when imaging highly scattering biological samples. In Eq. 3.2 we have assumed that the terms $P_{r,j}$ and $P_{s,j}$ from Eq. 3.1 have been subtracted. This can be accomplished in a practical setting by alternately blocking the sample and reference arms to measure their individual contributions.

In each of these reconstruction methods we wish to isolate a signal that is proportional to the power returning from the sample, P_S . Thus, our goal is to isolate the square of the coefficient of the cosine term in Eq. 3.2. In addition to this signal, we will also determine how the reconstruction method affects both the expected value and standard deviation of the fluctuating noise. These noise parameters are important factors

in image quality. The standard deviation of the noise is related to the SNR, which determines the lowest amplitude features that are visible in the image. The expected, or mean, value of the noise can add a DC shift to the image, thereby affecting the contrast of the image.

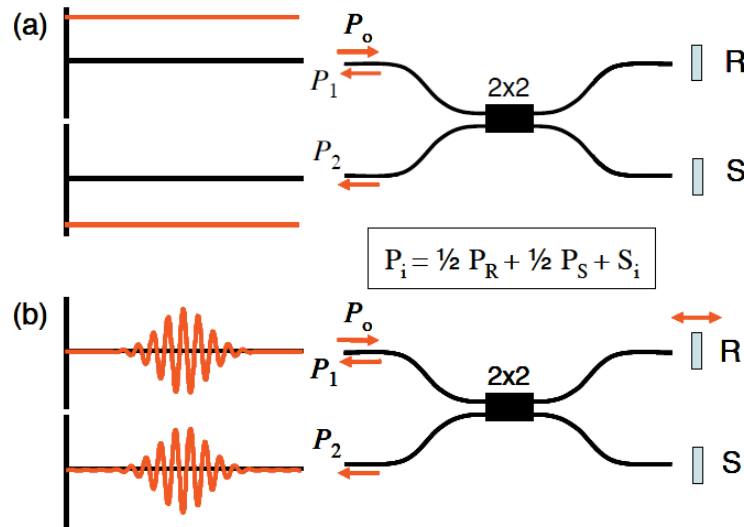


Figure 3.2. 2x2 (50/50) interferometric setups utilizing a) homodyne and b) heterodyne detection. In (a) the reference mirror is stationary, while it is translated in (b). The 180° phase shifts of the fiber coupler are evident in the acquired signals at the two output ports.

3.3.1 Optimal SNR in Common Interferometric Topologies

Here we describe the theoretical SNR corresponding to common interferometric setups. Figure 3.2 shows schematics of the setups that we will examine, which include 2x2 (50/50) fiber coupler-based Michelson interferometers employing a) homodyne and b) heterodyne detection. The signal and noise at each output port of the coupler can be represented by Eqs. 3.2 and 3.3 where $n=2$ to account for the power splitting ratios of the 50/50 fiber coupler.

The upper limit on SNR can be achieved in a homodyne experiment with perfect phase control (57–59). In this type of experiment, the argument of the cosine in Eq. 3.2

can be adjusted such that the maximal signal is always detected. By subtracting the signals acquired at each port of the coupler in Fig. 3.2(a) (i.e., performing balanced detection), the ideal SNR can be determined as:

$$M_{Optimal} = \frac{1}{4}(S_1 - S_2)^2, \quad (3.4)$$

with reconstructed signal of the form:

$$Sig_{M_{Optimal}} = P_R P_S \left(\frac{\epsilon \tau}{h\nu} \right)^2. \quad (3.5)$$

The expected value of the noise is given by:

$$E[M_{Optimal}(N_i)] = E\left[\frac{1}{4}(N_1 - N_2)^2\right] = \frac{1}{4}\left(E[N_1^2] + E[N_2^2]\right) = \frac{1}{2}\sigma^2. \quad (3.6)$$

This expression is expanded and written in terms of $E[N_i^2]$. For some of the following methods we will have terms of the form $E[N_i^4]$ as well. We can evaluate this simplified expression based on a knowledge of the variance at a single detection port: $E[N_i^2]=\sigma^2$ and $E[N_i^4]=3\sigma^4$ (where σ is given by Eq. 3.3). These substitutions can be made since the noise at each port is assumed to be Gaussian. The expectation of odd powers of N_i is zero since the noise is zero mean. In a similar manner we can now evaluate the variance of this method:

$$\begin{aligned} \sigma_{M_{Optimal}}^2 &= E\left[\frac{1}{16}(N_1 - N_2)^4\right] - \left(\frac{1}{2}\sigma^2\right)^2 \\ &= \frac{1}{16}E[N_1^4] + \frac{6}{16}E[N_1^2]E[N_2^2] + \frac{1}{16}E[N_2^4] - \frac{1}{4}\sigma^4. \\ &= \frac{3}{16}\sigma^4 + \frac{6}{16}\sigma^4 + \frac{3}{16}\sigma^4 - \frac{1}{4}\sigma^4 = \frac{1}{2}\sigma^4 \end{aligned} \quad (3.7)$$

Finally, we can determine the SNR as follows:

$$SNR_{Optimal} = \left(\frac{Sig_{M_{Optimal}}}{\sigma_{M_{Optimal}}} \right) \frac{P_R P_S \left(\frac{\epsilon \tau}{h\nu} \right)^2}{\frac{P_R \epsilon \tau}{\sqrt{2} 2 h\nu}} = 2\sqrt{2} \frac{P_S \epsilon \tau}{h\nu}. \quad (3.8)$$

Knowledge of phase can be attained in two ways. In the first situation, the phase is known prior to the measurement. This scenario can conceivably occur in well-controlled experiments where the only unknown variable is the signal amplitude. In the second situation, an estimate of the phase can be extracted from the measurement itself, and that information is then used in computing the signal amplitude. This type of phase estimation is employed in some of the following signal reconstruction algorithms. We note that the computation of signal amplitude where phase knowledge is used can be expected to be less robust and prone to systematic errors. In Section 3.5.3, we investigate the effect of phase error on our signal reconstruction algorithms, and find that they are surprisingly robust.

Heterodyne detection is typically accomplished using an AC lock-in amplifier. The measured signal is multiplied by a sine and cosine oscillating at the signal frequency, and summed over a variable time step, τ . The two outputs of the lock-in provide quadrature components for determination of signal amplitude and phase. The amplitude of the signal is then computed as the magnitude of the quadrature components. The signal reconstruction process can be written as the following, where S is the measured data:

$$M_{heterodyne} = \left(\sum_{i=1}^X (S_{i,1} - S_{i,2}) \cos(\Delta\omega_i) \right)^2 + \left(\sum_{i=1}^X (S_{i,1} - S_{i,2}) \sin(\Delta\omega_i) \right)^2. \quad (3.9)$$

The time step for each term in the summation is τ/X . In an analog mode lock-in amplifier X is effectively infinity and the summation can be replaced by an integration. As we shall see, the actual value of X (as long as it is >2) has no impact on the computed SNR. For the purpose of comparison, this method and each of the following methods leads to a reconstructed signal that is identical to Eq. 3.5. Derivation of the expected value and variance of the noise for this and following methods is detailed in Appendix D1. The results are given by:

$$E[M_{heterodyne}(N_i)] = 2X\sigma^2 \quad (3.10)$$

$$\sigma_{heterodyne}^2 = 4X^2\sigma^4, \quad (3.11)$$

which corresponds an SNR of the form:

$$SNR_{heterodyne} = \frac{P_R P_S \left(\frac{\varepsilon\tau}{h\nu}\right)^2}{2X \frac{P_R \varepsilon\tau}{2Xh\nu}} = \frac{P_S \varepsilon\tau}{h\nu}. \quad (3.12)$$

Heterodyne detection can also be improved given knowledge of the phase of the signal. In this case, the signal need only be multiplied by one phase matched sinusoidal component:

$$M_{heterodyne \text{ with phase knowledge}} = \left(\sum_{i=1}^X (S_{i,1} - S_{i,2}) \cos(\Delta\omega_i + \theta) \right)^2. \quad (3.13)$$

The use of phase knowledge results in a decrease in noise and corresponding increase in SNR.

$$E[M_{heterodyne \text{ with phase knowledge}}] = X\sigma^2 \quad (3.14)$$

$$\sigma_{heterodyne \text{ with phase knowledge}}^2 = 2X^2\sigma^4 \quad (3.15)$$

$$SNR_{heterodyne \text{ with phase knowledge}} = \frac{P_R P_S \left(\frac{\varepsilon\tau}{h\nu}\right)^2}{\sqrt{2}X \frac{P_R \varepsilon\tau}{2Xh\nu}} = \sqrt{2} \frac{P_S \varepsilon\tau}{h\nu}. \quad (3.16)$$

The above expressions will be useful as benchmarks to evaluate the performance of our image reconstruction algorithms with respect to optimal SNR, as well as routinely achievable SNR performance.

3.3.2 Method 1

Here we begin to discuss methods for image reconstruction given phase separated components at the three ports of a 3x3 fiber coupler based OCT system. We assume ideal conditions in which the power splitting ratios for the coupler are equivalent ($\alpha_{ij}=1/3$), $\varphi_j=120^\circ$, and $s_i=1$, and the signal and noise at each point is given by Eqs. 3.2 and 3.3 where $n=3$.

The most common method to reconstruct an image is to simply square and sum the signals from each port of the fiber coupler (51). This processing removes the cosine terms, which contribute a factor of 3/2 to the final reconstructed signal. We define method 1 as follows:

$$M_1 = \frac{3}{2} (S_1^2 + S_2^2 + S_3^2). \quad (3.17)$$

We can determine the mean value and variance of the noise to be:

$$E[M_1(N_i)] = \frac{9}{2} \sigma^2 \quad (3.18)$$

$$\sigma_{M_1}^2 = \frac{27}{2} \sigma^4, \quad (3.19)$$

and find an SNR of:

$$SNR_{M_1} = \frac{P_R P_S \left(\frac{\epsilon \tau}{h\nu} \right)^2}{\frac{3\sqrt{3}P_R \epsilon \tau}{\sqrt{23}h\nu}} = \frac{\sqrt{6} P_S \epsilon \tau}{3 h\nu}. \quad (3.20)$$

3.3.3 Method 2

A second method takes advantage of instantaneous quadrature, as described by Choma et al. (52). Taking the signal at port 1 of the coupler, S_I , as our real signal, the imaginary signal is reconstructed as:

$$S_{IM} = \frac{S_1 \cos \varphi_2 - S_2 \beta}{\sin \varphi_2} \quad \beta = \sqrt{\frac{\alpha_{41} \alpha_{51}}{\alpha_{42} \alpha_{52}}}. \quad (3.21)$$

Using the assumptions listed above, namely $\varphi_i=120^\circ$ and $\alpha_{ij}=1/3$. We are then able to reconstruct our image as the magnitude of this complex signal, $(S_{RE}^2+S_{IM}^2)$. We can simplify the expression as follows:

$$M_2 = \frac{9}{4}(S_{RE}^2 + S_{IM}^2) = 3(S_1^2 + S_2^2 + S_1 S_2). \quad (3.22)$$

We find noise parameters of the form:

$$E[M_2(N_i)] = 6\sigma^2 \quad (3.23)$$

$$\sigma_{M_2}^2 = 45\sigma^4, \quad (3.24)$$

and corresponding SNR:

$$SNR_{M_2} = \frac{P_R P_S \left(\frac{\varepsilon \tau}{h\nu} \right)^2}{\frac{3\sqrt{5}P_R \varepsilon \tau}{3h\nu}} = \frac{\sqrt{5} P_S \varepsilon \tau}{5 h\nu}. \quad (3.25)$$

3.3.4 Method 3

This method makes use of phase information during signal amplitude computations. We again follow Choma's method for obtaining instantaneous quadrature, and calculate the phase at each point in our image, $\theta=\tan^{-1}(S_{IM}/S_{RE})$. The estimated phase is then used to divide out the cosine terms present in Eq. 3.2. Finally, we scale and sum the three signals using scaling factors, a_i , constrained to sum to 1. In this way, we isolate the desired signal as follows:

$$M_3 = \frac{9}{4} \left[\frac{a_1 S_1}{\cos(\theta + \varphi_1)} + \frac{a_2 S_2}{\cos(\theta + \varphi_2)} + \frac{a_3 S_3}{\cos(\theta + \varphi_3)} \right]^2. \quad (3.26)$$

Scaling factors, a_i , are determined by substituting the measured phases, as well as φ_i , and minimizing the resulting noise. For example, if the values of θ and φ_i for a given channel produce a cosine value close to zero, then the noise would increase greatly after dividing it by this small number. Hence, this channel would be weighted the least compared to the others. And conversely, maximally interfering signals (large cosine value) are weighted more heavily than others. Since the noise in each channel is equivalent, larger interferometric signals should lead to an increase in SNR. The values of the scaling factors can be expressed as a function of the phase as well as the phase shifts between subsequent ports:

$$a_i = \frac{2}{3} [\cos^2(\theta + \varphi_i)]. \quad (3.27)$$

The noise parameters and SNR that correspond to this method are:

$$E[M_3[N_i]] = \frac{3}{2} \sigma^2 \quad (3.28)$$

$$\sigma_{M_3}^2 = \frac{9}{2} \sigma^4 \quad (3.29)$$

$$SNR_{M_3} = \frac{P_R P_S \left(\frac{\varepsilon \tau}{h\nu} \right)^2}{\frac{3P_R \varepsilon \tau}{\sqrt{23} h\nu}} = \sqrt{2} \frac{P_S \varepsilon \tau}{h\nu}. \quad (3.30)$$

This method can be generalized for an $n \times n$ fiber coupler based interferometer. In this case, the reconstruction based on Method 3 is given by:

$$\frac{n^2}{4} \left(\sum_{i=1}^n \frac{a_i S_i}{\cos\left(\theta + \frac{2\pi}{n}(i-1)\right)} \right)^2, \quad (3.31)$$

where a_i is:

$$\alpha_i = \frac{2}{n} \cos^2 \left(\theta + \frac{2\pi}{n} (i-1) \right). \quad (3.32)$$

As was previously mentioned, the sum over all a values is 1. The above expressions can be used to determine the expected value and variance of the noise for this generalized reconstruction method:

$$E[M_{3, n \text{ ports}}] = \frac{n}{2} \sigma^2 \quad (3.33)$$

$$\sigma_{M_{3, n \text{ ports}}}^2 = \frac{1}{2} n^2 \sigma^4, \quad (3.34)$$

with SNR determined as:

$$SNR_{M_{3, n \text{ ports}}} = \frac{P_R P_S \left(\frac{\epsilon \tau}{h\nu} \right)^2}{\frac{n P_R \epsilon \tau}{\sqrt{2} n h \nu}} = \sqrt{2} \frac{P_S \epsilon \tau}{h \nu}. \quad (3.35)$$

This expression is the same as that given in Eq. 3.30. Interestingly, the SNR associated with this method is independent of the number of output ports available for signal collection.

3.3.5 Methods 4 and 5

Finally we wish to discuss two additional reconstruction methods that are directly analogous to the processing performed by AC lock-in detection, and most easily understood in the context of a large number of detection ports (although these techniques will work as long as $n \geq 3$). Instead of expressing our interferogram in terms of pathlength mismatch, we can write it in terms of phase delay, where each detection port samples a different phase delay. Thus by multiplying the measured signal by sines and cosines

phase shifted similarly to each of the output ports, we can estimate the amplitude of the signal by averaging the result. The signal is reconstructed as:

$$M_4 = \left(\sum_{i=1}^n S_i \cos(\varphi_i) \right)^2 + \left(\sum_{i=1}^n S_i \sin(\varphi_i) \right)^2, \quad (3.36)$$

and the noise is given by:

$$E[M_4(N_i)] = n\sigma^2 \quad (3.37)$$

$$\sigma_{M_4}^2 = n^2\sigma^4. \quad (3.38)$$

We find SNR equivalent to the heterodyne case:

$$SNR_{M_4} = \left(\frac{P_R P_S \left(\frac{\varepsilon\tau}{h\nu} \right)^2}{n \frac{P_R \varepsilon\tau}{nh\nu}} \right) = \frac{P_S \varepsilon\tau}{h\nu}. \quad (3.39)$$

Likewise, with knowledge of the phase of the signal from quadrature components in Section 3.3, the signal can be reconstructed using only one sinusoidal component:

$$M_5 = \left(\sum_{i=1}^n S_i \cos(\theta + \varphi_i) \right)^2 \quad (3.40)$$

$$E[M_5(N_i)] = \frac{n}{2}\sigma^2 \quad (3.41)$$

$$\sigma_{M_5}^2 = \frac{1}{2}n^2\sigma^4. \quad (3.42)$$

The noise is reduced by a factor of 2, giving an SNR of:

$$SNR_{M_5} = \left(\frac{P_R P_S \left(\frac{\varepsilon\tau}{h\nu} \right)^2}{\frac{n}{\sqrt{2}} \frac{P_R \varepsilon\tau}{nh\nu}} \right) = \sqrt{2} \frac{P_S \varepsilon\tau}{h\nu}. \quad (3.43)$$

The results of these derivations can be found in Table 3.1. We note that the two methods that incorporate phase information, Methods 3 and 5, are predicted to have better SNR in comparison with the other methods. It is interesting to note that Methods 3 and 5 are predicted to have the same SNR. In fact, as is derived in Appendix D1, a substitution of Eq. 3.32 for a_i converts Method 3 into a form identical to Method 5. However similar, we note that these methods differ in the case where the phase shifts at the ports of the fiber coupler are not equally spaced (i.e., $\varphi_i \neq 2\pi(i-1)/n$). In this case, the a_i s can be determined through a minimization, and the method will produce an image with a different SNR than that derived above. Method 5 requires that the phase shifts be equally spaced, and will not perform well under these conditions.

Finally, we note that although we have assumed shot noise limited detection in these derivations, the five methods will perform the same with respect to one another so long as the dominant noise source is white.

Reconstruction Method	Method 1	Method 2	Method 3	Method 4	Method 5
Theoretical SNR	$\frac{\sqrt{6P_s \epsilon \tau}}{3hv}$	$\frac{\sqrt{5P_s \epsilon \tau}}{5hv}$	$\frac{\sqrt{2P_s \epsilon \tau}}{hv}$	$\frac{P_s \epsilon \tau}{hv}$	$\frac{\sqrt{2P_s \epsilon \tau}}{hv}$
Experimental SNR (dB)	88.0	85.6	91.0	90.6	91.1
Theoretical Comparison to Method 5 (dB)	-2.4	-5	0	-1.5	0
Experimental Comparison to Method 5 (dB)	-3.1	-5.4	-0.04	-0.4	0
Theoretical Mean Noise	$\frac{1}{2}\sigma^2$	$6\sigma^2$	$\frac{3}{2}\sigma^2$	$3\sigma^2$	$\frac{3}{2}\sigma^2$
Experimental Mean Noise (10^{-6})	4.6	5.9	2.4	2.9	2.4

Table 3.1. Comparison of theoretical and experimental results. Notably, the phase dependent methods (3 and 5) show superior SNR and noise performance with respect to the others.

3.4 Experimental Methods

The system depicted in Fig. 3.1 was calibrated to determine accurate values for ϕ_i and s_i . In order to make SNR measurements, a mirror was placed in the sample arm to serve as an ideal reflector, which was attenuated (-70 dB) such that sample arm shot noise was negligible compared to that from the reference arm. A beam chopper was used to alternate measurements of signal and background noise. In order to assure that we were using our homodyne system to acquire shot noise limited data, as opposed to dominant $1/f$ noise, we sampled quickly, at 800 kHz, and limited our data averaging time (~ 0.65 ms) following the results of Ref. (65). Both signal and noise data were reconstructed using the five methods described above, and the SNR was determined as the mean signal divided by the standard deviation of the noise. The methods were also compared based on the mean value of the reconstructed noise.

We then used the 3x3 homodyne OCT system to acquire several images. Our system resolution has been measured to be approximately 14 μm in the axial direction, and 9.4 μm in the lateral direction. First, we imaged a highly attenuated Air Force test target (-50 dB) in order to visualize the relative performance of the three methods in a low signal situation. We then imaged stage 54 *Xenopus laevis* tadpoles. Each data set was processed using the five image reconstruction algorithms described above, and displayed on equivalent color scales. The improved image contrast obtained using reconstruction Methods 3 and 5 confirms our theoretical findings in biological samples.

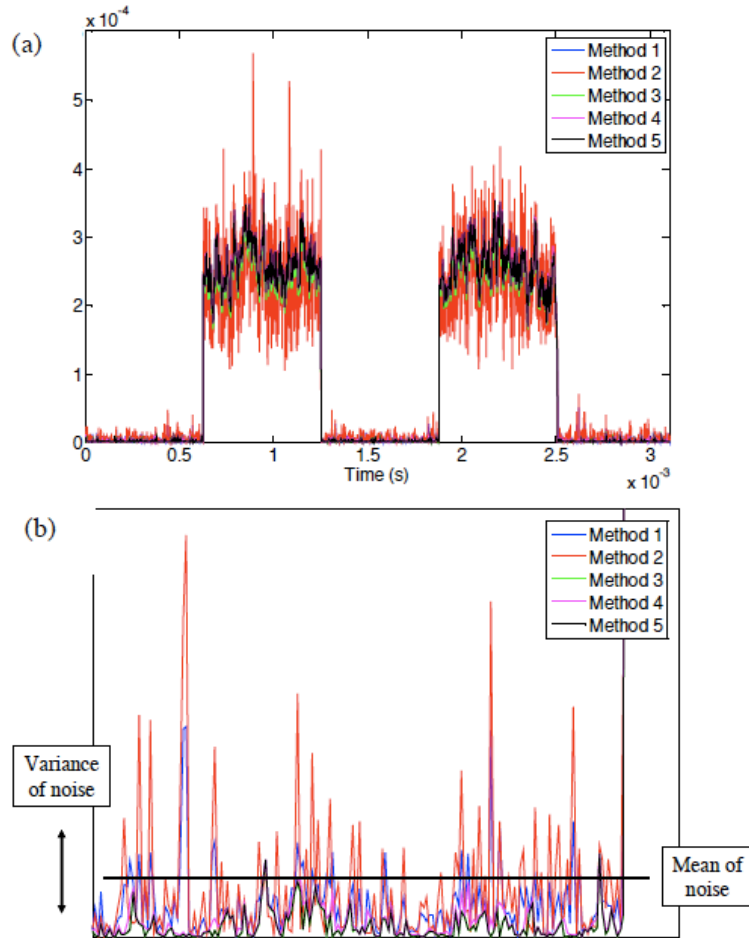


Figure 3.3. a) Reconstructed signals from an attenuated mirror. A beam chopper was used to make measurements of both signal and background noise, which were used to experimentally determine the SNR of the five methods. b) A magnified view of the noise from (a) depicting experimentally determined values for the mean and variance of the noise.

3.5 Results and Discussion

3.5.1 Experimental SNR Results

We evaluated our reconstruction methods based on data acquired with an attenuated mirror in the sample arm. Figure 3.3 displays a typical reconstructed trace, showing alternating signal and noise measurements as the sample beam was chopped. The SNR of the reconstructed signals were determined, as well as the mean value of the noise. Both calculations were made using the data depicted in Fig. 3.3. The results can be seen in Table

1, showing that Methods 3 and 5, which take advantage of the known phase in order to minimize the noise, perform significantly better than the other methods in terms of SNR. In close agreement with our theoretical predictions, we found an SNR enhancement of up to 5.4 dB over the phase independent methods. These two methods also leave the smallest remaining DC noise after signal reconstruction. However, we note that these two methods do not match theoretical predictions for mean noise as closely as the other three methods. It is reassuring that Methods 3 and 5 vary from theory in a comparable manner, since they perform very similar processing; however, the exact cause of this discrepancy is unclear to the authors at this time.

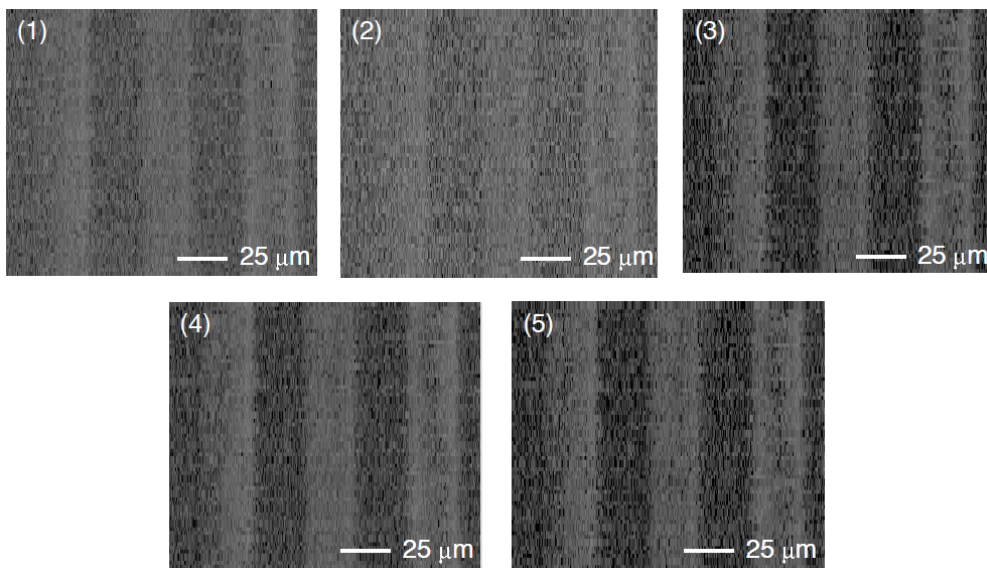


Figure 3.4. These images show a portion of a highly attenuated Air Force test target, representing a very low signal situation. The three images were reconstructed from a single data set and reconstructed using Methods 1–5 (described above). Methods 3 and 5 clearly perform better than the others, showing a notable increase in contrast between the bars of the test target and the background.

3.5.2 Imaging Results

The SNR improvement noted in the previous section is quite dramatic in our reconstructed images. Figure 3.4 shows a portion of an Air Force test target. The resolution target was highly attenuated (-50 dB) such that the optical power returning

through the sample arm was very low. Each of the images shown in Fig. 3.4 was reconstructed from the same raw data using Methods 1–5 described above. Additionally, each image is displayed on the same color scale. We see that for the image reconstructed using Method 2 the bars on the test target can barely be discriminated from the background. The image reconstructed using Method 1 is better, but there is still relatively little contrast between the bars and the background noise. As predicted by the theoretical sensitivity analysis, Methods 3 and 5 produce images with a marked increase in contrast compared to the others. The bars of the Air Force test target are clearly distinguishable in panels (3) and (5) of Fig 3.4.

Our reconstruction algorithms were also tested on data from biological images. Fig. 3.5 (first column) shows an image of structures in the anterior, medial portion of a stage 54 *Xenopus laevis* tadpole. Again, Methods 3 and 5 produced images that more clearly distinguish biological structure from background noise. The nuclei of the cellular structures at the bottom of the image are more visible. The ability to achieve superior SNR based only on reconstruction algorithm implies that, to achieve the same SNR as through commonly used reconstruction algorithms, the optical power incident on fragile biological tissues can be reduced. In Fig. 3.5 (second column) we have subtracted the DC value of the noise in each image in order to compare the noise variance between images. When a portion of the background noise is magnified (Fig. 3.5, column 3), there is significantly more background fluctuation in images corresponding to Methods 1 and 2 than in the other images.

We have seen in the above experimental results that Methods 3 and 5 are capable of producing images with the highest SNR. In these methods, knowledge of the phase at

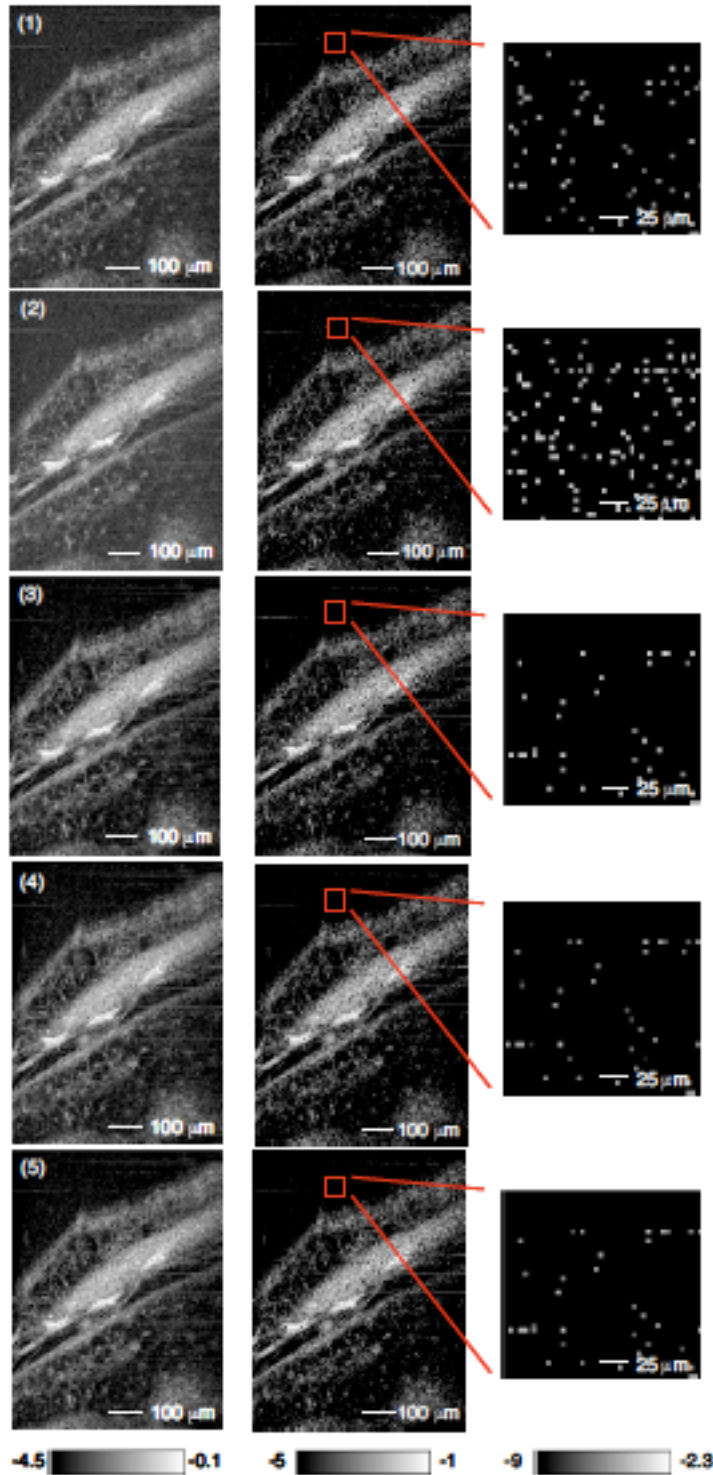


Figure 3.5. In the first column the image reconstruction algorithms were evaluated on images from a stage 54 *Xenopus* tadpole. Again, Methods 3 and 5 produced images with improved SNR, more clearly distinguishing biological features such as cell nuclei from background noise. In the second column of images the DC noise has been subtracted from the image. The increase noise variance is now visible in the background of the images corresponding to Methods 1 and 2 in a blown up portion of the background (third column)

each point in the image was used to minimize the noise at that point. In essence, these algorithms utilize more of the available information than the other methods.

3.5.3 Robustness to Phase Error

The performance of each of the signal reconstruction methods depends on appropriate calibration of the 3x3 homodyne OCT system. However, Methods 3 and 5 are strongly dependent on correct calculation of the phase. Determination of the phase depends on exact knowledge of the loss scaling coefficients, s_i , and the angles between adjacent ports of the fiber coupler, ϕ_{ij} . Uncertainty in these values leads to uncertainty in the phase at various points in the image, and additionally leads to an improper choice of noise minimization coefficients, a_i , in Method 3. To reduce the effects of this potential problem, we calibrated the 3x3 system immediately before image acquisition, making the assumption that drifts in the system calibration parameters are slow.

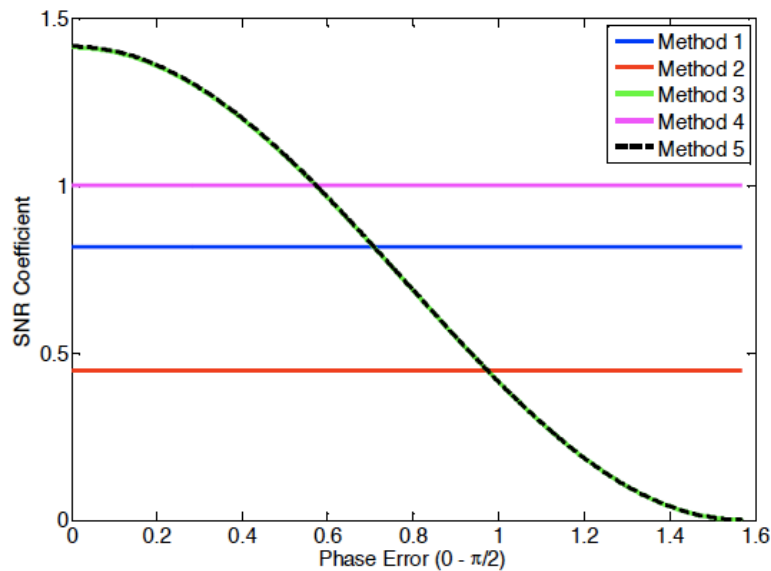


Figure 3.6. SNR is plotted versus phase error for the five reconstruction methods. Only Methods 3 and 5 are phase dependent. Here, we see that these methods are relatively robust to phase error, only dropping below the other methods for fairly large errors in phase.

Additionally, we investigated the impact of phase error on the SNR of the reconstruction methods. To do this, we computed the SNR corresponding to each method using a phase $\Theta+d\theta$, where $d\theta$ is a phase error that varies from 0 through $\pi/2$. The results are plotted in Fig. 3.6 in terms of the SNR coefficient (i.e., the coefficient of $P_{S\epsilon\tau}/h\nu$). The computation shows that Method 3 and 5 are surprisingly robust in the presence of phase error. Very large phase errors may be incorporated before these methods drop below the others in terms of SNR. These results imply that the phase-dependent methods not only provide improved SNR, but are relatively insensitive to errors in system calibration.

3.6 Conclusions

In conclusion, we have demonstrated the effect of image reconstruction algorithm on the SNR when phase separated components are detected. We compared five potential methods for reconstructing an image from the three outputs of a 3x3 fiber coupler-based homodyne OCT system, and demonstrated that algorithms which use knowledge of the phase at each point in the image to minimize noise perform significantly better than the others in terms of SNR. This holds true for both homodyne and heterodyne techniques. The algorithms showed an SNR increase of up to 5 dB over the other methods, and were found to perform better than the most commonly used forms of heterodyne detection. This increase in SNR was evident as improved contrast, as well as overall image quality, in images from both an Air Force test target as well as biological samples. Additionally, we found that these phase-dependent methods are relatively robust in terms of phase error. Finally, we note that our analysis is not restricted to 3x3 homodyne OCT, but can be

applied to any situation in which phase separated components are combined to decouple phase and amplitude information.

Chapter 4. Modeling the Effects of 1/f Noise

This chapter is adapted from Ref (65): E.J. McDowell, X. Cui, Z. Yaqoob, and C. Yang, 'A generalized noise variance model and its applications to the characterization of 1/f noise,' Optics Express, 15(7), 3833–3848 (2007).

4.1 Introduction

1/f noise, alternately referred to as pink or flicker noise, is found in a wide range of physical systems (66–69), from carbon resistors and semiconductors (70), to heartbeat dynamics (71) and traffic flow (72). In general, 1/f noise has a power spectral density that follows the form $1/f^\alpha$, where α commonly ranges from 0.5 to 1.5 (73). Despite significant effort in describing a universal model for the origin of 1/f noise (74), no single model is currently accepted, and the origins of 1/f noise have only been well characterized in very specific circumstances. For example, 1/f noise in vacuum tubes is commonly modeled as a superposition of relaxation rates that characterize the release of electrons from cathode surface trapping sites (73, 75, 76). Additionally, the 1/f noise measured in cellular ion currents has been attributed to the stochastic nature of the opening and closing mechanisms of voltage gated ion channels (77).

The presence of 1/f noise in optical detection can significantly degrade the effective precision and sensitivity of the optical technique. In interferometric methods, including time domain optical coherence tomography (OCT) (19), a typical strategy for avoiding 1/f noise involves the use of heterodyne detection in which the signal of interest

is modulated and shifted into a frequency band in which $1/f$ noise is small compared to other sources of noise. Under these circumstances, we typically consider only white noise processes, which include receiver noise, shot noise, and excess intensity noise (25).

Homodyne methods are advantageous in their simplicity. By directly detecting the interferometric signal, there is no need for scanning mechanisms or lock-in detection. In addition, a properly performed homodyne experiment can provide a 3 dB improvement in SNR compared to heterodyne techniques (57–59). Homodyne interferometric methods have long been used to measure displacements (78, 79) and vibrations (80, 81), and have been adapted to a variety of other applications including the detection of trace gasses (82). In addition, there has been a recent rise in homodyne interferometric methods for biomedical applications (51, 52, 83, 84). We also note that most of the spectrometer-based OCT systems reported thus far, which have an improved SNR over time domain techniques (22–24), are homodyne in nature. An understanding of the impact of $1/f$ noise can guide better detection scheme design, and direct the selection of operating parameters.

The issue of $1/f$ noise in homodyne detection, and optical detection in general, is an understudied problem. In an optical system, we expect $1/f$ noise to be generated by the broadband source (85), as well as the photodetector circuitry (86). The complex nature of the light detection process makes it difficult to directly identify the specific noise generating sources in the light detection chain. More importantly, even if the $1/f$ noise characteristics of a given system can be empirically determined, there is a need for a suitable theoretical model that can be used to characterize the impact of $1/f$ noise on the sensitivity of a detection system.

In Section 4.2, we present a novel time domain approach to determine the SNR behavior of an optical system in the presence of $1/f$ noise. To our knowledge, this approach has not been previously reported. Using this model, we examine the impact of the noise exponent, α , (Section 4.2.1) as well as the total experimental time frame, T (Section 4.2.2). Two findings are particularly noteworthy. 1) The noise model shows that for $\alpha > 1$, the $1/f$ noise variance is proportional to the square of the integration time (τ). This implies that for measurements that are dominated by $1/f$ noise, the SNR cannot be improved by increasing the integration time of the measurement. 2) The noise model also predicts the existence of a characteristic time ($\tau_{\text{white-to-1/f}}$) at which $1/f$ noise begins to dominate over white noise, such as shot noise. In Section 4.3, we describe our 3×3 fiber coupler based homodyne interferometer, as well as the experiments that were conducted to characterize $1/f$ noise in that system. In Section 4.4, we compare our theoretical results to experimental findings from the homodyne interferometer. In addition to validating our theoretical results, we also find that the $1/f$ noise characteristics are detector dependent. Finally, we summarize our findings in Section 4.5.

4.2 Theoretical Noise Model

In the following analysis we will consider a generalized noise source with known power spectral density. It is a well-known fact that SNR in the limit of dominant white noise, such as shot noise, increases linearly with integration time (τ). (In keeping with interferometry convention, we define SNR as the ratio of the square of the signal count to the noise variance.) However, we do not expect this trend in the case of dominant $1/f$ noise. The presence of $1/f$ noise implies that the amplitude of noise fluctuations will increase on longer time scales. The following model allows us to examine the

dependence of both 1/f noise and white noise on integration time, and determine the appropriate detection parameters to obtain the optimal SNR for a given optical system.

In order to determine the contribution of 1/f noise to the SNR of an optical system, we would like to determine the variance of the 1/f noise amplitude distribution as a function of the integration time of the detection system. The following derivation presents a method for determining this variance using the power spectral density of the noise to construct a time series that can then be ensemble averaged appropriately. This is, to the best of our knowledge, a new approach that is useful for analyzing any generalized noise sources for which the power spectral density is known. For the sake of clarity, we choose to quantify our signal in terms of photon count rate and photon counts. We note that through appropriate scaling these expressions can be converted to quantities of energy and power.

We can describe the signal time trace as a combination of a DC term, representing the mean signal, and a time varying, zero mean term that represents the noise. The noise term can be expressed as a summation of frequency dependent contributions, each weighted by the power spectral density of the noise distribution:

$$\begin{aligned} x(t) &= x_0 + \Delta x(t) \\ &= x_0 + \sum_{i=1}^{\infty} \sqrt{2S(f_i)\Delta f} \cos(2\pi f_i t + \delta_i) \end{aligned} \quad (4.1)$$

Here, x_0 is the mean signal (photon count rate), $S(f_i)$ is the power spectral density corresponding to the frequency f_i , and δ_i is a random phase shift that varies uniformly on the interval $[0, 2\pi]$. The phase shifts between f_i and f_{i+1} are uncorrelated, producing the desired noise source. The exact definition of the power spectral density, $S(f)$, can vary from community to community. The power spectral density employed here is given by

the Fourier transform of autocorrelation function of the measured signal. This results in a symmetrically distributed power spectrum. $S(f)$ in Eq. 4.1 is a single-sided power spectrum, which contains double the original value for each positive frequency. The power contained in each frequency step, Δf , is given by $S(f)\Delta f$. Thus, to obtain the total signal in each frequency step we must include the discretization within the square root in Eq. 4.1. We briefly verify our representation of the signal in Eq. 4.1 by noting that for a signal of the form $A\cos(2\pi f_0 t)$, the single sided power spectrum is given by $S(f) = (A^2/2)\delta(f-f_0)$. As such, the factor $\sqrt{2S(f)\Delta f}$ yields the correct weight of A in the frequency step containing f_0 .

An actual measurement of the signal count, which necessitates the collection of signal photons over a finite measurement time window, τ , will yield two terms. The first term simply integrates over τ to give an expected value of $X(\tau) = x_0\tau$. For the second term we have the following:

$$\Delta X(\tau) = \int_0^{\tau} \Delta x(t) dt \quad (4.2a)$$

$$E(\Delta X(\tau)) = 0, \quad (4.2b)$$

where the expected value of the noise fluctuations is zero. Thus, the variance of the noise is given by the second moment of $\Delta X(\tau)$:

$$\sigma_X^2(\tau) = E(\Delta X(\tau)^2) = E\left[\left(\int_0^{\tau} \left(\sum_{i=1}^{\infty} \sqrt{2S(f_i)\Delta f} \cos(2\pi f_i t + \delta_i)\right) dt\right)^2\right]. \quad (4.3)$$

We can then rewrite the product,

$$\sigma_X^2(\tau) = E\left[\int_0^{\tau} \sum_{i=1}^{\infty} \sqrt{2S(f_i)\Delta f} \cos(2\pi f_i t + \delta_i) dt \left[\int_0^{\tau} \sum_{j=1}^{\infty} \sqrt{2S(f_j)\Delta f} \cos(2\pi f_j t + \delta_j) dt \right]\right], \quad (4.4)$$

noting that since δ_i and δ_j are uncorrelated for $i \neq j$, the expectation will vanish unless $i=j$.

$$\begin{aligned}\sigma_x^2(\tau) &= E \left(\sum_{i=1}^{\infty} \left[\int_0^{\tau} \sqrt{2S(f_i)\Delta f} \cos(2\pi f_i t + \delta_i) dt \right]^2 \right) \\ &= E \left(\sum_{i=1}^{\infty} \left[\frac{\sqrt{2S(f_i)\Delta f}}{2\pi f_i} (\sin(2\pi f_i \tau + \delta_i) - \sin(\delta_i)) \right]^2 \right) \\ &= E \left(\sum_{i=1}^{\infty} \frac{2S(f_i)\Delta f}{(2\pi f_i)^2} [\sin^2(2\pi f_i \tau + \delta_i) - 2\sin(2\pi f_i \tau + \delta_i)\sin(\delta_i) + \sin^2(\delta_i)] \right).\end{aligned}\tag{4.5}$$

The expectation can then be evaluated by taking an ensemble average where δ_i is varied in the interval $[0, 2\pi]$.

$$\sigma_x^2 = \frac{1}{2\pi} \int_0^{2\pi} \left(\sum_{i=1}^{\infty} \frac{S(f_i)\Delta f}{2(\pi f_i)^2} [\sin^2(2\pi f_i \tau + \delta_i) - 2\sin(2\pi f_i \tau + \delta_i)\sin(\delta_i) + \sin^2(\delta_i)] \right) d\delta_i\tag{4.6}$$

Finally, we decrease the spacing between subsequent elements in the infinite sum, and rewrite the variance in integral form:

$$\sigma_x^2(\tau) = \int_0^{\infty} \frac{S(f)}{2(\pi f)^2} [1 - \cos(2\pi f \tau)] df.\tag{4.7}$$

This expression is useful and generalized. It can be used with any noise power spectral density to derive the noise variance.

To verify our result, we begin by considering the situation where white noise dominates (i.e., $S(f)=A_{white}$). In this situation, Eq. 4.7 can be rewritten as:

$$\sigma_{X, white}^2(\tau) = \int_0^{\infty} \frac{A_{white}}{2(\pi f)^2} [1 - \cos(2\pi f \tau)] df\tag{4.8}$$

$$\sigma_{X, white}^2(\tau) = \frac{A_{white}\tau}{2}.\tag{4.9}$$

Here, we can immediately recognize this form as the variance of white noise. For an

idealized photon flow that is shot noise limited, the coefficient A_{white} is given by $2x_0$. This leads to $\sigma_{X, shot\ noise}^2(\tau) = x_0\tau$; a result that is consistent with the Poissonian nature of shot noise.

If we instead substitute the power spectral density that we expect for 1/f noise, $S(f) = A_{pink}/f^\alpha$, we obtain Eq. 4.10. However, this integral diverges at $f=0$. By integrating from a minimum frequency, f_{min} , we can effectively cap the function and force the integral to converge. As we will show in Section 4.2.1, this truncation is valid under certain experimental conditions, and f_{min} is directly related to the total time frame of the experiment (T). The variance is then given by:

$$\sigma_{X, pink}^2(\tau, f_{min}) = \int_{f_{min}}^{\infty} \frac{A_{pink}}{2\pi^2 f^{\alpha+2}} [1 - \cos(2\pi f\tau)] df. \quad (4.10)$$

In the following sections we analyze Eq. 4.10 in terms of its dependence on both f_{min} and α . Additionally, since there is no straightforward analytical solution to Eq. 4.10, we approximate the solution in order to show the form of the dependence on integration time (τ).

4.2.1 Choice of f_{min}

In our analysis, we choose $f_{min}=1/T$, where T is the total experimental time frame. This is different from the integration time τ , which gives the time step over which the signal is sampled. The difference between these two time constants can be better appreciated in the following scenario. Suppose we have a light source with a known 1/f noise power spectrum, $S(f)$, which we decide to amplitude modulate in order to send a message. The message length is T in its entirety. The message is analog in nature but is band limited such that it does not contain frequency components beyond f_{signal} . The message can be

received, with no information loss, by measuring the light intensity over a time frame of T and choosing a time step of $\tau=2/f_{signal}$ for signal integration. Intuitively, we can appreciate that this time step integration is useful for suppressing high frequency ($f > f_{signal}$) noise contributions in our measurements. The noise variance for this experiment can be calculated using Eq. 4.10 based on the abovementioned parameters. We can see that the message length T is relevant for noise variance consideration; as the length of T is increased, more low frequency noise components will be incorporated, and the SNR will correspondingly deteriorate. Noise components of frequency lower than f_{min} are present in the collected signal trace. However, these components manifest as a net DC shift in the entire collected signal, and have no impact on the content of the sent message (see Fig. 4.1).

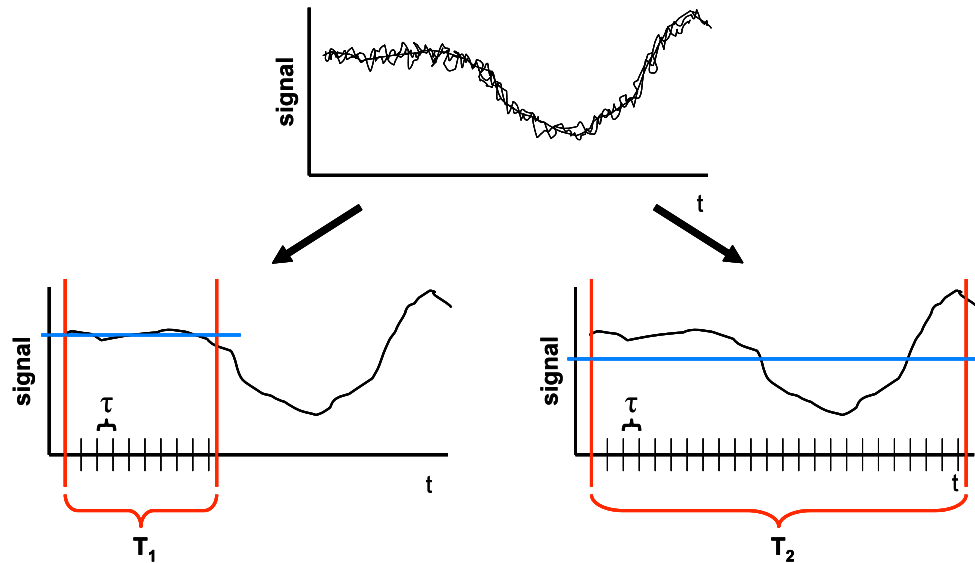


Figure 4.1. The total time frame of an experiment, T , determines the lowest frequency noise components that are incorporated into a measured signal. The upper panel depicts the raw signal, or amplitude modulated ‘message’ that is encoded on a $1/f$ noise dominated light source (see Section 2.1). If the message is band limited such that it does not contain frequency components beyond f_{signal} , the message can be optimally collected by integrating the collected signal in time steps of $\tau=2/f_{signal}$. In the left panel, low frequency noise ($f < f_{min}$) in the light source causes a net DC shift in the acquired signal. As T is increased (right panel) the same low frequency noise dramatically impacts the measured noise variance between subsequent time steps (τ), which can lead to a degradation in the SNR of the collected message.

There is an additional scenario in which a minimum frequency may be imposed on Eq. 4.10. In certain situations the power law behavior of $1/f$ noise breaks down for very low frequencies (73). This imposes a natural cap on Eq. 4.10, which is approximately constant across these low frequencies, implying that fluctuations do not become infinitely large. In this case, however, we cannot approximate Eq. 4.10 by simply integrating from the corner frequency through infinity. We must also consider the area under the constant portion of the power spectrum in determining the total noise variance (so long as these frequencies fall above the f_{min} imposed by the detection system). In reality, this type of natural capping has only been seen in very few experimental situations (87, 88). Most often, $1/f$ behavior can be seen down to the lower frequency bound of the measurement. In fact, $1/f$ noise has been measured over 6 frequency decades (89), and has been shown to display the familiar trend at frequencies as low as $1/(3$ weeks) in MOSFETs (90) and even $1/(300$ years) for weather data (91).

4.2.2 Influence of the Noise Exponent, α

The value of α can dramatically influence the $1/f$ noise variance characteristics. To motivate our discussion, we will first present numerical solutions to Eq. 4.10, allowing for an empirical determination of the dependence on integration time. For verification, we will more rigorously demonstrate the τ dependence by deriving an approximation to Eq. 4.10, which clearly reveals the role of τ .

Equation 4.10 is numerically approximated (MATLAB), and the standard deviation of the noise fluctuations (square root of Eq. 4.10) is plotted in Fig. 4.2 for various values of α . These curves are solely intended for the purpose of examining the dependence of the noise on integration time. The individual curves plotted in Fig. 4.2 have arbitrary amplitudes relative to one another, as the units of A_{pink} will change as α is

varied. An f_{min} of 1.6 mHz, corresponding to a relatively long experimental time frame, was used in these simulations.

As we expect, the white noise curve, $\alpha=0$ in Figs. 4.2 (a) and (b) show a dependence on the square root of the integration time. As α varies from 0 to 1 (Fig. 4.2(a)), the standard deviation appears to transition from a square root-type dependence towards a linear dependence. This response demonstrates the gradual transition from white noise to 1/f noise as α is increased. Interestingly, for $\alpha>1$ (Fig. 4.2(b)), the standard deviation appears to increase linearly with integration time. This suggests the fact that, under conditions where 1/f noise is dominant, the total noise increases in proportion with the signal. Additionally, we note that the white noise curve tapers faster than all curves for which $\alpha\neq 0$. Thus, each of the 1/f noise curves necessarily crosses the shot noise curve at some point. This fact implies the existence of a characteristic time ($\tau_{white-to-1/f}$) at which 1/f noise begins to dominate over white noise.

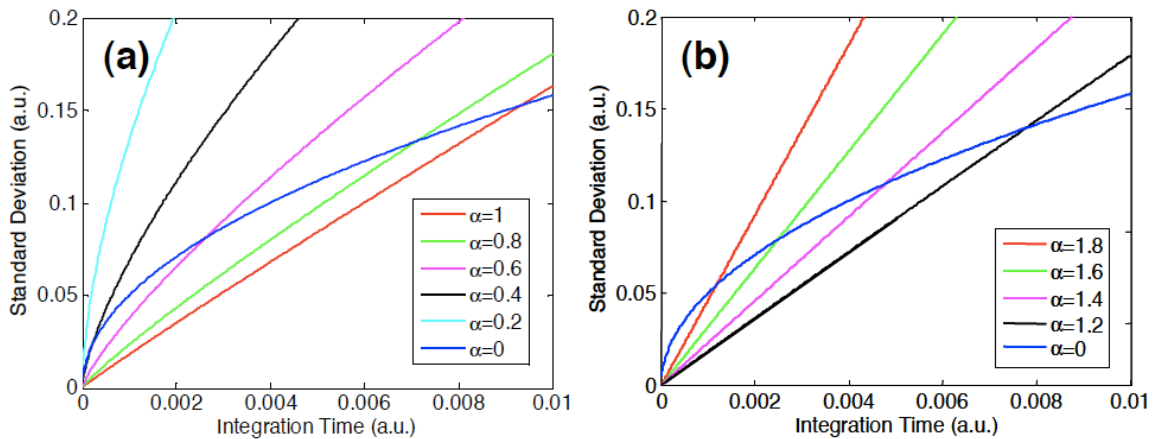


Figure 4.2. Theoretical results for noise standard deviation versus integration time, square root of Eqs. 4.9 and 4.10 for white noise and 1/f noise, respectively. The 1/f noise transitions from the square-root dependence of white noise ($\alpha=0$) to a linear dependence as α increases from 0 to 1, and maintains a linear dependence on integration time for $\alpha>1$.

SNR traces corresponding to the same α values as Fig. 2 are plotted in Fig. 4.3. Here, we define SNR as $(X/\sigma)^2$ [37], where X is the total number of photon counts, which increases linearly with τ , and σ is the standard deviation of the noise. As expected, the theoretical shot noise limited SNR increases linearly with integration time. For $0<\alpha<1$,

the SNR transitions from a curve that is approximately linear (similar to white noise), to a curve that appears to taper towards a constant value. The linear dependence of the $1/f$ noise standard deviation in Fig. 4.2(b) implies that the corresponding SNR will be constant, since the total signal also increases linearly with increasing integration time. Figure 4.3(b) shows that this appears to be empirically true.

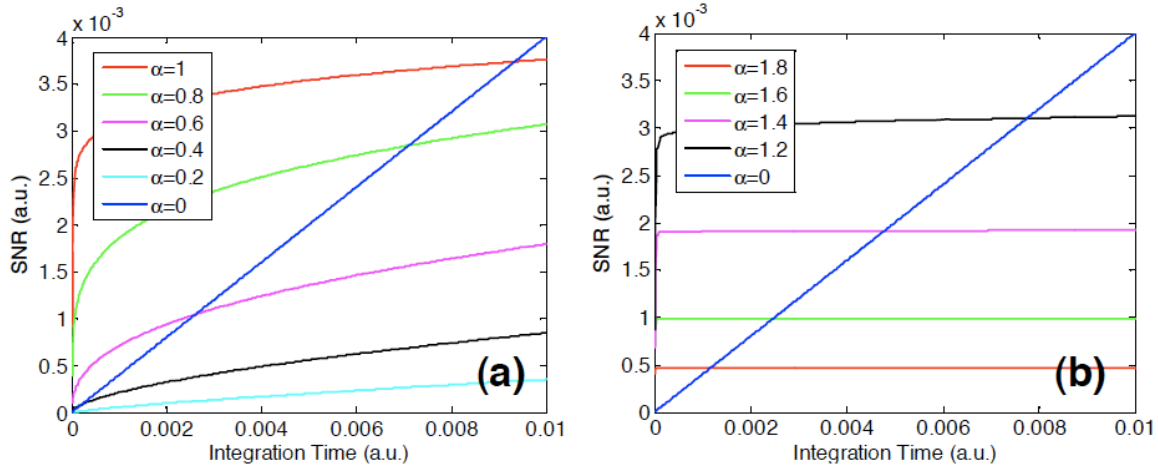


Figure 4.3. Theoretical results for SNR versus integration time. As expected, the white noise limited SNR increases linearly with integration time. In the case of dominant $1/f$ noise, the SNR increases with decreasing slope for $0 < \alpha < 1$, and tapers to a constant value for $\alpha > 1$.

The above simulations provide some initial intuition into the dependence of integration time on SNR in the limit dominant $1/f$ noise. It is possible to derive an approximate solution to Eq. 4.10 that shows the explicit dependency of the noise variance on integration time, τ , for a wide class of experimental situations. Specifically, if $\tau \ll 1/f_{min}$, Eq. 4.10 can be easily simplified. In the context of the thought experiment described above (Section 4.2.1), this constraint corresponds to a situation in which the message is long (f_{min} small) and the maximum signal frequency is high ($\tau = 2/f_{signal}$ is small) — a signal that can be expected to describe an overwhelmingly large fraction of practical situations. Under these conditions, we arrive at the following expressions for the noise variance:

$$\begin{aligned}
\sigma_{X,pink}^2(\tau, f_{\min}) &\approx \frac{A_{pink}}{2} \left[\frac{(2\pi)^\alpha \tau^{\alpha+1}}{(\alpha+1)\alpha\Gamma(\alpha)\cos\left(\frac{\alpha\pi}{2}\right)} \right] & 0 < \alpha < 1 \\
&\approx A_{pink} \left[\frac{\tau^2}{(\alpha-1)f_{\min}^{\alpha-1}} \right] & \alpha > 1 \\
&& \text{except when } \alpha \in \mathbb{Z}^+
\end{aligned} \tag{4.11}$$

where $\Gamma(\alpha)$ is the mathematical gamma function defined as $\int t^{\alpha-1} e^{-t} dt$ over the interval $[0, \infty]$ for $\alpha > 0$. \mathbb{Z}^+ refers to the set of positive integers. Equation 4.11 shows that, for small f_{\min} and increasing τ , two distinct regimes exist. In these regimes, the SNR depends on τ as follows:

$$\begin{aligned}
SNR(\tau) &\sim O(\tau^{1-\alpha}) & 0 < \alpha < 1 \\
&\sim O(\tau^0) & \alpha > 1 \\
&& \text{except when } \alpha \in \mathbb{Z}^+
\end{aligned} \tag{4.12}$$

For $0 < \alpha < 1$ Eq. 4.11 shows a dependence of the variance on $\tau^{\alpha+1}$. This confirms our intuition of a transition from white noise to $1/f$ noise, as the SNR moves from a function with τ dependence to a function of constant value. This dependence implies that the SNR can still increase after crossing the characteristic integration time ($\tau_{\text{white-to-1/f}}$) at which $1/f$ noise begins to dominate, although the gain in SNR from further increases in τ occurs with diminishing returns as α approaches 1.

For $\alpha > 1$ we find a τ^2 dependence. These approximations confirm our observations from Figs. 4.2 and 4.3 that, for $\alpha > 1$, the SNR should reach a constant value when $1/f$ noise is the dominant noise process. This is quite a remarkable fact, implying that once the integration time is increased past $\tau_{\text{white-to-1/f}}$, there will be no further significant improvements in SNR. The τ dependence of Eq. 4.10 and Eq. 4.11 is plotted in Fig. 4.4 versus the $1/f$ exponent, α . For integer values of α , Eq. 4.10 cannot be easily solved, and these locations are represented by open circles.

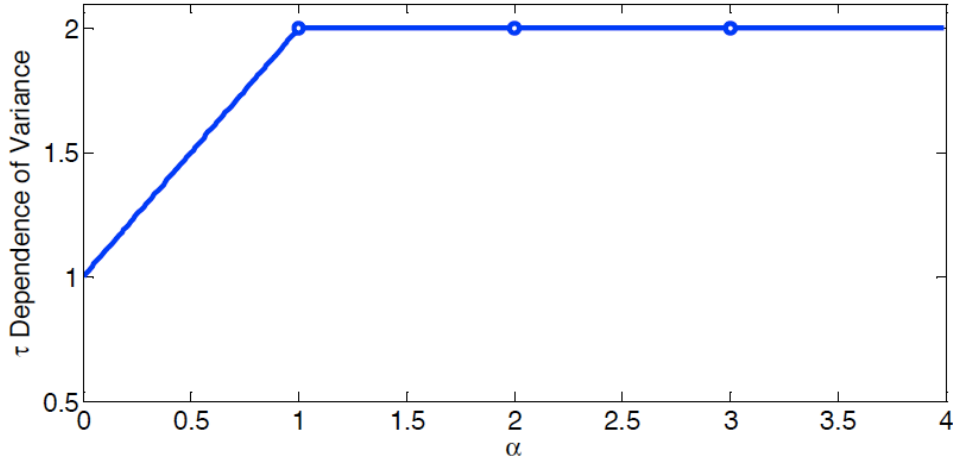


Figure 4.4. The τ dependence of the $1/f$ noise variance is dependent on the $1/f$ exponent, α . For $\alpha > 2$, this dependence is given by τ^2 . Open circles represent α values that cannot be simply approximated by Eq. 4.11.

4.3 Experimental Methods

The model described in Section 4.2 is widely applicable. In particular, it is very appropriate for determining the noise characteristics that are influential in homodyne interferometry. In the next two sections, we describe our findings for this specific application area. A 3x3 fiber coupler based homodyne optical coherence tomography system first described by Yaqoob et al. [25] was used to study $1/f$ noise and its impact in homodyne interferometry. This type of system was chosen because of its ability to instantaneously decouple phase and amplitude information [24]. Additionally, the system sensitivity does not depend on maintaining a phase difference of exactly 90° . A calibration procedure, accompanied by appropriate processing, allows us to relax the requirement for stringent phase control in order to use the inherent phase shifts of the fiber coupler.

The experimental setup used here was the same as that described in Chapter 3, diagrammed in Fig. 3.1, and described by Eq. 3.1. For this experiment, the amplitude of the interferometric signal was determined by squaring and summing the signals from the three ports (equivalent to Method 1 in Chapter 3).

The system depicted in Fig. 3.1 was built and calibrated, with phase shifts measured as $\phi_1=116.6 \pm 1.2^\circ$, $\phi_2=120.7 \pm 0.9^\circ$, $\phi_3=122.5 \pm 0.8^\circ$. The objective lens was a 20x, 0.4 NA IR lens, allowing for a measured lateral resolution of 9.4 μm . The broadband SLD source provided a measured axial resolution of 14 μm . A sample arm power of approximately 30 μW , measured at a single detector, was used in all following experiments. In order to experimentally measure the SNR of the homodyne interferometer, time traces of the OCT signal were acquired with a mirror in the sample arm. To measure the noise contribution, the sample arm was blocked. Varying integration times were used to bin the measured signal into integrated ‘blocks’. These ‘blocks’ are represented in Fig. 4.1 by dashed lines with spacing τ , and the integrated signal is proportional to the total number of photons detected over this time interval. The power spectrum of the noise was determined using only the integrated noise signal. The SNR was determined by taking the square of the mean value of the integrated signal divided by the standard deviation of the integrated noise signal

To set a baseline for the evaluation of the effects of 1/f noise on the homodyne system, a heterodyne system was constructed and evaluated as well. The reference mirror labeled in Fig. 3.1 was mounted on a voice coil to allow for modulation of the reference arm optical path length. The interferometric signal was detected at a single port of the fiber coupler, and the envelope of the interferogram was acquired using a lock-in amplifier set at the Doppler shift frequency created by the velocity of the moving reference mirror. Instead of visualizing only a single point, we acquired the entire coherence function in depth as we scanned the reference arm. To measure the SNR we integrated over the central portion of the peak, defined by the full width at half maximum

(FWHM), as well as over the same number of points in an area distant to the peak. The integration time was set by the width of the peak, determined by the speed at which the reference arm was scanned. By changing the scan speed, and locking in on the appropriate carrier frequency, we were able to determine the dependence of the SNR on integration time.

Finally, we were interested in investigating the source of $1/f$ noise in our homodyne interferometer. In order to examine the contribution of detector $1/f$ noise, we replaced our initial detectors (NewFocus, #2011) with new detectors (Thorlabs, #DET10C). We acquired homodyne data as described above, and compared the data sets in terms of the $1/f$ noise characteristics.

One potential problem that was necessary to address involved the discrete sampling of the photodetectors. We wanted to acquire data points that represented the mean signal over the time between subsequent samples, but photodiodes do not integrate over this time period. There was the potential for high frequency noise to skew the data as we integrated over various amounts of time in post processing. To solve this problem, we set the low pass cutoff frequency on the photodetectors to match our sampling rate in all experiments. Thus, fluctuations were smoothed out on the scale of the sampling time. We note that the power spectral density remains constant with or without filtering since the cutoff frequency is found at twice the maximum frequency displayed in the power spectrum.

4.4 Results and Discussion

4.4.1 Measured Power Spectrum

We begin our investigation of $1/f$ noise by displaying the power spectrum of our measured homodyne noise signal averaged over 85 data sets (Fig. 4.5). No capping of the $1/f$ noise at low frequencies can be seen over our measurement range. By fitting to the linear portion of the curve, we found an exponent of $\alpha=1.39\pm 0.1$. The results of the fit also gave us a value for A_{pink} , used in the above derivation. The constant value of the white noise determined A_{white} . Additionally, we note that the frequency at which white noise processes, shot noise in this case, became dominant was approximately 70 Hz.

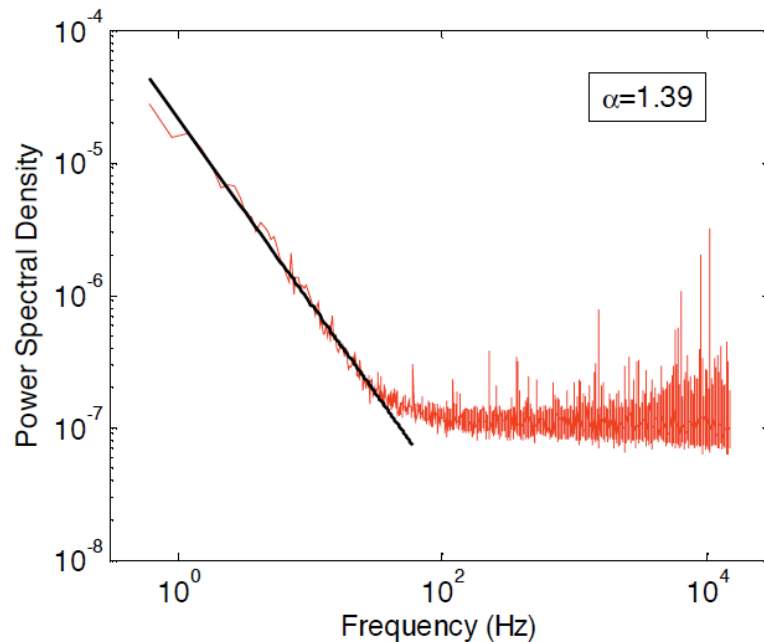


Fig. 4.5. Power spectral density of the interferometric noise, measured with the sample arm blocked. The data were averaged over 85 data sets, and sampled at 30 kHz. The initial portion of the curve was fit, and an exponent of $\alpha=1.39$ was determined. The $1/f$ to white noise corner can be seen at approximately 70 Hz.

4.4.2 Experimental SNR Versus Integration Time

After measuring the SNR of the homodyne system as described above, we plotted SNR versus integration time averaged over 65 data sets in Fig. 4.6. Notably, for short

integration times the curve was approximately linear, while for long integration times the curve was flat. This implies that white noise was initially dominant, and that $1/f$ noise became increasingly prominent as the integration time was increased. This behavior agrees well with the analysis described above and plotted in Figs. 4.2 and 4.3. By fitting to the linear and constant portions of the data in Fig. 4.6 we experimentally determined the integration time at which $1/f$ noise began to dominate as $\tau_{white-to-1/f}=2.1$ ms. The curve was almost completely constant after several 10s of ms, and any further increase in integration time did not significantly increase the SNR. We next compared this result with those from the corresponding heterodyne system, which were collected and analyzed as described in Section 4.3. The use of a carrier frequency shifted our desired signal away from the baseband and out of the $1/f$ regime. This form of detection is the standard method employed for minimizing the contribution of $1/f$ noise when making electronic measurements. The stable range of voice coil frequencies, approximately 1–20 Hz,

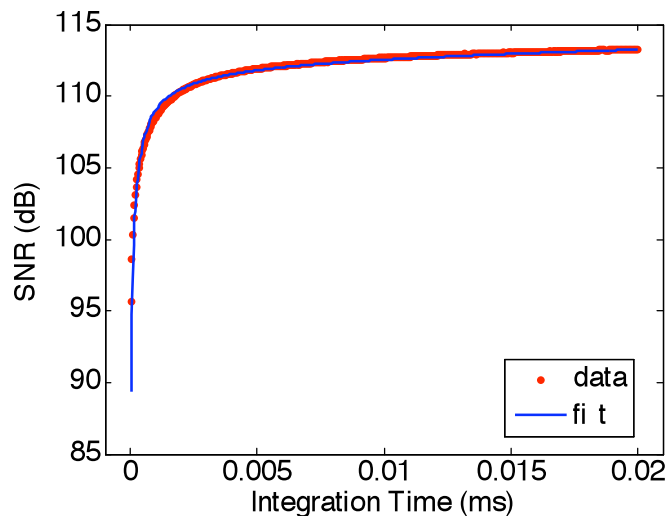


Figure 4.6. SNR of the homodyne interferometric signal plotted versus integration time. The initial portion of the curve displays a linear trend, indicative of dominant white noise processes. The final portion of the curve is constant with increasing integration time, in agreement with the theoretical $1/f$ noise variance derived above.

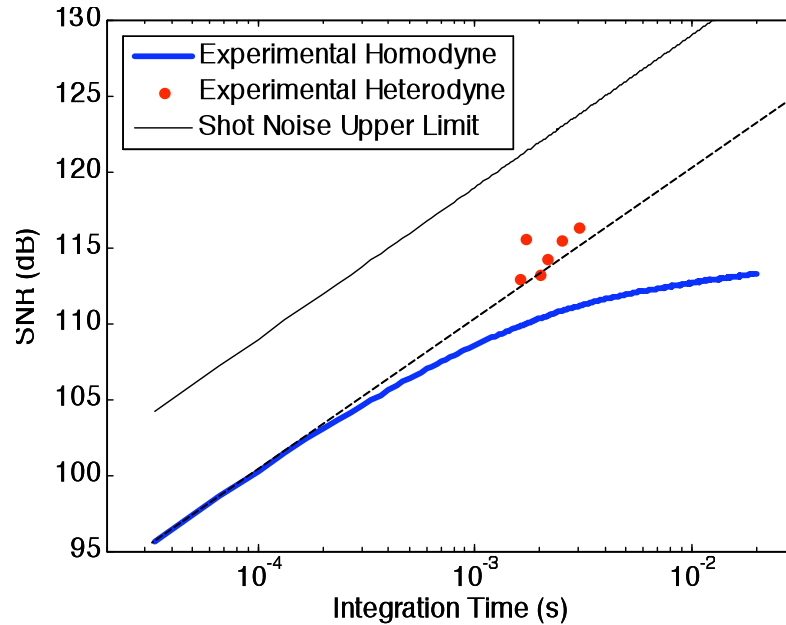


Figure 4.7. A comparison of homodyne (blue) and heterodyne (red) SNR versus integration time. The black curve represents the upper limit on SNR for shot noise limited signals. A line drawn through the initial portion of the homodyne data intersects the heterodyne data (dashed line). This implies that the homodyne data is white noise limited for short integration times, after which $1/f$ noise becomes dominant.

imposed the range of modulation frequencies that we were able to utilize, approximately 5–20 kHz. The voice coil frequency, directly related to the scan speed, set the width of the coherence envelope as well as the integration time of the measurement.

Figure 4.7 displays both heterodyne and homodyne SNR plotted on a log-log scale versus integration time. The homodyne data were averaged over 65 data sets. It is clear that the initial portion of the homodyne data falls along a line that intersects the heterodyne data at longer integration times. This is evidence confirming that the homodyne system is white noise limited for short integration times. The theoretical upper limit on SNR, when white noise is dominant, is plotted in black in Fig. 4.7. This upper shot noise limit assumes perfect constructive interference of the detected signal (i.e., the cosine term in Eq. 3.1 is always equal to 1) and the absence of other white noise sources.

In principle, it is possible to reach this upper limit in homodyne detection when maintaining perfect phase control. In contrast, due to the nature of its time modulation, it is not possible to reach using heterodyne detection since we always detect the coherence function modulated by a fringe pattern.

4.4.3 Characteristic Time

Using the noise model described in Section 4.2, we were able to theoretically predict the characteristic integration time at which 1/f noise began to dominate. However, this calculation required f_{min} . To verify our choice of $f_{min} = 1/T$, we fit the data in Fig. 4.6, sampled at 30 kHz for 1 second to an expression for SNR, including both 1/f and shot noise terms:

$$SNR = \frac{x_0^2 \tau^2}{\sigma_{X,pink}^2 + \sigma_{X,white}^2}. \quad (4.13)$$

Here, $\sigma_{X,pink}^2$ and $\sigma_{X,white}^2$ are given by Eq. 4.9 and Eq. 4.10, respectively. Amplitude values contained in these equations, A_{white} and A_{pink} , were obtained from the power spectrum, as described in Section 4.1. The only free variables in Eq. 4.13 are the total photon count rate, x_0 , and f_{min} , contained in $\sigma_{X,pink}^2$. The fit can be seen in blue in Fig. 4.6. From this fit we determined a f_{min} of 1.1 Hz, which is approximately equal to $1/(T=1s)$. This result helps to confirm the validity of our model for making predictions about experimental results.

With confidence in our value of f_{min} , we used the theoretical noise model to predict the characteristic integration time at which 1/f noise became dominant. This time was determined as the time at which white noise and 1/f noise give an equivalent noise variance, and the following equation holds:

$$\frac{A_{white} \tau}{2} = \int_{\omega_{min}}^{\infty} \frac{A_{pink}}{2\pi^2 f^{\alpha+2}} [1 - \cos(2\pi f \tau)] df. \quad (4.14)$$

We calculated this characteristic time to be $\tau_{white-to-1/f} = 1.65$ ms, and note that the SNR of the measurement should begin to be affected at shorter times when 1/f noise is less than, but not negligible compared to white noise. This time agrees fairly well with our experimentally determined time of 2.1 ms.

4.4.4 1/f Noise Power Dependence

In the initial analysis we arrived at an expression for the variance of the noise amplitude distribution in terms of constants A_{pink} and A_{white} . For shot noise, the constant can be determined using knowledge of Poisson statistics. One question that arises concerns the

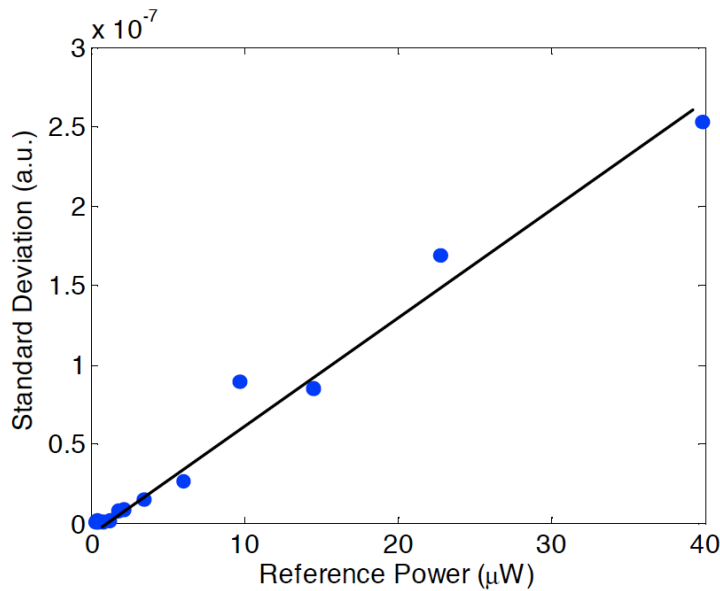


Figure 4.8. The form of the 1/f noise amplitude (A_{pink} in Eq. 4.10) is unknown, although we might expect it to depend on the reference arm power in some fashion. The blue dots represent experimental measurements and the black line is a linear fit to the data. The amplitude was found to follow a linear trend versus reference arm power, similarly to the shot noise amplitude.

form of the constant for $1/f$ noise, A_{pink} . Figure 4.8 shows the dependence of $1/f$ noise on reference arm power. These noise values were computed using an integration time of $\tau=10$ ms, which falls well above the point at which $1/f$ noise becomes dominant in Figs. 4.6 and 4.7. The linear trend in Fig. 4.8 makes intuitive sense; like shot noise, the $1/f$ noise is directly proportional to the number of detected photons.

4.4.5 Sources of $1/f$ Noise

Finally, we examined the contribution of the photodetectors to $1/f$ noise in the interferometric system. We expect a different set of photodetectors to have different $1/f$ characteristics, and possibly different exponents, α . The initial detectors (New Focus #2011) showed a linear trend of $\alpha=1.40$, while the replacement detectors (Thorlabs #DET10C) displayed an increase to $\alpha=2.17$. The power spectra are plotted in Figs. 4.9 (a) and (b). We expect the shot noise limited SNR curve to be similar between both sets of detectors since the photon count rate remained the same. Using the results of our theoretical analysis plotted in Figs. 4.2 and 4.3, we expect that $1/f$ noise with a higher exponent will intersect the shot noise curve at a shorter integration time. These expectations are verified by comparing the experimental SNR versus integration time for the two sets of detectors. Although the two curves look very similar in the shot noise regime, the signals from Thorlabs detectors begin to shift from a linear shot noise curve to a flat $1/f$ noise curve almost an order of magnitude earlier than those of the New Focus photodetectors. These results emphasize the importance of careful detector selection in minimizing $1/f$ noise for optical systems.

In addition to detector noise, there is a component of the $1/f$ noise that arises from the light source. A portion of the noise was removed by subtracting the detected signal at

D4 from the signals at the other three ports. When this subtraction was not performed, we found a difference in SNR similar to that displayed in Fig. 4.9(c) where $1/f$ noise caused the SNR curve to flatten out at shorter integration times. This result was less dramatic than that in Fig. 4.9(c), with a maximum difference of approximately 3 dB between the data that had and had not been corrected using the signal from D₄. We note that this type of correction, commonly used to reduce excess intensity noise [14], is also an important factor in reducing $1/f$ noise.

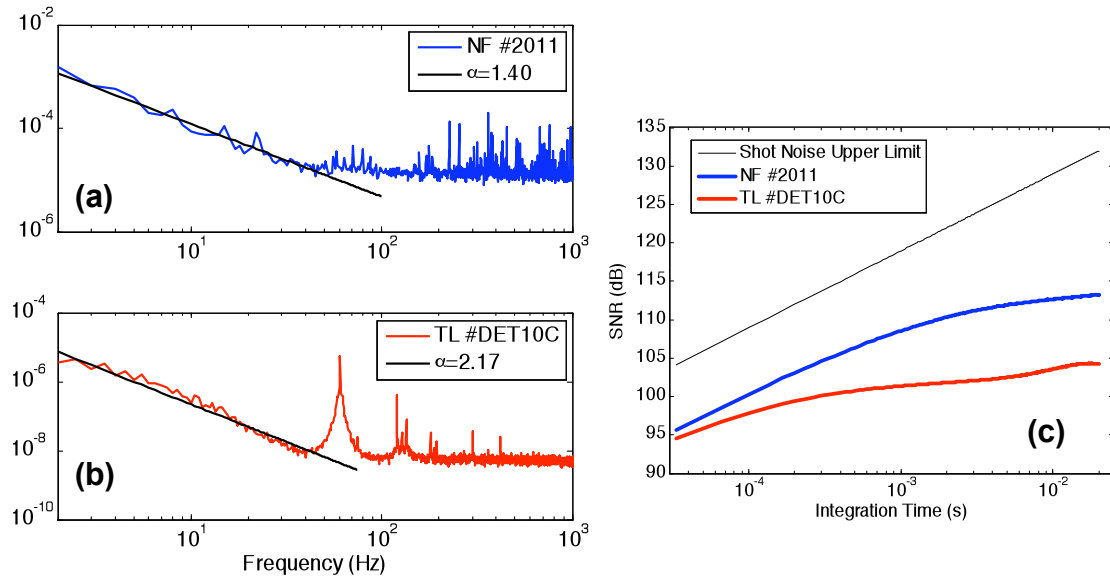


Figure 4.9. Power spectra of initial detectors (a), and replacement detectors (b), showing a notable increase in the $1/f$ noise exponent, α . c) SNR versus integration time for both sets of detectors. The larger $1/f$ exponent of the Thorlabs detectors (TL #DET10C) caused $1/f$ noise to become a dominant process for shorter integration times than was seen in the New Focus detectors (NF #2011).

4.5 Conclusions

In conclusion, we have presented what is, to the best of our knowledge, a novel time domain method for analysis of the dependence of the noise variance on the integration time of the detection system. While we used this model to investigate $1/f$ noise in a homodyne interferometry system, it is applicable for any optical detection scheme in

which the power spectrum of the noise fluctuations is known. We confirmed the validity of our model by demonstrating that our results are consistent with the well known dependence of white noise on integration time. The solutions to our model were found to be dependent on a minimum frequency, f_{min} , which was inversely related to the total time frame of the experiment. By restricting this total time frame it is possible to exclude large amplitude, low frequency components from the acquired signal. Our analysis revealed that the variance of the 1/f noise amplitude distribution shows two distinct regimes. For $0 < \alpha < 1$, the noise variance is dependent on $\tau^{\alpha+1}$, representing a transition from white noise to 1/f noise. However, for $\alpha > 1$, the noise variance is dependent on τ^2 , implying that when the dominant noise processes display a 1/f characteristic, the SNR of the measurement is constant versus integration time. The presence of both white and 1/f noise sources suggests the existence of a characteristic integration time, beyond which 1/f noise dominates and the SNR can no longer be significantly improved by increasing integration time.

We experimentally characterized the 1/f noise of our homodyne interferometer, finding a 1/f exponent of $\alpha = 1.39 \pm 0.1$ and a 1/f noise corner of approximately 70 Hz. Experimental data confirmed our theoretical results, showing that the measured SNR tapers to a constant value in the 1/f dominated regime. For short integration times, white noise processes were dominant. We have established white noise limited detection for short integration times by comparing our homodyne SNR to the SNR of the corresponding heterodyne interferometer, as well as to theory. Our experimental results demonstrated a characteristic integration time for our homodyne OCT interferometer, of $\tau_{white-to-1/f} = 2.1$ ms, beyond which increases in integration time did not produce

corresponding increases in SNR. This time agrees fairly well with the theoretically determined value of $\tau_{white-to-1/f} = 1.65$ ms based on the measured power spectral characteristics of system. This characteristic time depends on the $1/f$ characteristics of the optical system, and is both system and detector dependent. Finally, we note that careful photodetector selection and characterization is important in order to minimize $1/f$ noise in homodyne detection.

Chapter 5. Dark 1/f Noise in Direct Detection Schemes

This chapter is adapted from Ref (92): E.J. McDowell, J. Ren, and C. Yang, 'Fundamental sensitivity limit imposed by dark 1/f noise in the low optical signal detection regime,' Optics Express, 16(10), 6822–6832 (2008).

5.1 Introduction

The ability to detect very low amplitude optical signals is important and relevant in a variety of measurement scenarios. The detection of light from a distant star is an example. Additionally, many biomedical imaging techniques depend on measuring very weak optical signals, including second harmonic generation, Raman scattering, and single molecule fluorescence. For an ideal measurement system that contains only white noise sources, it is possible to measure any arbitrarily small signal by simply increasing the integration time of the detection system. However, this may not be possible in certain situations due to the presence of 1/f noise. In this chapter, we will theoretically determine the detection limit imposed by 1/f noise, specifically dark 1/f noise, in direct low optical signal detection schemes.

In order to enable the detection of weak signals, it is common to use highly sensitive detectors such as photomultiplier tubes (PMTs) or avalanche photodiodes (APDs). PMTs utilize a combination of high gain, low noise, high frequency response, and

large collection area (93) to achieve high sensitivity. APDs can be thought of as the semiconductor analog to a PMT.

Noise in optical detection is a combination of the intrinsic noise associated with a flow of photons, as well as noise associated with the detector. In the shot noise limit, noise related to the discrete arrival time of photons dominates all other noise processes. This limit represents an optical system functioning in an optimal manner, as the total noise of the detection process can never be reduced below the intrinsic shot noise level (without resorting to manipulation of the photon statistics). It is also possible for an optical system to operate such that detector noise is dominant. In broad terms, detector noise can be divided into two categories: dark noise and bright noise. Bright noise can arise as multiplicative noise caused by gain fluctuations and randomness in the carrier multiplication process of the PMT or APD (94), among other possible sources. In other words, if put N photons on a detector, the count we receive will fluctuate around the mean value of eN (e is the detector efficiency) due to randomness in the signal conversion process; this fluctuation comprises bright noise. Dark noise describes the random signal count from a detector that is blocked from receiving any optical signals. Among other causes, this can arise from thermally induced fluctuations and other additive noise sources in the detector. In the presence of a weak or absent input light field, bright noise can be neglected and dark noise dominates. As the focus of this study is centered on scenarios where the input light field is weak, we are primarily interested in the detector dark noise, specifically the dark $1/f$ noise.

Interestingly, the typical noise characteristics specified for high sensitivity optical detectors, including the noise equivalent power / bandwidth (NEP, NEB), reflect only the

white noise portion of the dark noise. We note that such a characterization is incomplete, as the detector circuitry, among other potential sources, necessarily contributes dark $1/f$ noise. In the presence of dark $1/f$ noise, such devices will deviate from their predicted performance in which only dark white noise is accounted for. Our goal in this chapter is to quantify this deviation. In particular, we will study the impact of dark $1/f$ noise on the fundamental sensitivity limit imposed by the detector that, to our knowledge, has never been studied or analyzed. This analysis is distinct from and complementary to our previous study (65) of the impact of $1/f$ noise in homodyne interferometric systems where 1) bright, rather than dark, detector noise was dominant, and 2) the noise analysis focused on the correct reception of a time varying signal trace rather than a confirmation of the existence of a signal source.

In this chapter we first give a general description of $1/f$ noise, as well as several relevant studies of its effect in detection systems. We then define the specific problem that we are considering in this work. Next, we demonstrate the relevance of this analysis by experimentally showing that dark $1/f$ noise exists in practical detectors. The remainder of the chapter is intended to be purely theoretical. We derive an expression for the SNR of the measurement of interest. We then show the results of our analysis and discuss the application of these results to experimental scenarios. We conclude by placing these results in context with our previous study (65), and provide a generalized guide for characterizing $1/f$ noise that is useful for a broad range of optical detection applications.

5.2 Background

1/f noise, alternately referred to as pink or flicker noise, can be found in a wide range of physical systems (66-68). Generally, 1/f noise is represented by a power spectral density (PSD) that follows the form $1/f^\alpha$, where α commonly ranges from 0.5 to 1.5 (73). The origins of 1/f noise sources are not well understood. In fact, a 1/f power spectrum can arise from very different time traces (sharp bursts versus slower baseline drifts of the system). The origins of these noise sources are not the focus of this work. In the context of our analysis of detection sensitivity, it is sufficient to quantitatively characterize 1/f noise based on empirical data without seeking the exact nature of the noise source.

For white noise sources, we expect the deviation in the signal (or noise) count to scale as the square root of the signal (or noise) count. It is this deviation, rather than the noise count itself, that limits detector sensitivity. This point will be more explicitly clarified later, but an intuitive understanding of this issue is not hard to grasp through the following example. Suppose we have a unity efficiency detector that is known to have an average dark white noise count rate of x photon/s. This implies that if we want to detect the presence of a weak light source (photon rate of y photon/s) with this detector in a measurement made over T seconds, we must make sure that the total signal count (yT) exceeds the noise deviation term (\sqrt{xT}) rather than the total expected dark count (xT).

1/f noise differs from white noise in two distinct ways. First, 1/f noise differs in its dependence on the integration time of the detection system, which we will derive in this chapter. Secondly, 1/f noise is dependent on an additional intrinsic factor, the noise exponent, α , which can vary from noise source to noise source.

Several published works have attempted to characterize the effects of $1/f$ noise on detection systems. Allan (95) has shown that there is a relationship between the PSD of the fluctuating phase of an atomic frequency standard and the variance of its frequency deviation. To derive this relationship, the variance of the frequency deviation is written in terms of the autocorrelation function of the phase, which can be related to the PSD of the phase using the Wiener-Khinchin Theorem. Allan's work illustrates a way to characterize the PSD of a random process through a statistically measurable quantity — the variance of a group of samples, where each sample is the time averaged value of the random variable over a given time period. The relationship between the variance and the PSD derived by Allan depends on the averaging time period, the dead time between samples, and the number of samples within the group. In a later work (96), the model was further generalized, and an analytical expression for the relationship was strictly proved.

More recently, we have described and verified a quantitative noise model to study the effect of $1/f$ noise in homodyne interferometers (65), as described in Chapter 4. Our goal in doing so was essentially the opposite of Allan's. Our aim was to use the PSD of a noise source (which is measurable) to find the noise variance of a specific measurement we wish to make. In doing so we are then able to predict the signal-to-noise ratio (SNR) of the measurement. This quantitative noise model represents the noise in the system in a time domain format as a sum over all possible frequencies. Each frequency is represented by a sinusoidally varying term, weighted by the value of the PSD at that frequency. The phase of each term is random with respect to that of all other frequencies, essentially representing any and all possible time traces that can result from a superposition of those

frequencies. Using this time domain representation, we were able to evaluate the noise variance that we would expect given the PSD of the noise source.

We further note that the $1/f$ noise studied in Ref. (65) was bright in nature rather than dark, as the reference beam of the homodyne interferometer was always incident on the detector. This strong light field precluded any significant dark noise contributions in that scenario.

5.3 Problem Statement

Suppose we wish to confirm the existence of a weak light source, using a detector with dark noise power spectral density $S(f)$, determined *a priori*, and a mean dark noise count rate x_{noise} . For the sake of clarity, we choose to quantify our signal in terms of photon count rate (x) and photon counts (X). We can assign a signal count rate of x_{signal} , attributed to the presence of the weak light source; in the weak source regime, $x_{noise} \gg x_{signal}$. If we are given a time frame of T to detect the presence of the weak light source, we can perform an experiment by first blocking the detector and measuring the dark noise count ($X_{noise}(\tau)$) for a time period of $\tau = T/2$, then exposing the detector to the weak light source and measuring the combination of dark noise and signal for an equivalent time period ($X_{signal+noise}(\tau = T/2)$). Our goal is to determine, based on the PSD of the noise, whether or not it is possible to discriminate the presence of x_{signal} from this measurement.

Experimentally, the power spectrum, $S(f)$, of the detector noise can be determined *a priori* by 1) acquiring a measurement trace from the detector in the dark (where the time duration of the trace is much longer than any experiments we wish to perform), 2) computing the autocorrelation function, and 3) finding the Fourier transform of the

autocorrelation function. A realistic model for an optical detector involves modeling $S(f)$ as a sum of mutually independent white and $1/f$ noise. By relating the variance of a measurement, $X(\tau)$, to the power spectrum of the detector, $S(f)$, we can assess the impact of $1/f$ noise.

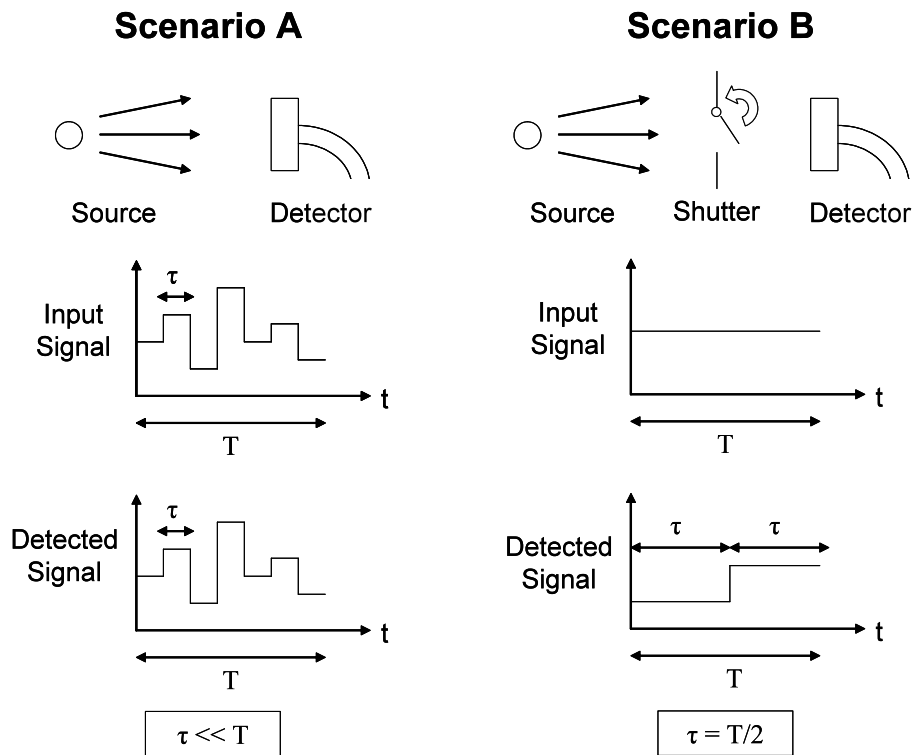


Figure 5.1. A comparison between the measurement schemes in Chapter 3 (Scenario A) and the current work (Scenario B). In Scenario A, an amplitude modulated message is transmitted in steps of duration τ over a total time T . In this work, we simply wish to confirm the presence of the light source in an experiment where both signal and noise are measured for equivalent time periods.

It is evident that our measurement scenario is quite different from that analyzed in our previous noise study (Ref. (65)) for a homodyne interferometer. In that study, a strict assumption was made regarding the relationship between the integration time (τ) and the total time frame of the experiment (T). This assumption, $\tau \ll T$, is relevant in certain scenarios; for example, the case in which a transmitter is transmitting a message of

duration T , where the signal varies over each time step, τ . (Fig. 5.1(a)). The experimental scenario examined in the current study is different in that our signal collection time frame is comparable to the total experimental time frame. A naïve extension of the result of Ref. (65) will not achieve the correct result for this particular detection scheme. Here, instead of receiving an amplitude modulated message, we simply wish to find the limit in which we can detect the presence of the transmitter in the first place. Experimentally, this corresponds to data obtained by alternate measurements of signal and noise (Fig. 5.1(b)), as we have described above.

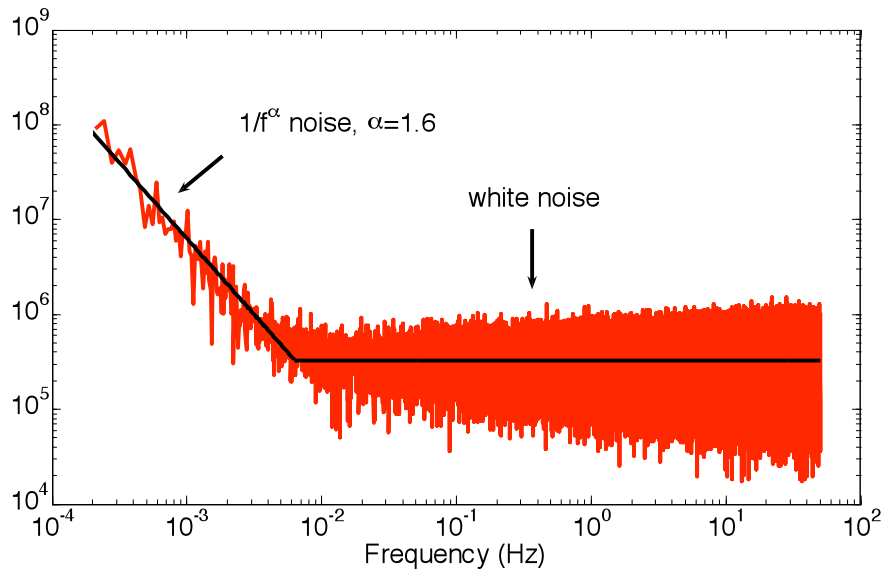


Figure 5.2. Power spectral density of the dark noise count of a photon counting APD. $1/f$ noise is visible at and below frequencies in the mHz range. This averaged trace displays an α value of 1.6.

5.4 Experimental Verification

To confirm that dark $1/f$ noise does indeed exist in sensitive optical detectors, we measured the power spectral density of the dark count of an APD (Perkin-Elmer, SPCM-A2R15) over approximately 3 hours and plotted the result, averaged over 6 traces, in Fig.

5.2. We see that the noise spectrum can be well described as a combination of dark white and 1/f noise, with 1/f noise visible at and below frequencies in the mHz range.

Figure 5.2 shows that an α value of 1.6 was measured from the PSD of this particular APD. As our results in Ref. (65) showed that the noise exponent factor is highly device dependent for bright 1/f noise, it is possible that the α value for dark 1/f noise may vary significantly from device to device. The model that we present in this here is applicable for any system with $\alpha > 0$. We advise readers who intend to use our model in their respective applications to characterize their detectors via the above approach and calculate the corresponding α values.

5.5 Theory

Given a measurement of the PSD of our detector dark noise, it is possible to derive the expected SNR of future measurements made with this detector. Our noisy signal can be described, in terms of photon count rate, as:

$$x(t) = x_{signal} + \Delta x(t), \quad (5.1)$$

where $\Delta x(t)$ represents the fluctuating noise. In our experiment, we make measurements of the signal and noise photon count over a time period, τ :

$$X_{noise}(\tau) = \int_0^{\tau} \Delta x(t) dt, \quad (5.2)$$

$$X_{signal + noise}(\tau) = \int_{\tau}^{2\tau} (x_{signal} + \Delta x(t)) dt. \quad (5.3)$$

In the context of this thought experiment, we wish to determine when the difference between the measurements described above gives a statistically significant result.

Explicitly, we want to know when the difference between the mean signal and noise values is greater than the standard deviation of the measurement:

$$E[X_{\text{signal} + \text{noise}}(\tau) - X_{\text{noise}}(\tau)] > \sigma[X_{\text{signal} + \text{noise}}(\tau) - X_{\text{noise}}(\tau)]. \quad (5.4)$$

The expected value of the left hand side of Eq. 5.4 is simply given by $x_{\text{signal}}\tau$. We can derive an expression for the variance of this measurement, the square of the right hand side of Eq. 5.4, as follows:

$$\sigma^2[X_{\text{signal} + \text{noise}}(\tau) - X_{\text{noise}}(\tau)] = E\left[\left(\int_{\tau}^{2\tau} \Delta x(t) dt - \int_0^{\tau} \Delta x(t) dt\right)^2\right]. \quad (5.5)$$

It can be seen from Eq. 5.5 that very low frequency components of Δx , which will essentially contribute the same number of photons to each integral, will cancel each other out. Thus, there is no dependence on the minimum measurable frequency, or alternately the total time frame of the experiment. We can combine the two integrals by making a change of variables:

$$\sigma^2(X_{\text{signal} + \text{noise}} - X_{\text{noise}}) = E\left[\left(\int_0^{\tau} (\Delta x(t + \tau) - \Delta x(t)) dt\right)^2\right]. \quad (5.6)$$

This expression can be rewritten as:

$$\begin{aligned} & \sigma^2(X_{\text{signal} + \text{noise}} - X_{\text{noise}}) \\ &= E\left[\int_0^{\tau} \int_0^{\tau} \Delta x(t_1 + \tau) \Delta x(t_2 + \tau) dt_1 dt_2 + \int_0^{\tau} \int_0^{\tau} \Delta x(t_1) \Delta x(t_2) dt_1 dt_2 - 2 \int_0^{\tau} \int_0^{\tau} \Delta x(t_1 + \tau) \Delta x(t_2) dt_1 dt_2\right] \\ &= \int_0^{\tau} \int_0^{\tau} E(\Delta x(t_1 + \tau) \Delta x(t_2 + \tau)) dt_1 dt_2 + \int_0^{\tau} \int_0^{\tau} E(\Delta x(t_1) \Delta x(t_2)) dt_1 dt_2 - 2 \int_0^{\tau} \int_0^{\tau} E(\Delta x(t_1 + \tau) \Delta x(t_2)) dt_1 dt_2 \\ &= 2 \int_0^{\tau} \int_0^{\tau} R(t_1 - t_2) dt_1 dt_2 - 2 \int_0^{\tau} \int_0^{\tau} R(t_1 - t_2 + \tau) dt_1 dt_2 \end{aligned} \quad (5.7)$$

where $R(t')$ is the autocorrelation function and can be related to the PSD through the Wiener-Khinchin theorem as follows: $R(t') = \int_0^{\infty} S(f) \cos(2\pi f t') df$, for a single-sided

power spectrum, $S(f)$. For readers that are more familiar with a double-sided power spectrum, we note that the single sided power spectrum simply folds the negative side of the even double sided power spectrum onto the positive frequency axis.

Eq. 5.7 can be evaluated as:

$$\begin{aligned}
& \sigma^2(X_{\text{signal+noise}} - X_{\text{noise}}) \\
&= 2\text{Re} \left[\int_0^\infty \int_0^\tau \int_0^\tau S(f) e^{i2\pi f(t_1-t_2)} df dt_1 dt_2 - \int_0^\infty \int_0^\tau \int_0^\tau S(f) e^{i2\pi f(t_1-t_2+\tau)} df dt_1 dt_2 \right] \\
&= 2\text{Re} \left[\int_0^\infty \int_0^\tau \int_0^\tau S(f) e^{i2\pi f(t_1-t_2)} (1 - e^{i2\pi f\tau}) df dt_1 dt_2 \right] \\
&= 2\text{Re} \left[\int_0^\infty S(f) (1 - e^{i2\pi f\tau}) \left(\int_0^\tau e^{i2\pi f t_1} dt_1 \right) \left(\int_0^\tau e^{-i2\pi f t_2} dt_2 \right) df \right] \\
&= 2\text{Re} \left[\int_0^\infty S(f) (1 - e^{i2\pi f\tau}) \frac{1}{(2\pi f)^2} (e^{i2\pi f\tau} - 1)(e^{-i2\pi f\tau} - 1) df \right] \\
&= 2\text{Re} \left[\int_0^\infty S(f) (1 - e^{i2\pi f\tau}) \frac{1}{(\pi f)^2} \sin^2(\pi f\tau) df \right] \\
&= 2\text{Re} \left[\int_0^\infty S(f) e^{i\pi f\tau} (e^{-i\pi f\tau} - e^{i\pi f\tau}) \frac{1}{(\pi f)^2} \sin^2(\pi f\tau) df \right] \\
&= 2\text{Re} \left[\int_0^\infty S(f) e^{i\pi f\tau} (-2i) \frac{1}{(\pi f)^2} \sin^3(\pi f\tau) df \right] \\
&= 2\text{Re} \left[\int_0^\infty S(f) (\cos(\pi f\tau) + i \sin(\pi f\tau)) (-2i) \frac{1}{(\pi f)^2} \sin^3(\pi f\tau) df \right] \\
&= 4 \int_0^\infty \frac{S(f)}{(\pi f)^2} \sin^4(\pi f\tau) df
\end{aligned} \tag{5.8}$$

From here, the power spectral density of the dominant noise source can be used to determine the expected noise variance, as well as the expected SNR of a measurement given knowledge of the signal amplitude. For dominant dark white noise, $S(f)$ is a constant, A_{white} . The resulting noise variance and corresponding SNR are determined (using Eq. 3.822.12 and 3.828.13 of Ref. (97)) to be:

$$\sigma_{white}^2(\tau) = \int_0^{\infty} \frac{4A_{white}}{\pi^2 f^2} \sin^4(\pi f \tau) df = A_{white} \tau, \quad (5.9)$$

$$SNR_{white} = \frac{x_{signal} \sqrt{\tau}}{\sqrt{A_{white}}}. \quad (5.10)$$

We can see that for a dark white noise limited signal, any arbitrarily small x_{signal} can be detected using a sufficiently long collection time, τ .

As we alluded to previously in this chapter, the same is not true for the case of dominant dark 1/f noise. Here, we substitute a power spectrum of the form: $S(f) = A_{1/f}/f^\alpha$, and find a noise variance of the form:

$$\sigma_{1/f}^2(\tau) = \int_0^{\infty} \frac{4A_{1/f}}{\pi^2 f^{2+\alpha}} \sin^4(\pi f \tau) df. \quad (5.11)$$

This result can be reduced to the following form:

$$\sigma_{1/f}^2(\tau) = A_{1/f} C \tau^{1+\alpha}, \quad (5.12)$$

$$C = (2^{2+\alpha} - 2^{1+2\alpha}) \pi^{\alpha-1} \Gamma(-1-\alpha) \sin\left(\frac{\alpha\pi}{2}\right) \quad \alpha > 0, \quad \alpha \notin Z,$$

$$SNR_{1/f} = \frac{x_{signal} \tau}{\sqrt{A_{1/f} C \tau^{1+\alpha}}} = \frac{x_{signal} \tau^{(1-\alpha)/2}}{\sqrt{A_{1/f} C}}. \quad (5.13)$$

Here, Γ represents the Gamma function. The derivation required for simplifying Eq. 5.11 makes use of known integral forms, including Eq. 3.756.4 and 3.756.9 in Ref. (97). This solution holds for any non-integer value of α that is greater than zero. We can clearly see the dependence of the noise variance on the integration time, τ . Interestingly, we see from the SNR expression that for $\alpha > 1$ we actually expect the SNR to decrease as a function of integration time.

Thus far, we have derived expressions for the noise variance given either white or 1/f noise. Since these two noise sources are independent of one another, we can describe the total noise variance as the sum of the individual variances, allowing us to examine the SNR that we might expect from a realistic optical system:

$$\sigma_{total}^2(\tau) = A_{white} \tau + A_{1/f} C \tau^{1+\alpha}, \quad (5.14)$$

giving a combined SNR of:

$$SNR = \frac{x_{signal} \tau}{\sqrt{A_{white} \tau + A_{1/f} C \tau^{1+\alpha}}} = \frac{x_{signal} \sqrt{\tau}}{\sqrt{A_{white} + A_{1/f} C \tau^\alpha}}. \quad (5.15)$$

This expression combines two competing terms: white noise dominated SNR, which will improve with increasing integration time, and 1/f noise dominated SNR, which will decrease (for $\alpha > 1$). The combination of these two noise sources suggests that the SNR will increase to a maximum value before beginning to decrease with integration time. More importantly, the presence of this maximal SNR value implies that there is a limit on the smallest x_{signal} that can be detected with such a system. The integration time at which the maximal SNR is achieved can be determined by solving for the time at which the derivative of the SNR expression is equal to zero. This results in an expression for τ of the following form:

$$\tau_{opt} = \left[\frac{A_{1/f} C}{A_{white}} (-1 + 2\alpha) \right]^{-1/\alpha}, \quad (5.16)$$

where we can clearly see that the optimal integration time is a function of the relative amplitudes of dark 1/f and white noise in the system.

5.6 Results

In the following paragraphs we will examine the behavior of the SNR expression in Eq. 5.15 as a function of α , as well as the relative amplitudes of white and 1/f noise. Figure 5.3 shows the SNR as a function of integration time for α values ranging from 0.4 to 1.6. We chose to fix the relative amplitudes of white and 1/f noise at $A_{1/f}/A_{white}=0.01$ for the purpose of this illustration. For $\alpha < 1$, the SNR steadily increases as a function of integration time, however at a slower slope as α nears 1. For $\alpha > 1$, the SNR curve reaches a maximum value and begins to decrease as a function of integration time.

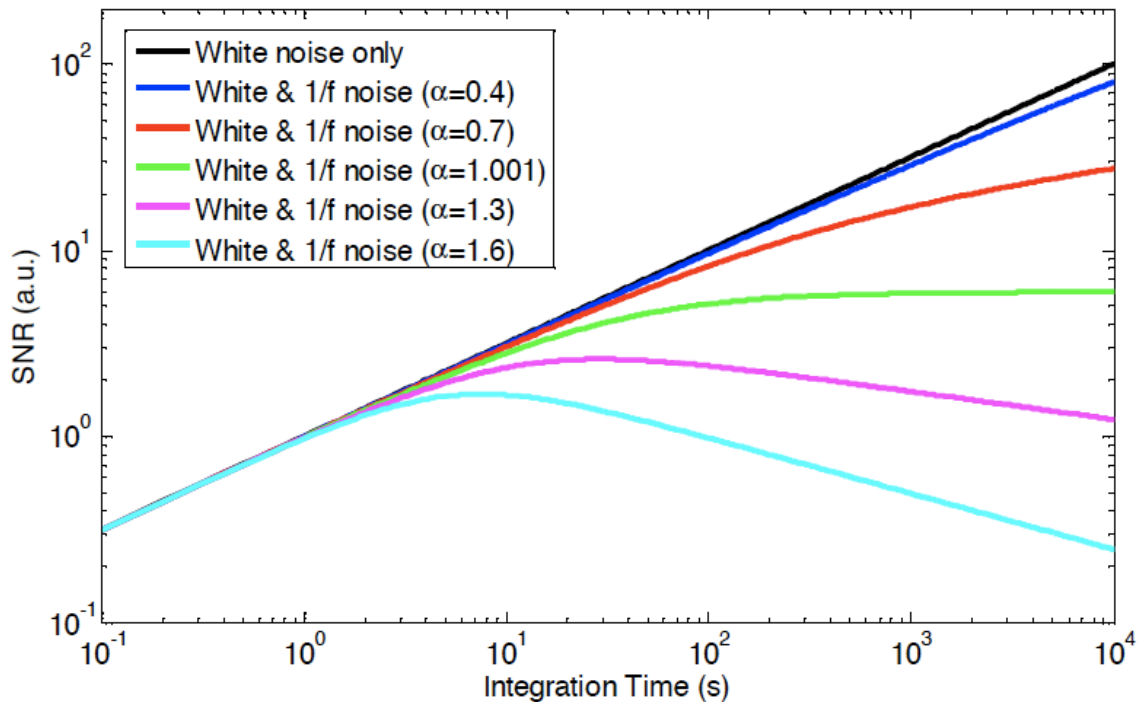


Figure 5.3. SNR versus integration time for a combination of white noise and 1/f noise with α values ranging from 0.4 to 1.6 ($A_{1/f}/A_{white}=0.01$). The slope of the SNR trace decreases with increasing α . For $\alpha > 1$, the SNR reaches a peak value and begins to decrease with increasing integration time. The existence of a peak SNR value implies that there is a limit on the smallest signal that the system is capable of measuring.

The location of the maximal SNR value is dependent on the relative amplitudes of white and 1/f noise (Eq. 5.16). Figure 5.4 shows SNR traces for a fixed α value of 1.6. As

$A_{1/f}/A_{white}$ is increased, we see the location of the maximal SNR (indicated by stars) moving toward shorter integration times. The dashed curve in Fig. 5.4 corresponds to an SNR trace that we might expect from the photon counting APD described above. The power spectrum in Fig. 5.2 was used to determine noise amplitude values ($A_{1/f}/A_{white}=3.03\times 10^{-4}$). This curve shows that the optimal integration time for the APD is approximately 50 s. Any further increase in integration time beyond this point will no longer improve the SNR.

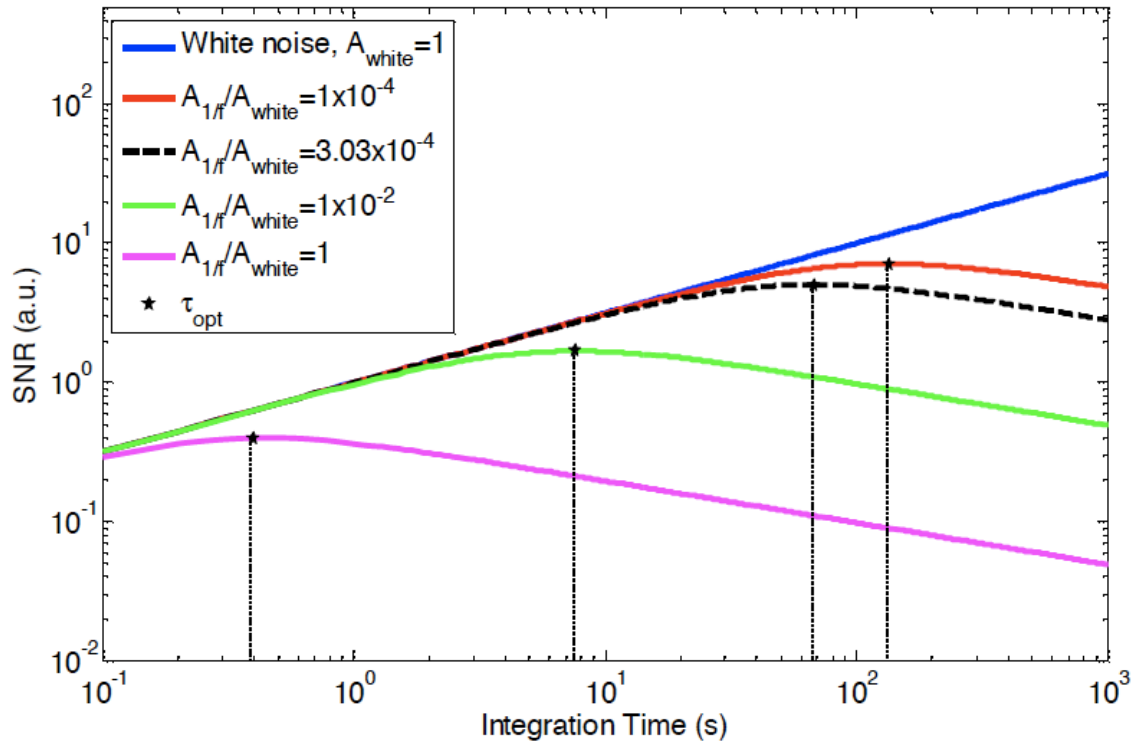


Figure 5.4. The location of the peak SNR value is dependent on the relative amplitudes of white and $1/f$ noise. As $A_{1/f}/A_{white}$ is increased (for fixed $\alpha=1.6$), the location of the maximum SNR, denoted by stars, moves towards shorter integration times. Curve fitting to the data shown in Fig. 5.2 we find $A_{1/f}/A_{white} = 3.03\times 10^{-4}$ for the photon counting APD described. The dashed curve shows an SNR trace corresponding to this value, with an optimal integration time of ~ 50 seconds.

5.7 Discussion

5.7.1 Summary of Analysis

With the exception of Ref. (65), none of the studies mentioned above have applied their results to fundamental detection sensitivity in optical systems. The progression of our analysis (in terms of photon counts) and form of our solutions (in terms of SNR) are of direct and practical relevance for optical engineering. To our knowledge, this is the first study of the impact of $1/f$ noise in low optical signal direct detection schemes where dark noise dominates over other noise sources. We reinforce the fact that the thought experiment described here is different in implementation from the homodyne detection experiment in Ref. (65), as described in detail above. Although the two analyses give similar results for white noise dominated signals, the results in the presence of $1/f$ noise differ significantly. Ref. (65) showed that the SNR corresponding to Scenario A of Fig. 1 increased with increasing integration times before tapering to a constant value. In the current work, we have found that the SNR corresponding to Scenario B of Fig. 1 increases to a maximum before beginning to decrease with increasing integration times (for $\alpha > 1$).

The results of this analysis speak to the importance of careful photodetector selection. It is preferable to choose a detector with as small an α as possible. If α is less than 1, the detector is still capable of offering improved SNR with increasing integration time. If α is greater than one, there is a fundamental sensitivity limit associated with the detector that cannot be improved by increasing the signal integration time. Nevertheless, it is still desirable to aim for as small an α value as possible, as this will result in a broader peak in the SNR versus integration time curve. A broader peak implies that there is a broader range of integration times at which a high SNR can be obtained. In

summary, the selection of a detector with a small α value is an important consideration when designing a weak signal detection system.

5.7.2 Application of Analysis

The present work and our previous work (Ref. (65)) are complementary and widely applicable for noise characterization of detection schemes. The present work analyzes the fundamental detection limit in the context of dominant dark white and 1/f noise, but can

	Scenario A	Scenario B
Measurement	X_{signal}	$X_{\text{signal+noise}} - X_{\text{noise}}$
White Noise Variance	$\sigma_{\text{white}}^2(\tau) = \frac{1}{2} A_{\text{white}} \tau$	$\sigma_{\text{white}}^2(\tau) = A_{\text{white}} \tau$
1/f Noise Variance	$\sigma_{1/f}^2(\tau) \approx A_{1/f} B \tau^{\alpha+1}$ for $\alpha < 1, \alpha \notin Z$ $\sigma_{1/f}^2(\tau, T) \approx A_{1/f} \left[\frac{\tau^2 T^{\alpha-1}}{\alpha-1} \right]$ for $\alpha > 1, \alpha \notin Z$	$\sigma_{1/f}^2(\tau) = A_{1/f} C \tau^{1+\alpha}$ for $\alpha > 0, \alpha \notin Z$
Combined SNR	$SNR(\tau) \approx \frac{x_{\text{signal}} \sqrt{\tau}}{\sqrt{A_{\text{white}} + A_{1/f} B \tau^\alpha}}$ for $\alpha < 1, \alpha \notin Z$ $SNR(\tau, T) \approx \frac{x_{\text{signal}} \sqrt{\tau}}{\sqrt{A_{\text{white}} + \frac{A_{1/f} \tau T^{\alpha-1}}{\alpha-1}}}$ for $\alpha > 1, \alpha \notin Z$	$SNR = \frac{x_{\text{signal}} \sqrt{\tau}}{\sqrt{A_{\text{white}} + A_{1/f} C \tau^\alpha}}$ for $\alpha > 0, \alpha \notin Z$

Table 51. A comparison of the important equations in both Chapter 4 (Scenario A) and the current study (Scenario B). The white noise variance is almost identical, regardless of the measurement scheme employed. In contrast, the 1/f noise variance differs in both its dependence on the integration time (τ), as well as its dependence on the total time frame of the experiment (in Scenario A only). The constant of proportionality, B is given by: $(2\pi)^\alpha / (2\alpha(\alpha+1)\Gamma(\alpha)\cos(\alpha\pi/2))$, and C can be found in Eq. 5.12 above.

also be used in scenarios where bright white and $1/f$ noise dominate (such as in homodyne or heterodyne detection). Our previous work (Ref. (65)), focused on the detection of a signal stream, was performed in the context where bright white and $1/f$ noise dominate, but, likewise, can be adapted for use in scenarios where dark white and $1/f$ noise dominate. Table 5.1 outlines the major results from the two analyses.

This sub-section aims to provide a recipe for choosing between the two analyses and appropriately applying them to specific detection scenarios. The steps are as follows:

Step 1: Determine if you are a) trying to confirm the existence of a light source or b) trying to receive a signal stream. Figure 1 can aid in your judgment.

Step 2: Obtain a detector time trace. This consists of acquiring a measurement trace from the detector with no useful optical signal incident on the detector. If you expect your experiment to be dominated by dark noise, this implies blocking all light from reaching the detector. If you expect your experiment to be dominated by bright noise, this implies only permitting background light power to reach the detector (such as the reference power in a heterodyne or homodyne interferometric system). The time duration for the trace should be much longer than the time frame of any experiments you wish to perform with the detector.

Step 3: Calculate the noise PSD by computing the autocorrelation function of the time trace, then finding the Fourier transform of the autocorrelation function.

Step 4: Extract the white and $1/f$ noise components from the noise PSD curve. The amplitudes of the two noise terms, as well as the α value of the $1/f$ noise term, should be determined.

Step 5: Compute the noise variances. For scenario A, you need the values calculated in Step 4, the detection integration time associated with each signal time step, t , and the time

frame of the experiment, T . Use Eq. 9 and 10 of Ref. (65) (Eqs. 4.9 and 4.10 of this thesis). For scenario B, you need the values calculated in Step 4 and the detection integration time, t . Use Eq. 5.9 and 5.11 of this work.

Step 6: Calculate the associated SNR value. For scenario A, use Eq. 14 of Ref. (65) (Eq. 4.13 of this thesis). For scenario B, use Eq. 5.15 of this work.

5.8 Conclusions

In conclusion, we have shown that there exists a theoretical fundamental sensitivity limit due to the presence of $1/f$ noise in low signal optical detection. We derive the signal to noise ratio that corresponds to a simple thought experiment, designed to detect the presence of a small signal buried in detector noise. For white noise dominated signals, our results are similar to those in Ref. (65). However, they are quite different for the case in which $1/f$ noise dominates. This subtle point is particularly important and relevant to weak signal detection schemes, as the type of detection scheme involved can lead to different SNR characteristics. For the detection scenario discussed in this chapter, our results show that for a combination of white noise and $1/f$ noise the SNR is continually increased with increasing integration times for $\alpha < 1$. However, for $\alpha > 1$, the SNR peaks and begins to decrease with integration time. This result implies a fundamental limit on the sensitivity of detection systems that operate in the presence of $1/f$ noise ($\alpha > 1$). Depending on the strength of the small signal and the $1/f$ noise characteristics, the optimal SNR may not be sufficient to enable weak signal detection regardless of the integration time involved.

On an intuitive level, the results make good sense, as we can expect to observe strong $1/f$ noise contributions corresponding to low frequencies when collecting signals over relatively long time scales. The lower the frequency of a particular $1/f$ noise component, the wider the integration window needs to be to observe its net effect. The overall behavior of the SNR will degrade as a function of the integration time when the linear signal strength increase (with respect to the integration time) is unable to compensate for the increased noise associated with the stronger low $1/f$ noise frequency components for ($\alpha > 1$). Purely white noise dominated systems do not face this issue because the linear increase in signal strength is always more rapid than the increase in white noise.

Chapter 6. 1/f in FDOCT

This chapter is adapted from an as-of-yet unpublished manuscript: E.J. McDowell, M.V. Sarunic, and C. Yang, '1/f noise in spectrometer-based Fourier domain optical coherence tomography.'

6.1 Introduction

In recent years, we have seen rapid development of so-called Fourier domain detection systems in the research field of optical coherence tomography (OCT) (22–24). Significant efforts into characterizing the sensitivity of this technique have been made. However, one important area has remained understudied — the effect of 1/f noise on spectrometer-based FDOCT (sFDOCT) systems. 1/f noise manifests as fluctuations with power spectral density of the form $1/f^\alpha$, where α commonly ranges from 0.5 to 1.5. In this chapter, we present experimental findings that document the effect of 1/f noise on the detection sensitivity of such systems.

The presence of 1/f noise in optical detection can significantly degrade the effective precision and sensitivity. In interferometric detection methods, including time domain OCT (19), a common strategy for avoiding 1/f noise involves the use of heterodyne detection, in which the signal is frequency shifted into a band where 1/f noise is insignificant. Under these circumstances, we typically consider only white noise processes, including receiver noise, shot noise, and excess intensity noise (25). In previous analyses of FDOCT sensitivity, only these noise sources were considered to be

significant. However, sFDOCT systems employ homodyne detection and are thus susceptible to $1/f$ noise in the base band.

The signal to noise ratio (SNR) of a white noise limited OCT system is linearly proportional to the detection integration time (τ). This suggests that the SNR of the system can be increased to measure arbitrarily small signals by simply increasing τ . However, a large τ value leads to a significant contribution of $1/f$ noise, disrupting the linear SNR dependency on τ .

Chapters 4 and 5 established a generalized $1/f$ noise analysis protocol for simple detection scenarios (65, 92). Here, we will adapt the approach in (65) to accommodate for the nature of the sFDOCT signal (i.e., derived from multiple detectors) and determine the impact of $1/f$ noise on sFDOCT SNR.

The effect of multiple detectors on noise in a sFDOCT system deserves some elaboration. In the case of a homodyne interferometer (65), the noise analysis can be performed directly on the measured output of the interferometer. For a sFDOCT system, performing noise analysis on a particular spectrometer channel is not helpful, as we are primarily interested in the noise characteristics of the appropriately transformed depth (or spatial domain) scan. In the presence of $1/f$ noise, a direct relationship between the noise in a given spectrometer channel and the noise associated with the depth scan cannot be expressed without further information. Although it is reasonable to expect the signal from one detector channel to exhibit $1/f$ noise, it is not intuitively clear that when signals from multiple detector channels are combined in a Fourier transform summation that the resulting signal will have similar $1/f$ noise characteristics. We also note that $1/f$ noise between detector channels is correlated to some extent, which further complicates the

analysis. Fortunately, the black-box noise analysis approach in (65) allows us to perform the noise analysis directly on the depth scan, as long as we can experimentally establish that the noise in the derived depth scan is a combination of $1/f$ and white noise.

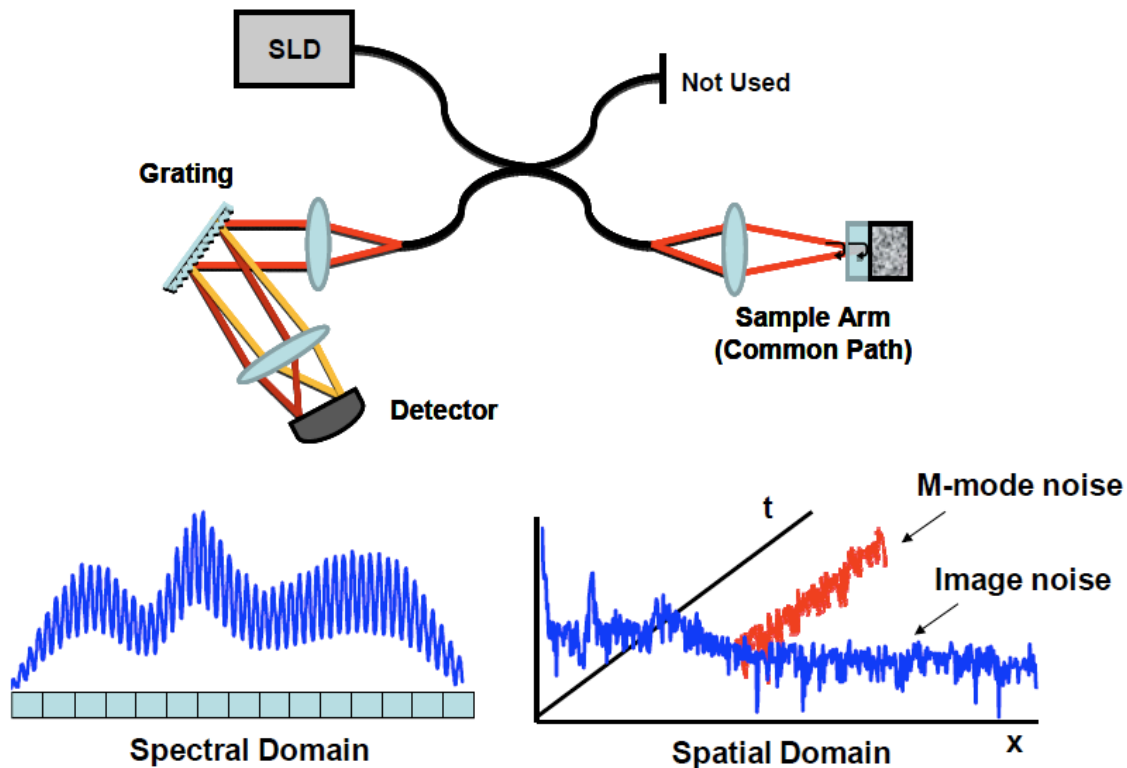


Figure 6.1. System schematic for the common path FDOCT system employed in this study. Noise acquired by individual spectrometer channels in the spectral domain is transformed into the spatial domain and can be measured as a function of time at a single point (M-scan) or across the depth scan.

6.2 $1/f$ Noise in M-mode Data

To determine the impact of $1/f$ noise on sFDOCT systems, we employed the common path interferometer depicted in Fig. 6.1. Light from a Superlum SLD (centered at 826 nm, 72 nm FWHM) passed through an 80/20 fiber coupler and was focused onto a sample. Light reflected from the surface of a coverslip above the sample interfered with light scattered from other depths in the sample and was spectrally dispersed onto a DALSA Spyder 3

linescan CCD camera. A phase stable common path interferometer was chosen to suppress additional noise terms due to interferometer drift.

In order to examine the background noise inherent in our sFDOCT system, we employed a single mirror as our sample. Thus, we detected only a reference beam and recorded a spectrum that was not modulated by signal fringes. Background data were collected using a 2 ms integration time for a total of 2000 seconds. The spectra were resampled linearly in wavenumber and Fourier transformed to produce depth scans representing the noise floor across the entire imaging depth. The noise power spectrum was measured from long time traces at individual depths in the A-scan as the Fourier transform of the autocorrelation function of the time trace. This processing requires the signal to be wide-sense stationary — a reasonable assumption as we do not expect the system performance to vary in time. Power spectra from multiple depths were then averaged to display the cumulative noise characteristics shown in Fig. 6.2. We find that even through

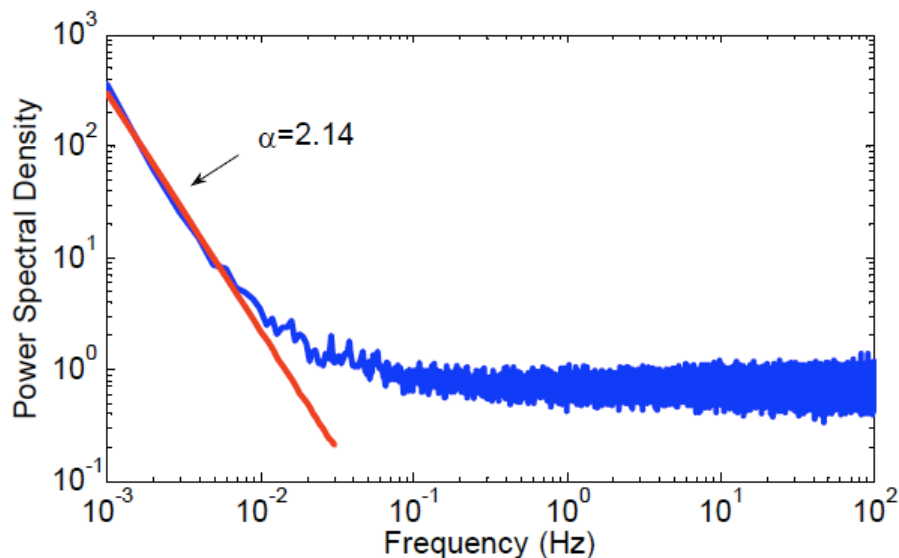


Figure 6.2. Power spectrum of the noise in the system. Values for the noise amplitude and exponent factor are found by fitting to this curve.

the sFDOCT computations, including resampling and Fourier transformation, 1/f noise continues to manifest at all depth locations. Two regimes can be distinctly observed in the power spectrum; above ~ 0.05 Hz the noise is white, while 1/f noise dominates for lower frequencies. The noise amplitude and the 1/f noise exponent factor can be extracted from Fig. 6.2. For this case, $\alpha=2.14$.

Employing the model described in (65), we used the power spectrum in Fig. 6.2 to predict the SNR of the FDOCT system. Specifically, the SNR behavior of this system was determined by the noise variance, which is given by:

$$\sigma^2(\tau, T) = \frac{A_{white}\tau}{2} + \int_{1/T}^{\infty} \frac{A_{1/f}}{2\pi^2 f^{\alpha+2}} [1 - \cos(2\pi f\tau)] df, \quad (6.1)$$

where A_{white} and $A_{1/f}$ are the white and 1/f noise amplitudes, and T is the total experimental time frame. We can also express the SNR:

$$SNR(\tau, T) = \frac{x_{signal}^2 \tau}{\frac{A_{white}}{2} + \frac{A_{1/f} \tau T^{\alpha-1}}{(\alpha-1)}}, \quad \alpha > 1, \quad \alpha \notin \mathbb{Z}^+, \quad (6.2)$$

where x_{signal} is the photon count rate associated with the signal of interest. The expression in Eq. 6.1 has been simplified according to (65).

Figure 6.3 (solid curve) shows the SNR trend predicted from the power spectrum, where we observed that the SNR increases linearly with τ (white noise dominant) before tapering to a constant value after times longer than ~ 1 second (1/f noise dominant). In fact, a deviation from linear behavior occurs as early as tenths of seconds.

To validate our SNR predictions, we processed the same background data set to experimentally determine the SNR dependency on τ . We generated the data we would expect from an experiment in which τ was physically tuned over several orders of

magnitude by summing sequential spectra. Following summation, each integrated spectrum was resampled and Fourier transformed to yield depth scans. The noise associated with each depth was then found by examining the fluctuations over the integrated spectra. The process was repeated for τ ranging from 2 ms to 40 s. These experimental noise values were then used (along with an arbitrary linearly increasing signal) to compute the experimental SNR. Figure 6.3 shows reasonable agreement between theoretical predictions and experimental results. The SNR cap shows that there is a limitation set by $1/f$ noise on the smallest signals that can be measured with our FDOCT system regardless of the measurement time involved. For scattering samples, this also implies that the penetration depth of a sFDOCT system is fundamentally limited as well.

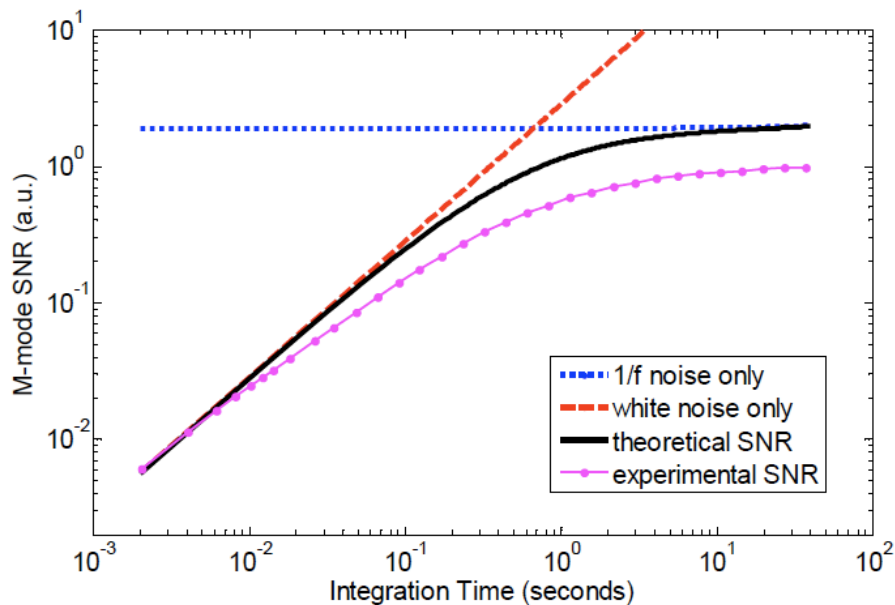


Figure 6.3. M-mode SNR as a function of integration time. The solid curve shows the theoretical SNR as determined from the noise power spectrum. Circular points represent experimental data averaged over multiple depths in the FDOCT depth scan.

The SNR measurement described in the paragraphs above relates the total signal to the time varying noise in the sFDOCT depth scan (i.e., noise in an M-mode scan). A more common way to define the SNR is to relate the signal to the noise across the depth scan. To distinguish the two definitions, we shall refer the first as M-mode SNR and the second as image SNR. The approach used to predict M-mode SNR is not applicable to image SNR. While these two SNR metrics measure the same quantity in the context of uncorrelated white noise, it is unclear how $1/f$ noise factors into the image SNR metric.

6.3 $1/f$ Noise in FDOCT Images

To demonstrate the existence of a $1/f$ noise imposed limitation in image SNR, as well as a corresponding limit in penetration depth, we constructed a tissue phantom composed of 1 μm latex beads embedded in polydimethylsiloxane (PDMS). The PDMS mixture was poured over a slanted opal diffuser, covered with a No. 2 coverslip, and allowed to cure overnight. A schematic of the phantom is shown in Fig. 6.4(a). M-mode data were taken at 10 μm increments over 2 mm in the direction denoted by the black arrow in Fig. 6.4(a). At each lateral location depth scans were acquired at a 2 ms integration time for 100 seconds. As before, spectra were summed in post-processing to display images corresponding to a range of τ values. The image SNR was determined as the square of the peak signal magnitude (at the opal diffuser) divided by the variance of the noise in a selected area below the diffuser removed from any signal peak.

For the scattering phantom, we expected to see the slope of the opal diffuser at increasing depths as τ is increased. A montage of images obtained from this sample at different τ values is shown in Fig. 6.4(a). For longer τ , an improvement in contrast can be

observed, and, as predicted, the depth penetration improved as well. However, in the regime where $1/f$ noise is dominant, the image quality no longer improves with increasing τ and the maximum imaging depth reaches a limit. An image SNR curve similar to that presented earlier for the M-mode SNR was obtained from these images and plotted in Fig. 6.4(b).

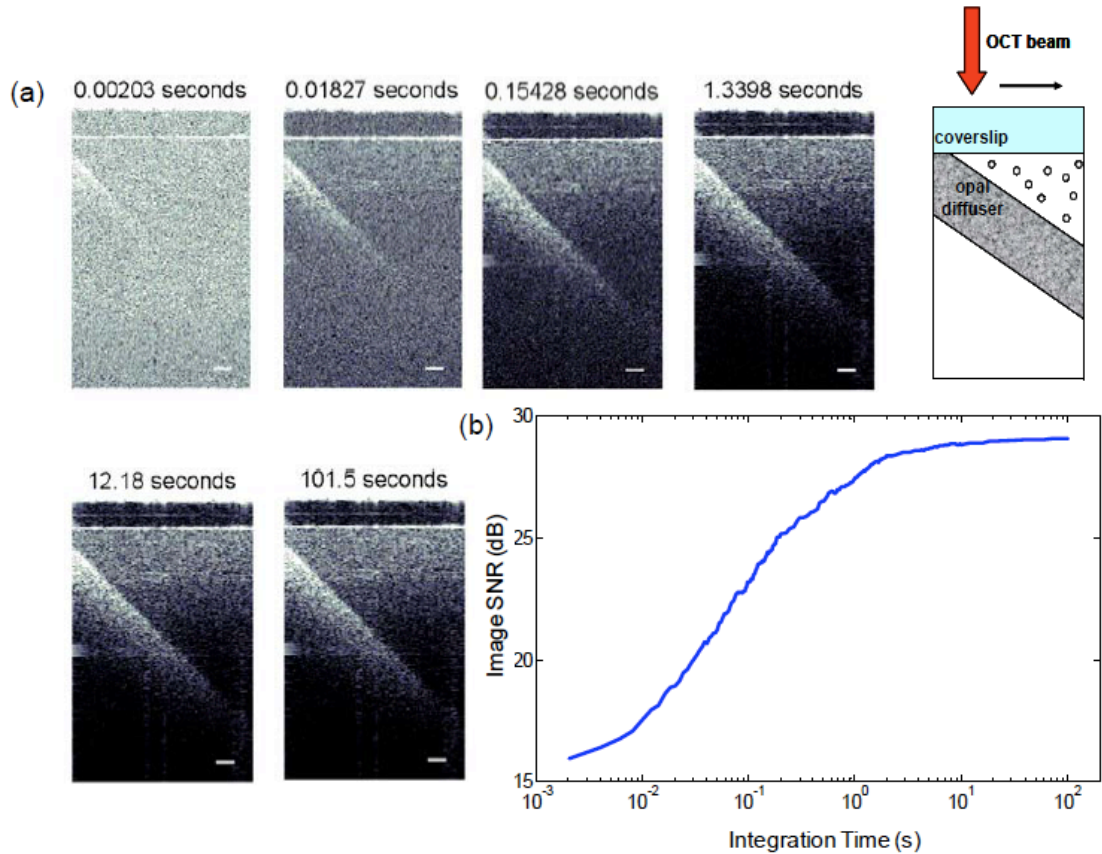


Figure 6.4. a) Image montage for increasing integration times. The scale bars are $200\ \mu\text{m}$. As the image SNR tapers to a constant value, the image quality becomes fixed. b) SNR curve extracted from the image sequence. The signal was measured at the opal diffuser and the noise was measured at a location below the diffuser removed from any signal.

Noise across the depth scan (image noise) represents uneven weighting of noise frequency components in the sFDOCT interferogram. The means by which this uneven weighting acquires a $1/f$ type dependence is unclear and deserves further study. Regardless,

we find that these two SNR definitions share a similar trend with respect to τ , implying that the dominant noise sources are likely similar in both cases.

We note that the noise across the depth scan, represented by the image SNR curve in Fig. 6.4(b), can easily be masked by other noise sources. If spectral calibration is not carefully conducted to remove the source spectrum, static variations across the source spectrum can create static noise patterns across the depth scan. We took care to remove this noise contribution by appropriately subtracting out these static variations.

Finally, we have found in previous work (Chapter 4) that $1/f$ characteristics, including the noise amplitude and exponent factor, are highly system dependent (65). This implies that sFDOCT systems should be characterized on an individual basis in order to determine the sensitivity limit associated with the particular system components.

6.4 Conclusions

In conclusion, we have shown evidence of SNR degradation caused by $1/f$ noise in sFDOCT systems. This SNR limit described above for both M-mode and image SNR metrics is a fundamental limitation of sFDOCT systems when operating in otherwise ideal conditions. The SNR of such systems increases linearly with integration time in white noise dominated regimes, and tapers to a constant as $1/f$ noise begins to dominate. This occurs for τ greater than ~ 1 second for SNR as defined by either time-varying noise (M-mode SNR), or noise across the depth scan (image SNR). This finding points to a fundamental sensitivity limit for low signal measurements that require long acquisition times.

Chapter 7. Turbidity Suppression Through Optical Phase Conjugation

At this point in the thesis, we switch gears to discuss a second, more novel, potential method for dealing with light scattering. As mentioned in Chapter 1, the remainder of this document will detail our attempts to time-reverse the process of light scattering. Here, we will describe the fundamental physics behind such attempts. This chapter is intended to provide background information for Chapters 8–10.

7.1 Optical Phase Conjugation

The concept of phase conjugation is quite old. Although the applications to biological tissues are new, it was shown over 40 years ago that optical phase conjugation (OPC) could reverse light scattering through a ground glass slide (98). Phase conjugation was also proven to be useful for removing aberrations associated with optical components for high-resolution imaging (99) and for the optimization of laser cavities (100, 101).

Before proceeding with a mathematical description of the holographic underpinnings, we will first discuss a conceptual view of phase conjugation. OPC is based on a device called a phase conjugate mirror (PCM). As compared to a conventional mirror, which is used to reverse the propagation direction of an incoming beam, a PCM reverses both the propagation direction and phase (Fig. 7.1). This causes an incoming beam to retrace its path back to the light source. If a distorting medium is placed between the light

source and the PCM, the phase conjugate beam will ‘un-distort’ itself on its path back to the light source. The novelty in our work on phase conjugation is that the technique has never before been used to remove the distortions caused by biological scatterers.

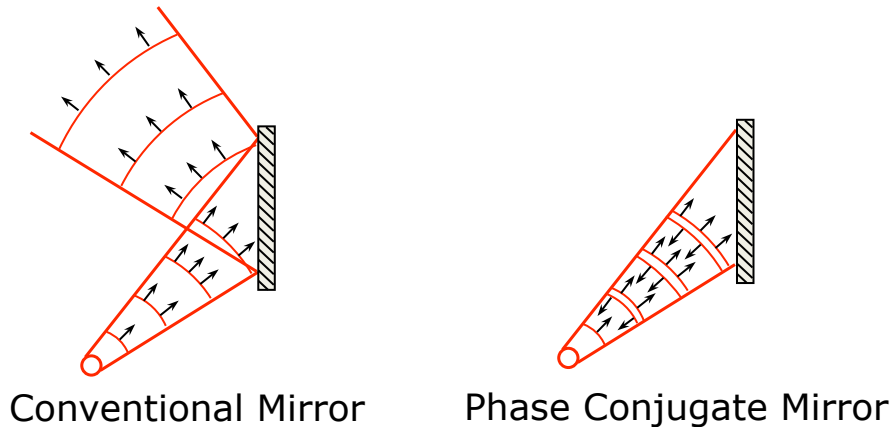


Figure 7.1. A conventional mirror compared to a phase conjugate mirror

7.1.1 OPC Based on Static Holography

We will first discuss OPC based on static holography, as employed in our experiments. In static holographic methods, a hologram is written into a holographic recording medium and read out at a later time.

The holographic recording medium used extensively in our work is Fe-doped lithium niobate (LiNbO_3), a photorefractive material. The Fe dopant creates defects in the material that trap charges (102). During the recording process a laser is passed through a scattering media, and the scattered wavefront interferes with a reference beam inside of the photorefractive crystal (Fig. 7.2). The interference pattern sets up an intensity grating within the crystal. The trapped charges become mobile in the presence of light, and positive charges migrate away from areas of high intensity. The intensity grating has now become a charge grating. The charge grating sets up a static electric field, which alters the

refractive index of the crystalline material through the linear electro-optic effect, otherwise known as the Pockels effect (103). In this manner, the interference pattern created between the scattered light and a reference beam is written as a refractive index pattern in the photorefractive crystal.

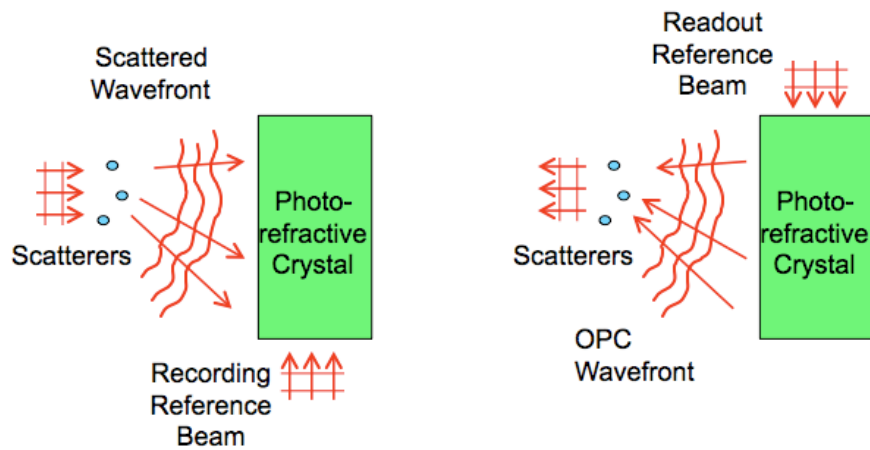


Figure 7.2. OPC through static holography

The refractive index pattern written into the crystal now acts like a diffraction grating. Playback with the same reference beam will recreate the scattered wavefront propagating in its initial direction, while a counter-propagating reference beam will phase conjugate the scattered field, essentially time-reversing the light scattering. The grating will remain in the photorefractive material until it is erased, either through high intensity uniform illumination or by heating the material.

A general description of holography may be helpful in understanding this process. Holography addresses the problem of recording both the amplitude and phase of an optical wave, in order to reconstruct that wavefront at a later time (104). The amplitude of a wave is easy to record using a photodetector, however a recording of phase is much more difficult. Typically this is accomplished by converting phase information to amplitude

information through interferometry, where a reference wavefront is added to the unknown sample wavefront. We can define the sample and reference waves as follows:

$$\begin{aligned} a(x,y) &= |a(x,y)| \exp[j\phi(x,y)] \\ A(x,y) &= |A(x,y)| \exp[j\psi(x,y)] \end{aligned} \quad (7.1)$$

where a is the sample wave and A represents the reference wave. When these waves interfere, the resulting intensity distribution is given by:

$$I(x,y) = |A(x,y)|^2 + |a(x,y)|^2 + 2|A(x,y)||a(x,y)| \cos[\psi(x,y) - \phi(x,y)]. \quad (7.2)$$

This form should be familiar from the discussion in Chapter 2. This pattern is then written into a recording media (in our case a photorefractive crystal as described above). Assuming the recording process is linear, the following amplitude transmittance pattern is written into the recording material (104):

$$t_A(x,y) = t_b + \beta' (|a|^2 + A^* a + A a^*). \quad (7.3)$$

We assume the intensity of the reference wave, $|A|^2$, is uniform, leading to a uniform bias transmittance, t_b . β' is the slope of the t_A vs. exposure curve of the recording material at the exposure time used in the experiment. The asterisk denotes the complex conjugate.

A coherent reconstruction wave then illuminates the pattern formed in the recording media. The light transmitted upon illumination is given by the product of the reconstruction wave, $B(x,y)$, with the transmittance function (104):

$$\begin{aligned} B(x,y)t_A(x,y) &= t_b B + \beta' a a^* B + \beta' A^* B a + \beta' A B a^* \\ &= U_1 + U_2 + U_3 + U_4 \end{aligned} \quad (7.4)$$

From Eq. 7.4 we can see that if the hologram is read out with the original reference beam ($B=A$), then the third term of the equation is an exact replica of the sample wavefront up to a multiplicative constant:

$$U_3(x,y) = \beta |A|^2 a(x,y). \quad (7.5)$$

Alternatively, if a conjugate reference beam is used ($B=A^*$) then the fourth term becomes proportional to the conjugate of the sample wavefront:

$$U_4(x,y) = \beta |A|^2 a^*(x,y). \quad (7.6)$$

Note that the useful portions of the reconstruction are accompanied by additional light field components. It was a major breakthrough by Leith and Upatnieks in 1962 (105) that brought about the usage of an off-axis reference beam to angularly separate the far field components in Eq. 7.4.

7.1.2 OPC Based on Dynamic Holography Through Degenerate Four-Wave Mixing

OPC can also be performed in real-time through dynamic holography, most commonly in a process called degenerate four-wave mixing (DFWM) (106-109). Dynamic holography means that two beams are instantaneously interacting to form a dynamic grating, which deflects a third light field in real-time.

Four-wave mixing is an important process in nonlinear optics, where three light fields interact to produce a fourth that is given by some linear combination (sum/difference) of the initial angular frequencies. The process requires a material with a nonzero third-order nonlinear optical susceptibility ($\chi^{(3)}$). The same LiNbO₃ photorefractive material described in the above section can be used to create this effect. OPC is dependent on degenerate FWM, meaning that all of the light fields are of the same wavelength. For 4 light fields ($j=1,2,3,4$) of the form:

$$E_j(x,t) = |E_j(x)| \exp[i(\omega_j t - kx)]. \quad (7.7)$$

Let E_1 and E_2 be pump beams that counter-propagate in a nonlinear medium. E_3 is the signal beam and E_4 is the beam that is generated through FWM. Without starting from scratch in nonlinear optics, phase matching requires that $\omega_4 = \omega_1 + \omega_2 - \omega_3$, and that $k_4 = k_1 + k_2 - k_3$. Since the pump beams counter-propagate ($k_1 = -k_2$), this means that the signal and generated beams will counter-propagate as well ($k_4 = -k_3$). It can further be shown that the electric field amplitude of the conjugate beam can be approximated by:

$$|E_4| = \frac{i\omega l}{2nc} \chi^{(3)} |E_1| |E_2| |E_3^*|, \quad (7.8)$$

in a medium of index n over an interaction length of l , where c is the speed of light. Thus the generated beam is proportional to the conjugate of the signal beam, $|E_3^*|$. One advantage of real-time OPC over static holography is the potential for amplification of the phase conjugate beam.

Additional methods exist, such as stimulated Brillouin scattering, to produce real-time phase conjugation. This, however, is beyond the scope of the current work.

7.2 Previous Work

The previous work from our group that has been conducted using OPC to time reverse scattering in tissues can be found in Yaqoob et al. (110). This work employed the static holography approach discussed above to take the first OPC measurements in tissues. The system described in the following chapters operates on the same principles, and will be described in detail in Chapter 8.

The most important result detailed in (110) is the proof-of-concept experiment shown in Fig. 7.3. A US Air Force target was used to apply an amplitude pattern to an incoming beam. If viewed through a transparent sample, such as agarose, as in Fig. 7.3(a),

the target pattern was clearly visible. However, if viewed through a piece of tissue (Fig. 7.3(b)), the information was scrambled and the image appeared cloudy. Figure 7.3(c) represents the static holographic recording of the scattered wavefront, which was played back through the sample in Fig. 7.3(d). Note that upon playback the target had been

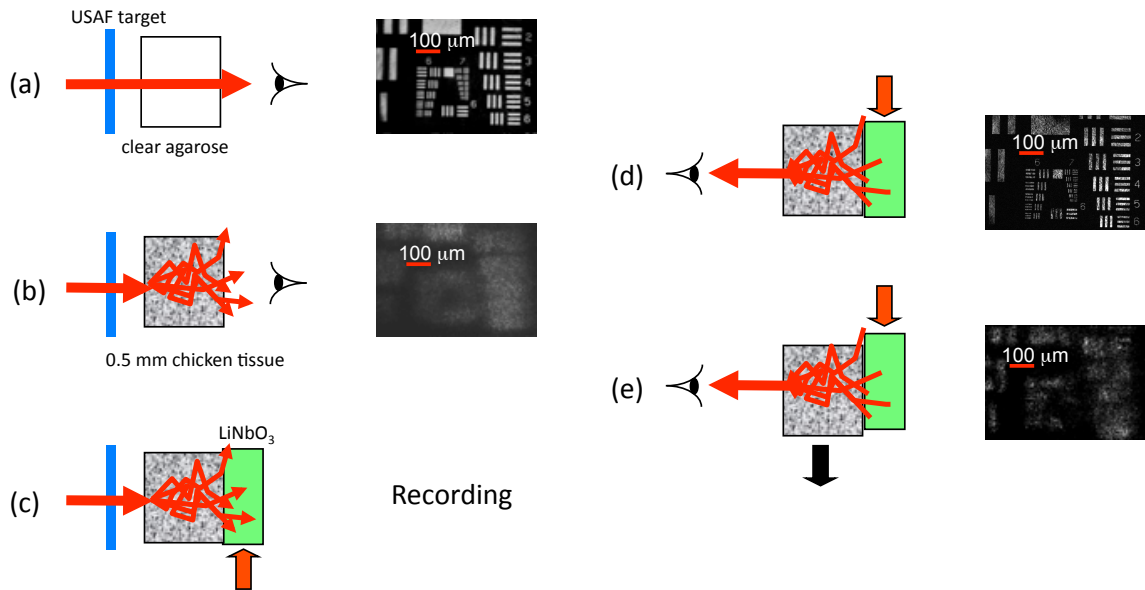


Figure 7.3. Proof-of-concept TSOPC experiment

physically removed from the system, but appeared in focus at the image plane of the system. Figure 7.3(e) conveys the sensitivity of the system to the position of the scattering media. We found it was essential for the scatterers to be in the same location during the playback process as they were during recording. When the scattering media was shifted, the signal began to decay quickly.

In addition to the above experiment, Ref. (110) demonstrated a signal through chicken breast tissues up to 0.67 mm in thickness. A interesting finding was also noted, which will be examined more thoroughly in Chapter 8, that the resolution of the

reconstructed image appeared to be constant regardless of the level of scattering. This initial paper laid the groundwork for the chapters to come.

Chapter 8. TSOPC System Characterization

This chapter is adapted from a recently submitted manuscript: E.J. McDowell, M. Cui, I.M. Vellekoop, V. Senekerimyan, Z. Yaqoob, and C. Yang, 'Turbidity suppression from the ballistic to the diffuse regime in biological tissues using optical phase conjugation,' Proceedings of the National Academy of Sciences, (Submitted, 2009).

8.1 Introduction

Elastic light scattering can significantly confound structural and functional information when biological samples are probed with light. Our recently published experimental technique utilizing optical phase conjugation (OPC) (110) has shown promise in dealing with the problem of light scattering. This method, termed turbidity suppression through optical phase conjugation (TSOPC), employs static holography to force a scattered light field to retrace its path through a highly scattering medium, effectively 'time reversing' the light scattering process. In this chapter, we will investigate both the fraction and shape of the light field reconstructed through a variety of samples, with scattering that spans both the ballistic and diffusive regimes.

Most of the previous studies of OPC in scattering media were conducted on sheets of textured plastic (111) or sheets of polyethylene or polypropylene (112). Our work employs both sections of chicken breast tissue of varying thickness and tissues phantoms of varying scattering coefficients in order to analyze the TSOPC process as the level of

scattering events is increased. We then fit these results to a theoretical model in which the contributions of ballistic and diffuse components are tracked. In doing so we uncovered several interesting facts. First, we will show that the TSOPC signal amplitude falls off at a slow rate compared to the ballistic (or unscattered) light component, which is inferred to be relatively insignificant in TSOPC signal generation. We also will also show that reconstruction of the incident wavefront can occur using only a very small fraction of the scattered light field (as little as 0.02%), provided the sample is highly scattering. Finally, we will discuss the non-intuitive finding that the quality of the reconstruction improves as the level of scattering increases, implying that, for the most highly scattering samples we examined, all information needed for reconstruction is included in the 0.02% of the light collected.

It is worth discussing where TSOPC falls in the context of standard optical methods that deal with the challenge of light scattering. Many techniques that acquire depth resolved information from tissues, such as optical coherence tomography (OCT) (19), selectively gate out and process only ‘information bearing’ ballistic or singly scattered components through coherent detection mechanisms. Alternatively, diffuse optical methods gather information from multiply scattered, or diffuse, photons exiting a biological material (16, 113). This leads to an increase in penetration depth, but a reduction in resolution (113). Techniques such as OCT exploit the wave nature of light, while diffuse optical methods model the photons as particles that diffuse through tissue. Our TSOPC technique falls at junction of these fields, attempting to extract coherent information from the bulk of the multiply scattered light. Here, we will show a TSOPC signal, dependent on coherent

detection and playback mechanisms, for light fields that have experienced over 200 scattering events.

Our specific methods involve two main steps: 1) collection and 2) ‘time reversal’ of scattered light components. Note that the phrase ‘time reversal’ is intended to help the reader envision the experiment. This process is not a true time reversal for two reasons. First, the collection area is of finite size, and the uncollected information is missing from playback. Second, even if the collection area was very large, collection in the far field means that the evanescent component of the scattered light field cannot be collected, and is missing as well. Current research efforts in which a shaped input beam is used to optimize transmission through a scattering medium (114, 115) are complementary to the second step of our process.

In this chapter we will 1) describe our TSOPC setup, 2) determine the TSOPC signal amplitude trend for an increasing average number of scattering events in both tissue and tissue phantoms with varying angular scattering properties, 3) examine the TSOPC resolution as the level of scattering increases, and 4) model and discuss the origin of the amplitude trend based on other measurable signals in our system.

8.2 Materials and Methods

The TSOPC system shown in Fig. 8.1 employed a 532 nm CW solid state laser in a Mach-Zehnder type interferometry scheme. Light scattered on transmission through the sample (20 mW incident power, 2 mm collimated beam) interfered with a reference beam (10 mW) as depicted in Fig. 8.1(a). This interference pattern was written into an iron-doped LiNbO₃ photorefractive crystal (PrC) over a time period of 20 seconds. A phase conjugate reference

beam (2 mW), approaching the PrC from the opposite direction, was used to playback the ‘time reversed’ wavefront as seen in Fig. 8.1(b). The phase conjugate wavefront retraced its path through the sample, reconstructing the incident light field. The reconstructed collimated beam was focused by a lens ($f=10$ cm), and the TSOPC signal was then measured at a CCD camera over a variable integration time (0.25 ms–1 s).

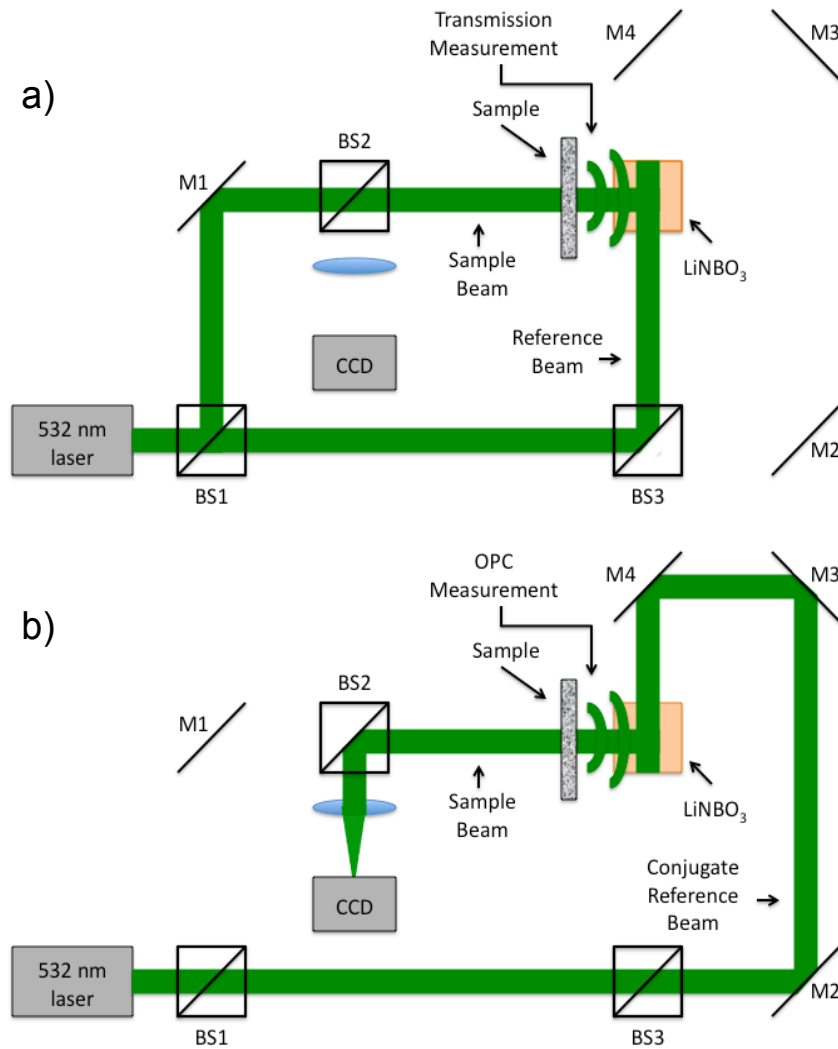


Figure 8.1. a) System setup for the recording process. Light scattered on transmission through a sample interfered with a reference beam in a photorefractive crystal (PrC) over tens of seconds. A transmission measurement was made at the location indicated. b) System setup for the playback process. A conjugate reference beam arrived at the PrC from the opposite direction and diffracted a conjugate beam toward the sample, retracing its path through the scattering material. The reconstructed beam was then focused to a spot and recorded at a CCD. A measurement of the phase conjugate power (OPC signal) was made at the location indicated.

Several measurements were made during this process: direct transmission through the sample over the collection area of the crystal (P_{Tmeas}); power exiting the photorefractive crystal before returning to the sample (P_{OPC}); and finally the TSOPC signal amplitude.

TSOPC measurements were made using two types of samples. The first corresponded to sections of chicken breast tissue ranging from 0.25 mm to 7 mm. The scattering coefficient was measured interferometrically using a standard Mach Zehnder interferometer. We also performed measurements on tissue phantoms composed of polystyrene microspheres embedded in polyacrylamide. The concentrations of microspheres were chosen to obtain scattering coefficients that varied between 0.1 and 15 mm^{-1} based on Mie theory calculations. The phantom samples were 3.5 mm in thickness. In addition to varying the scattering coefficient, the anisotropy factor was also varied by creating phantoms using 4 different sphere sizes (1003 nm, 433 nm, 157 nm, and 80.9 nm diameter) corresponding to anisotropy factors of $g=0.93$, 0.83, 0.28, and 0.07, respectively. The average sphere size was measured in a scanning electron microscope. The ballistic transmission through the phantoms was measured very far (~ 6 m) from the sample. Only those samples whose measured scattering coefficient matched the intended scattering coefficient to within 10% were used for measurements.

For the above measurements, a collimated sample beam was incident on the scattering sample. Such measurements were repeated for resolution studies in a slightly modified scheme in which the sample beam (10 mW) was focused onto the front face of the scattering sample (as shown later in Fig. 8.5) using a 6.24 mm focal length lens, and the scattered light pattern was written into the PrC upon interference with a reference beam (40 mW). In this manner, the reconstructed light field formed by a 1.5 mW conjugate reference

beam, formed a spot that was then imaged onto the CCD camera with a magnification of ~ 69 (given by the ratio of the focal lengths of the two lenses, where the lens in front of the CCD had a focal length of 43 cm). The PrC was placed 25 cm from the focused beam waist such that, in the absence of a scattering medium, the beam had diverged significantly (by a factor of ~ 4) upon reaching the reference beam (Fig. 8.5). The width of the measured spot, as determined through Gaussian fitting in two orthogonal directions, was then used to investigate the resolution of the TSOPC system.

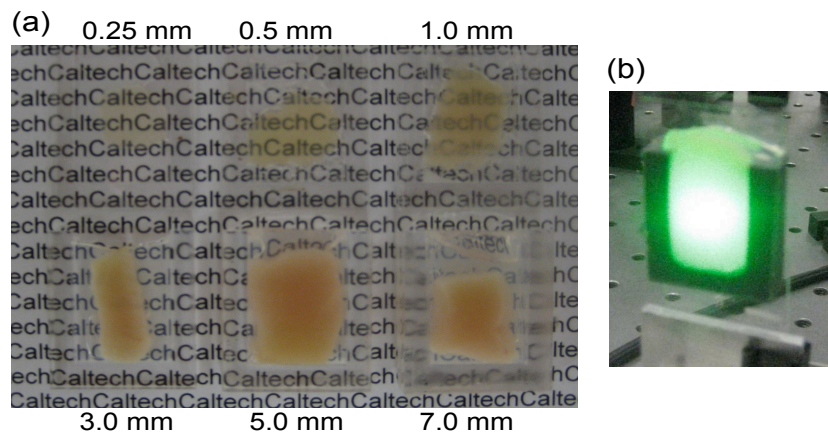


Figure 8.2. a) Representative 0.25, 0.5, 1, 3, 5, and 7 mm thick chicken breast sections placed above text. As the thickness increases, light scattering makes it impossible to read the text below. b) A 3.5 mm diameter beam of 532 nm light scattering through a representative 7 mm section of chicken breast tissue. For reference, the black plastic spacer is 30 mm x 24 mm.

8.3 Results

8.3.1 Chicken Breast Tissue Experiments

We will first examine results from chicken tissue samples of varying thickness. Figure 8.2(a) shows representative samples indicating that the thickest tissue samples used in this study were by no means transparent. Figure 8.2(b) shows the large extent of light scattering experienced by a green incident beam ($\lambda=532$ nm).

We determined the scattering coefficient of the chicken breast tissue to be $\mu_s=30.3$ mm^{-1} . The following data will be reported as a function of the average number of scattering events experienced by a photon tracing an approximately straight path through the sample, quantified by $\mu_s L$ (L is the sample thickness). Although most photons take longer paths through the scattering material, scattering more than $\mu_s L$ times, this is a simple reference quantity for turbidity estimation. In general the ballistic, or unscattered, component of the transmission decays exponentially with depth into a scattering medium, $T_{ball} = \exp(-\mu_s L)$. All data are normalized with respect to a non-scattering sample.

The total signal contained in the reconstructed focused spot, as measured on the CCD in Fig. 8.1(b), was indicative of the amount of light that had returned to its original configuration. For simplicity, this metric can be replaced by the amplitude, or peak intensity, of the focused spot, shown explicitly in Fig. 8.3(b) and 8.3(c). This is possible because the full-width at half-maximum (FWHM) of the reconstructed spot did not change as a function of scattering strength (a phenomenon that will be discussed in detail later in the chapter). The red curve in Figure 8.3(a) displays the TSOPC amplitude as a function of $\mu_s L$. Error bars correspond to the standard error from measurements made over different sample locations (i.e., different random configurations of scatterers). Although the TSOPC amplitude initially dropped off quickly, the slope began to taper off more slowly as $\mu_s L$ increased. This limited decrease is particularly noteworthy when compared to the dramatic decay of the ballistic component (blue curve, Fig. 8.3(a)).

The signals in Fig. 8.3(a) were measured in tissue sections that ranged from 0.25 to 7 mm in thickness, the thickest of which corresponding to a ‘time reversal’ of more than 200 scattering events. This is by no means trivial. Transmission through the 7 mm tissue

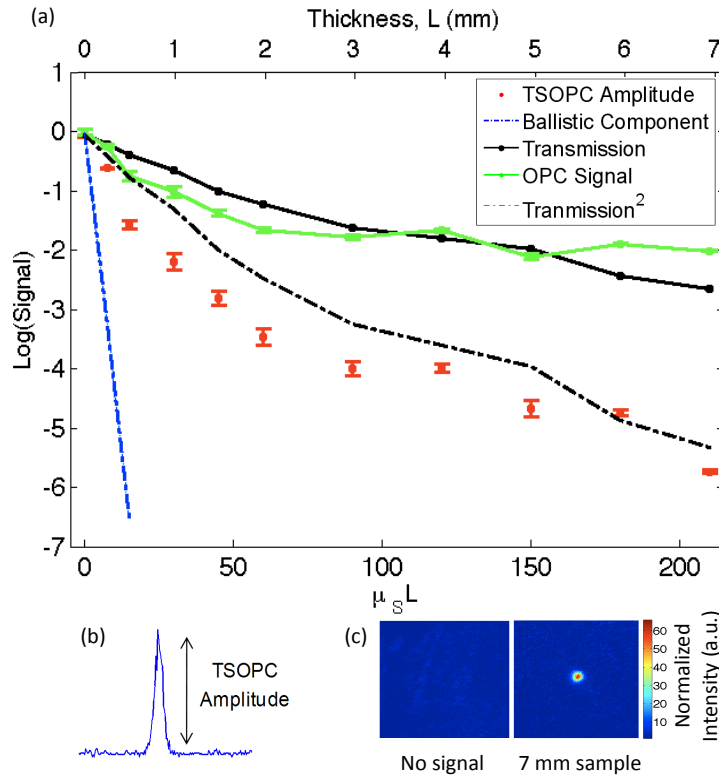


Figure 8.3. a) The TSOPC amplitude (red data), ballistic transmission (blue line), total transmission (black curve), and OPC signal (green curve) as levels of scattering were increased. The square of the transmission (dashed curve) approximated the TSOPC amplitude in trend. Error bars represent the standard error over N ranging from 3–7 measurements. b) The TSOPC amplitude was measured as the height of the focused spot after the background signal was subtracted. c) The signal from the 7 mm chicken breast sample was clearly visible above the noise in the system.

sample would result in a ballistic component at -91 on the scale shown in Fig. 8.3(a), or an attenuation of -910 dB.

The solid black curve in Fig. 8.3(a) represents the direct transmission through the chicken breast samples measured over the collection area of the PrC, T_{meas} (recorded at the location denoted in Fig. 8.1(a)). The green curve shows a similar trend and represents the power that exited the PrC upon playback, denoted P_{OPC} and recorded where indicated in Fig 8.1(b). The dependence of the TSOPC amplitude on these measured signals will be discussed and modeled in the Discussion section.

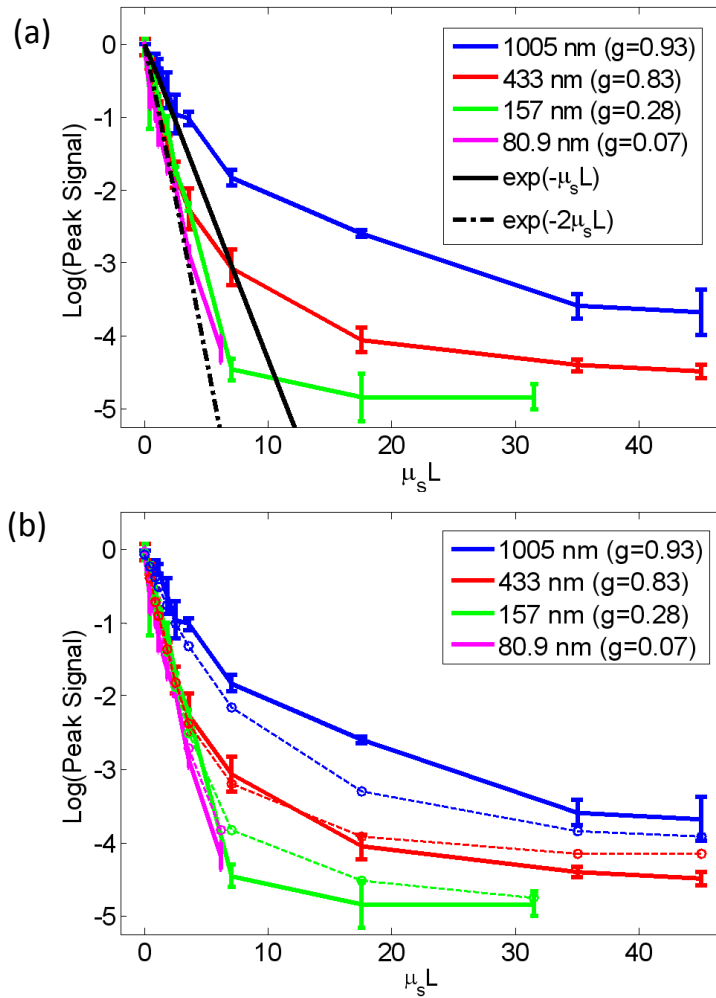


Figure 8.4. a) TSOPC amplitude trend for tissue phantoms composed of polyacrylamide ($n=1.346$) with embedded polystyrene microspheres ($n=1.6$). a) The amplitude signals fell off more dramatically for smaller spheres with a lower anisotropy factor. The black curve represents the ballistic transmission through the samples, and the dashed curve represents the ballistic transmission through a sample twice as thick. b) The TSOPC amplitude curves were compared to the square of the transmission and show that they agree in trend for the various sphere sizes.

8.3.2 Tissue Phantom Experiments

In order to examine the dependence of our system on the angular scattering properties of the sample, we conducted experiments on tissue phantoms composed of polystyrene spheres embedded in polyacrylamide. By varying the size of the spheres, the anisotropy factor, g , of the scattering media can be altered. A measure of the angular spread of the

scattered light, g is defined as the average cosine of the scattering angle ($g = \langle \cos(\theta) \rangle$). Figure 8.4(a) shows the TSOPC amplitude as a function of $\mu_s L$ for four types of phantoms from highly forward scattering ($g=0.93$) to nearly isotropic ($g=0.07$). We found that the more forward scattering samples resulted in a larger TSOPC signal for the same $\mu_s L$. The solid line superimposed on the data in Fig. 8.4(a) shows the decay of the ballistic component of the transmission, while the dashed line shows the decay of the ballistic component through a sample twice as thick ($2L$). Except for the case of the highly forward scattering samples, the TSOPC amplitude initially decayed along the dashed line.

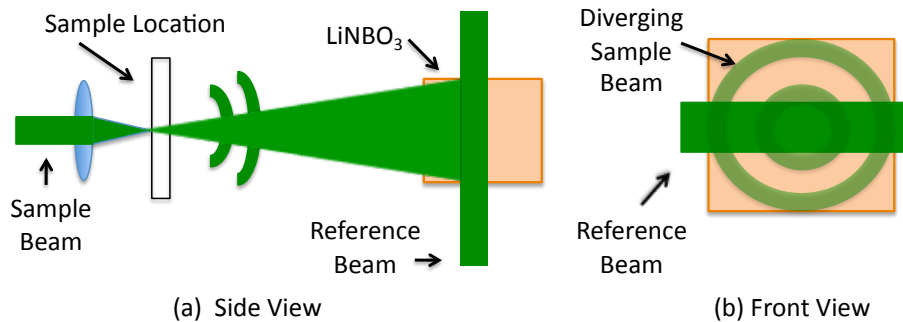


Figure 8.5. a) With no sample present, the light diverging from a focused beam expands on its path to the photorefractive crystal. Using a reference beam of fixed width, angular components of the diverging beam are better captured along one axis. a) side view. b) front view

8.3.3 Resolution Trends

To study the resolution of our TSOPC experiment, we employed a modified system in which the sample beam was focused onto the front face of the sample (Fig. 8.5(a)). The remainder of the system is as described in Fig. 8.1, and phase conjugation was used to reconstruct this spot at the front face of the sample. An imaging system formed between the lens shown in Fig. 8.5(a) and that in front of the CCD in Fig. 8.1(b) was used to relay and

magnify the reconstructed spot onto the camera for detection. The spot sizes described in the following results refer to the spot size at the sample.

We found that with no scattering sample present, the measured spot was narrow in the horizontal dimension, but spread over a large range vertically (top left panel of Fig. 8.6(a)). However, this effect could be mitigated through the presence of strong scattering in the sample. Figure 8.6(b) shows the full-width at half-maximum (FWHM) of the reconstructed spot in both X and Y directions for increasing thicknesses of chicken breast samples. Both values tapered to tight ($1.5 \mu\text{m}$), nearly diffraction limited (calculated to be

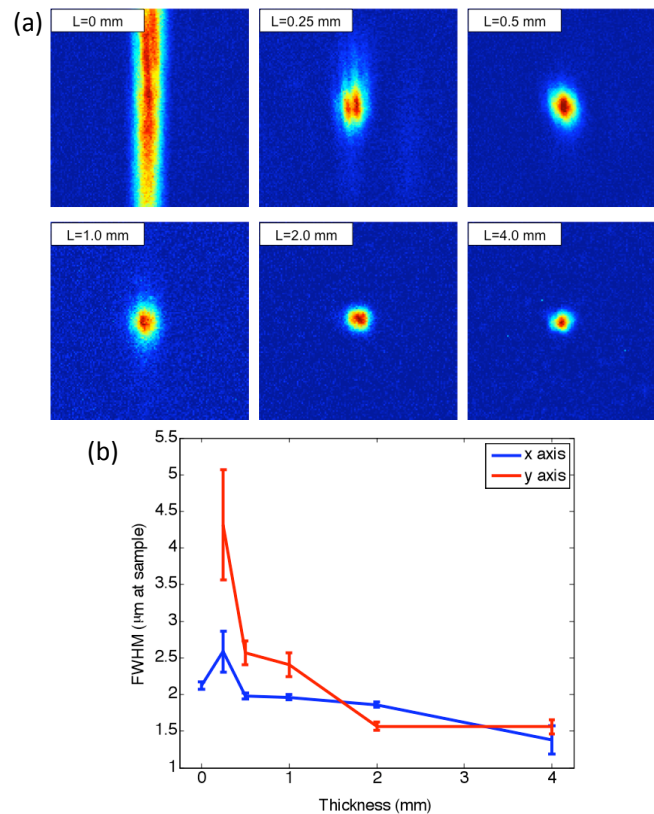


Figure 8.6. Resolution data for chicken samples. a) The top left panel shows that with no sample present the reconstructed signal forms a stripe rather than a spot. The other panels show that as the scattering is increased, the stripe is reduced to a near diffraction limited spot. b) The reduction in the size of the focused spot in the x and y directions. The diffraction limited in this setup was calculated to be $1.2 \mu\text{m}$. Error bars represent the standard error of the full-width at half-maximum (FWHM) made over $N=3$ measurements.

1.2 μm) spots, although the FWHM in the X direction tapered more quickly. The same trend can be seen with tissue phantoms in Fig. 8.7.

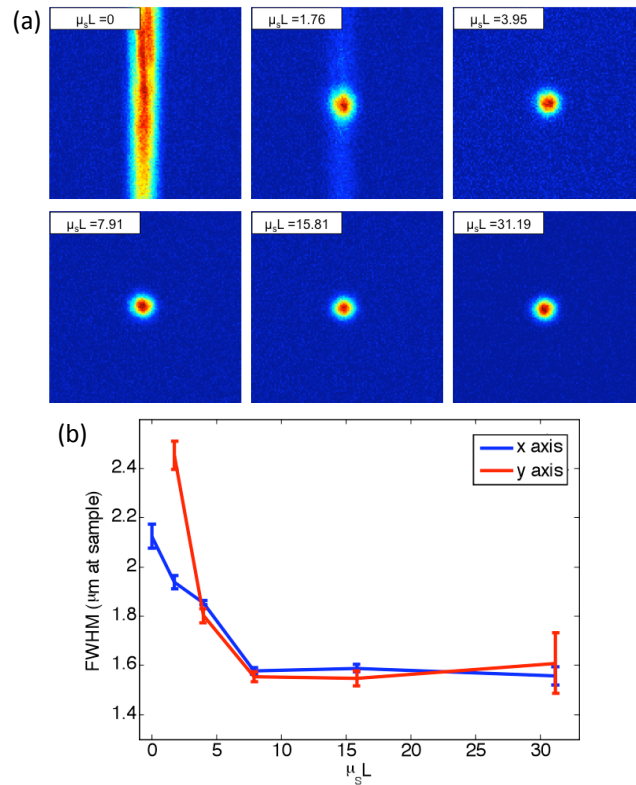


Figure 8.7. Resolution data for tissue phantoms. a) The top left panel shows that with no sample present the reconstructed signal forms a stripe rather than a spot. The other panels show that as the scattering is increased, the stripe is reduced to a near diffraction limited spot. b) The reduction in the size of the focused spot in the x and y directions. The diffraction limited in this setup was calculated to be 1.2 μm . Error bars represent the standard error of the full-width at half-maximum (FWHM) made over N=3 measurements.

8.4 Discussion

8.4.1 Amplitude Trends in Tissue Samples

To understand the TSOPC amplitude trend, we observed the corresponding trends for other measurable quantities in the system, including the transmission and OPC signals plotted in Fig. 8.3(a). As the thickness of the chicken sections were increased, both the transmission and OPC signal decayed in a similar manner. If we liken our holographic process to a four-wave-mixing scheme in terms of power dependence, the power exiting the crystal, P_{OPC} ,

should be proportional to the product of the power in the sample, recording, and readout beams: $P_{OPC} \propto P_{sample}P_{recording}P_{readout}$. Thus, for fixed power in the recording and readout beams, we expect the OPC signal to follow the transmission. Although we indeed saw the transmission and OPC signals fall off in a similar manner, we saw a large discrepancy between these and the TSOPC amplitude (red curve). The origins of this trend will be discussed and modeled later in this section.

The signal we measure through the thickest chicken tissue sample is worth additional discussion. One might expect that efficient ‘time reversal’ would be dependent on the collection of the entire scattered wavefront. However, a measurement of the total transmission through a 7 mm chicken breast sample over the collection area of the PrC shows that only ~0.02% of the power incident on the sample is scattered into the collection region. This implies that at most 0.02% of the incident power is used to record the hologram for phase conjugation, and is important because it shows that the TSOPC process is capable of ‘time reversal’ even when only a small portion of the scattered wavefront is captured. The 7 mm thickness of chicken breast tissue does not represent a hard limitation on the capabilities of our system. It was simply the thickest sample that we measured in this study.

To cast our results in a slightly different light, consider an OCT system centered at 532 nm with 120 dB of SNR. If we tried to image these chicken samples with such a system, we would find that our depth penetration is limited by scattering to ~0.5 mm, or $\mu_s L \sim 15$. Although we are not imaging, our measured TSOPC signal through 7 mm of highly scattering tissues is noteworthy in the context of current biomedical imaging standards.

8.4.2 Amplitude Trends in Tissue Phantoms

The amplitude signals recorded using tissues phantoms were shown to depend on the g factor of the sample. This is due to the limited collection angle of the PrC. Forward scattering events were more likely to direct a photon towards the PrC, while isotropic scattering events were likely to direct a photon away from it. Thus, the final measured signal for isotropically scattering samples was less than that for forward scattering samples.

It is interesting that the measured signals in Fig. 8.4(a) fall off along the dashed line, corresponding to the ballistic component of light transmitted through a sample of double thickness. A measured TSOPC amplitude close to the dashed line implies no advantage is gained by performing the TSOPC experiment. However, as $\mu_s L$ increased, the TSOPC amplitude began to diverge from the dashed line, meaning that we started to see an increased signal through TSOPC. The ballistic component of the scattered light was initially much stronger than the TSOPC signal, which became visible only after the ballistic component decayed significantly. In sum, Fig. 8.4(a) shows that we can efficiently collect forward scattered light, and implies that the majority of the signal we measure in tissues is related to forward directed scattering events as opposed to isotropically directed scattering events.

8.4.3 Origins of Amplitude Trends

A simple predictor of the TSOPC amplitude is square of T_{meas} , shown as a dashed black curve in Fig. 8.3(a) and dashed curves in Fig. 8.4(b). This finding is in agreement with literature results in which phase conjugation was studied (112, 116). Gu and Yeh (116)

invoked the reciprocity theorem and conservation of energy to show that under ideal circumstances (specifically in the absence of absorption and backscattering), the fidelity of the process, equivalent to our amplitude measure, scales as the square of the fraction of light intercepted by the phase conjugating device. This was experimentally verified using scattering sheets of polypropylene and polyethylene (112). Our samples are by no means ideal, most notably in terms of non-negligible absorption and backscattering of the tissue samples. The agreement of our TSOPC amplitude (red curve) with the square of the transmission (dashed black curve), at least in terms of trend, confirms that these predictions hold true for the case of tissue scattering as well. Our results serve to validate this theoretical prediction for a broader range of applications.

This finding deserves some additional discussion. We can describe the total ‘time reversed’ transmission as the product of the power leaving the PrC and the transmission of the phase conjugated beam: $P_{TSOPC} = T_{OPC} P_{OPC}$. One may argue that if each photon trajectory is perfectly phase conjugated and efficiently ‘time reversed’, T_{OPC} would trend towards a value of 1, and all power directed into the sample would be effectively transmitted. The flaw in this argument is that fundamentally, our experiment cannot be described by a photon picture. If we think of the sample as a black box, and monitor only the fraction of the input light that exits one side of the box, we can make an interesting comparison. If the box contains a 50/50 beamsplitter, we would expect 50% of the input power to exit. If we phase conjugated the exiting light, we would expect a second decrease of 50% on the way back. Although this may appear to be a very different scenario, in reality it is quite similar. In our TSOPC experiment, we can think of dividing the scattered wave into groups that have passed through channels with a particular transmission

coefficient (as in (115)). The bulk of the incident light is diffusely reflected, so the majority of the channels possess very small transmission coefficients. However, a small set of these channels transmits light in fairly efficient manner. Each of these channels can be likened to a beamsplitter with a fixed transmission coefficient. When the light is phase conjugated back along these paths, they again transmit the same fraction of light. Thus, in reality, the T_{OPC} is equivalent to the transmission of an incident plane wave through the sample.

In our current setup, where P_{OPC} scales with T_{meas} , the above argument confirms the T_{meas}^2 dependence predicted by Gu and Yeh. The amplitude of the transmitted light is the same as that expected by a double pass through the sample. The advantage, however, is that instead of the diffuse transmission that would result if a conventional mirror was used to reflect light back through the sample, we see the phase conjugate beam regain spatial coherence to reconstruct the incident light field. If a digital version of this experiment was employed, by recording the interference of the scattered field with a reference beam on a camera and playing back the phase conjugate field with a spatial light modulator, then P_{OPC} could be increased arbitrarily and enhanced transmission may be possible.

Although the T_{meas}^2 curves agree with our data in trend, they do not provide a very close fit, especially for the tissue phantom results. Although the properties of the sample are accounted for, the properties of the phase conjugation are not. In Appendix D2, we formulate a model that includes both T_{meas} and P_{OPC} values to describe the crossover from ballistic to diffusive regimes. The result is as follows:

$$\frac{P_{TSOPC}}{P_{Norm}} = \left[T_{ballistic} + X \sqrt{\left(\frac{P_{OPC}}{P_{Norm}} - T_{ballistic} \right) (T_{measured} - T_{ballistic})} \right]^2, \quad (8.1)$$

where P_{Norm} is the measured OPC power with no sample present. If we make the assumption that the aperture of the PrC is sharp, X^2 represents the ratio of the active area/responsivity of the PrC to the active area/repsonsivity of the photodetector used to measure the transmission. This assumption is not valid in reality since the aperture of the PrC is determined by the size of the Gaussian reference beam, but the trend of the X^2 values is still illuminating.

Figure 8.8 shows fits of this model to both the tissue (Fig. 8.8(a)) and phantom data (Fig. 8.8(b)). The fits are significantly better than the T_{meas}^2 fits for all types of samples since information about both the sample and the phase conjugation are taken into account. If we examine the X^2 values from fits to the phantom data (Fig. 8.8(a)) we see that X^2 decreases with the anisotropy factor, g . This is attributable to the fact that the responsivity of the PrC is diminished when scatterered light enters the active area at increasing angles with respect to the incident beam. This serves to reduce the amplitude of the interference pattern written into the PrC, and results in the same outcome as the case of a PrC with optimal responsivity that shrinks in size as the g factor decreases. Since tissues are highly forward scattering, we might expect that a fit to the chicken tissues sections would result in a similar X^2 as the 1 μm beads. However, we found a much smaller X^2 value. We expect that this occurred because the chicken sections are non-ideal scattering samples. The speckle pattern formed by the scattered light is not stationary due to diffusion of particles within the tissues. This implies that the particular channels that existed throughout the recording process do not necessarily exist or possess the same transmission coefficient upon playback. Thus, even if a strong pattern is formed at the PrC, it may not exactly correspond to the scattering structure of the tissue upon playback. A faster holographic

medium or a digital implementation of this experiment may diminish this effect in the future.

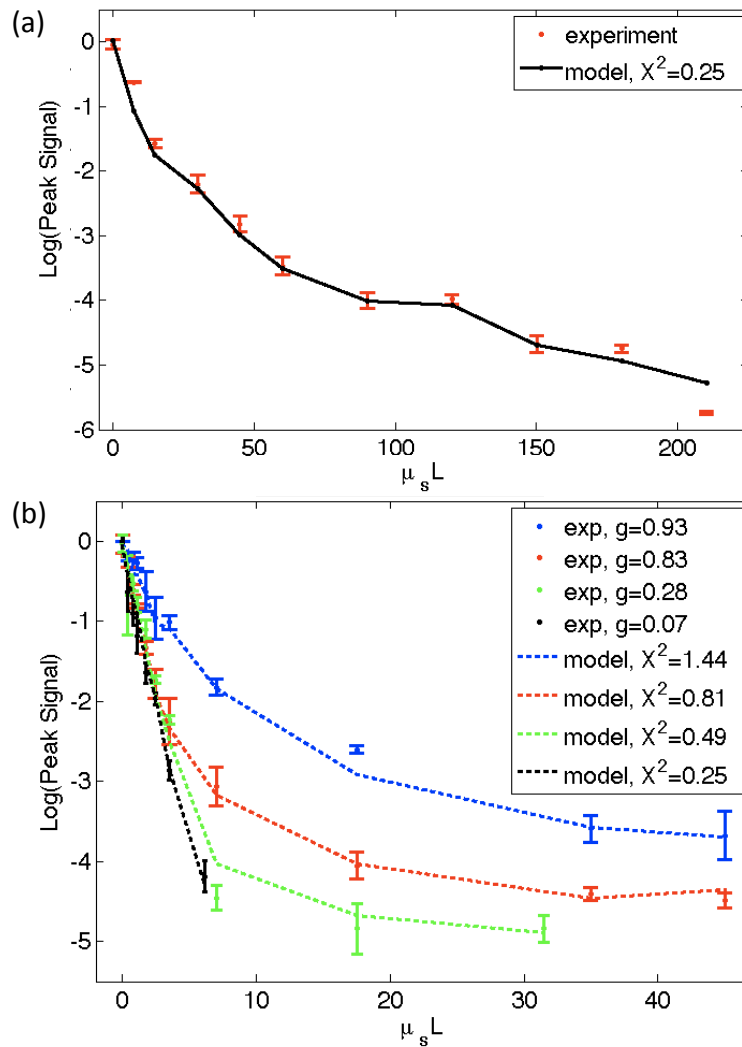


Figure 8.8. Model fits to the experimental chicken tissue results (a) and the experimental tissues phantom results (b). A model that includes information about both the sample and the phase conjugation performs significantly better than the T^2 predictor in both cases.

8.4.4 Resolution Trends

One might expect that the resolution of the TSOPC system would degrade as scattering becomes more prominent. However, we found that scattering can be beneficial in terms of resolution when a limited collection angle is employed. This experiment represented a low

collection efficiency situation because the PrC was placed far from the sample plane. With no scattering sample in place, Fig. 8.5(a) shows that the sample beam had diverged significantly upon reaching the PrC, and only portions of the sample beam that overlapped with the reference beam were recorded. From a Fourier optics perspective, the large angle components of the diverging beam carried information about high spatial frequencies at the focus. Thus, by losing these components we could no longer expect to reconstruct a diffraction-limited spot. As the sample and reference beams were orthogonally oriented in the crystal (Fig. 8.5(b)), the effective recording area for the sample beam had a width of 3.5 mm (FWHM of the collimated reference beam) and length of 10.0 mm (length of the crystal). This explains the shape of the spots shown in Fig. 8.6(a) and 8.7(a). Since the collection region was oblong, diverging angular components were better captured along one axis, leading to a smaller reconstructed spot along that dimension. As the samples became more highly scattering, more of the angular components were directed into the PrC, and the spot size was improved. The tapering of the FWHM to a constant value implies that beyond a scattering threshold the angular components incident on the sample were effectively randomized such that efficient collection could be obtained over any small portion of the scattered wavefront. This finding has been demonstrated previously for plastic sheet aberrators and etched glass phase screens (111), confirming theory and simulations on thin, random phase screen aberrators (117, 118), but has never been demonstrated in extended scattering samples or biological materials. Our work serves to extend these findings into the realm of realistic biological materials.

We mentioned previously in discussing our amplitude results that the peak of the detected signal was a useful metric only if the width of the spot remained constant. There

were two significant differences in system geometry between the amplitude experiments and the resolution experiments described immediately above. First, the sample beam was collimated as opposed to focused on the sample. This reduced the beam divergence towards the crystal. Second, the PrC was placed as close as possible to the sample plane. Both of these geometrical factors allowed for efficient collection regardless of the level of scattering. Thus, for the amplitude experiments described above, the FWHM of the measured spot was fixed for all measurements. Our amplitude studies showed that we could reconstruct a signal with only a small portion of the scattered wavefront, and our resolution studies provided us with evidence to claim that all relevant information was contained in this reconstruction.

8.4.5 Significance and Future Work

It should be pointed out that our results, in both tissues and tissue phantoms, contrast the common misconception that light loses its coherence upon scattering. While a tight pulse of light spreads as scattering occurs and spatial coherence is certainly lost, individual portions of the wavefront traveling on various trajectories through the scattering media retain relative coherence and thus are still capable of interference. We have shown a signal, dependent on coherent recording and playback mechanisms, for light that has scattered over 200 times on average. However, polarization shifts can accrue during scattering and, in the case where the scattered light is sufficiently diffuse, the light field no longer possesses a preferred polarization state. As light of an orthogonal polarization cannot interfere with the reference beam, we can expect to record only half of the available information in this situation. We believe that future technological developments of TSOPC

systems should include the capability for recording the scattered wavefront using two orthogonal polarizations, demonstrated to be useful in a related system in Ref(115).

8.5 Conclusions

In conclusion, we have demonstrated that we can efficiently suppress elastic light scattering in tissues and tissue phantoms using optical phase conjugation. We examined the decay of the reconstructed TSOPC amplitude as a function of $\mu_s L$ and found that, after an initial sharp drop, the signal decreased slowly compared to the decrease in ballistic transmission. This amplitude trend roughly scaled as the square of the transmission through the samples, and was modeled more accurately using measurements that included both sample and phase conjugation effects. TSOPC signals were measured through up to 7 mm of chicken breast tissue, displaying effective reconstruction through coherent mechanisms after an average of over 200 scattering events. Additionally, we showed that as little of 0.02% of the scattered wavefront was sufficient for a TSOPC reconstruction. Measurements on tissue phantoms confirmed the amplitude trends, and showed that more highly forward scattering samples lead to larger TSOPC amplitude values as more scattered components were directed into the collection region of the PrC. Finally, increased scattering in both tissues and tissue phantoms was found to improve the resolution of the detected signals by improving the overall angular collection efficiency of the system.

Chapter 9. TSOPC in Living Tissues

Over the past two years, we have attempted several studies of TSOPC in living tissues. There are several mechanism that make TSOPC measurements more difficult in living tissues, including various sources of sample motion and absorption due to the presence of blood flow. Our initial experiments were designed to separate these two effects, questioning whether the combination would prove insurmountable for the current implementation of our system. The first experiment involved measurements on freshly excised portions of lobster tissues. The idea being that the tissue was still alive and functioning, although the blood flow was cut off. A second set of experiments involved *in vitro* tissue cultures, thin layers of epithelial tissues grown in petri dishes and nourished purely by diffusion; again, difficulties with blood flow would be avoided. Unfortunately, unexpected sources of error crept into both of these experiments. The slick lobsters tissues slipped within coverglasses during the experiments. As such, dead tissues appeared to be just as ‘alive’ as living tissues. The tissue cultures required a horizontally-mounted sample stand, which made the tissues more susceptible to air currents in the room, causing vibrations that masked active motion in the samples. These failures prompted us to move ahead with experiments on living tissue in the presence of blood flow. The remainder of this chapter is adapted from a manuscript in preparation by M. Cui, E. J. McDowell, and C. Yang entitled ‘An *in vivo* study of turbidity suppression by optical phase conjugation (TSOPC) on rabbit ear’.

9.1 Introduction

Biological tissues are highly heterogeneous. Optical wave propagation in such media is dominated by elastic scattering (1), which presents significant challenges for tissue optics. Elastic scattering can randomize the optical wavefront, preventing direct imaging through tissues. The multiple scattering events cause strong backscattering, limiting optical measurement to superficial depths. The elastic scattering of an optical wave is nevertheless deterministic and time reversible. Optical phase conjugation (OPC) is known to be able to time reverse the scattering process and ‘heal’ the wavefront distortion. Despite the fact that OPC has been an active field since the 1970s (119–123), its application to tissue optics remains largely unexplored. Recently, we demonstrated that holographic recording of the transmission of a single mode laser through chicken tissue, followed by a phase conjugate playback, can allow the optical wave to retrace its scattering path (110). We found that this process termed turbidity suppression through optical phase conjugation (TSOPC) is surprisingly robust. To date we have been able to perform TSOPC through 7 mm thick dead chicken tissue sections. While such a technique holds great promise in tissue optics, living tissues pose additional challenges.

These challenges can be divided into two main categories: sample motion and sample absorption. Our technique is a two-step process, holographic recording of the scattered wavefront followed by playback. The applicability of our technique for *in vivo* work depends on the relative time scales between the optical realization of TSOPC and tissue variations that can perturb the time reversal process. Motion of the scatterers during and after the recording time serves to reduce the portion of the optical wave that is efficiently time reversed. Sample motion arises in living tissues from a variety of sources:

microscale active motion due to molecular motors and metabolic processes, bulk motion caused by muscle contractions including the pulse of the animal, as well as diffusive or Brownian motion of particles in the fluid environment of the tissue.

Additionally, the blood present in living tissues is highly absorptive. Unlike scattering, tissue absorption is an irreversible process. In recent work, we have found that as little as 0.02% of the scattered wavefront can be used for reconstruction, provided the sample is highly scattering [8]. Therefore, we anticipate that absorption can be grouped into a category of generalized loss mechanisms (such as backscattering). This work will mainly focus on the first topic, sample motion. However, we note that sample absorption is a surmountable problem from the simple fact that we were able to record the following results. In this chapter, we will show that the TSOPC experiment is capable of reconstructing an incident wavefront through a living rabbit ear.

Tissue motion has been studied for a number of reasons, and has formed the basis of several emerging imaging techniques. Recent publications have shown that tissue motion can be a potential metric of the cellular response to anti-cancer drugs [9]. We are interested in both the effect of tissue motion on our system, and the ability to distinguish viable tissues from non-viable tissues based on our measurements.

9.2 Experimental Methods

As mentioned above, in the first step of the experiment a collimated laser beam was used to illuminate the ear of a rabbit, and the transmitted light was recorded in a hologram. In step two, the phase conjugate of the transmitted light was read out from the hologram and back-propagated through the ear. The reconstructed signal was recorded in

time and analysis of the signal decay yielded the time scale of the *in vivo* tissue perturbation. We repeated the measurement 0.5, 1, 2, 3, and 24 hours after the ear was excised, which revealed several perturbation mechanisms of different time scales.

A system similar to that described in Chapter 8 and shown in Fig. 8.1 was used in this experiment. The power of the signal, writing and reading beams were 48 mW, 48 mW, and 4.8 mW, respectively. A five second recording time was used throughout the experiments, since the reading process in photorefractive materials can erase the stored hologram. Using a power ratio of 1:10 between the read and write beams ensured a hologram lifetime of ~6 min. The ear of a New Zealand rabbit under deep anesthesia was gently held between two glass slides and mounted onto the sample holder as shown in Fig 9.1.

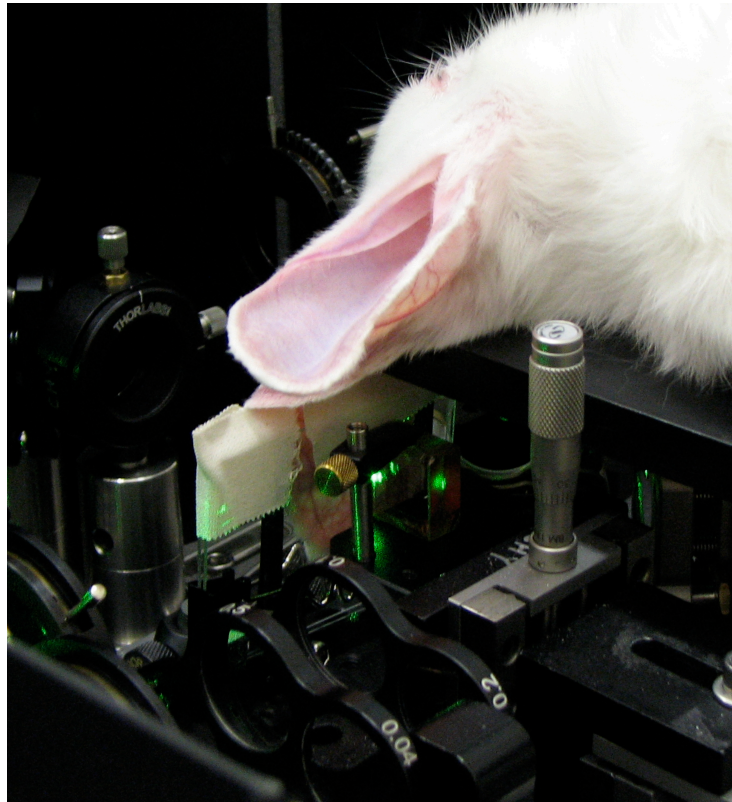


Figure 9.1. The ear of a New Zealand rabbit mounted in the TSOPC system

9.3 Results and Discussion

Figure 9.2 shows TSOPC spots reconstructed through the ear of the rabbit when it was alive (i, ii), 30 mins after euthanasia (iii), and through a tissue phantom of comparable scattering properties (iv). The signal reconstructed through the ear of the euthanized rabbit (iii) and the tissue phantom (iv) led to similar round spots, ~68 micron in diameter as expected from the 1.5 mm input beam diameter and the 150mm lens in front of the camera. The signal reconstructed through the living rabbit ear, however, deviated from the expected round spot (i, ii), indicating that the scattering structures in the tissue had moved during the recording process (5 sec) and distorted the hologram.

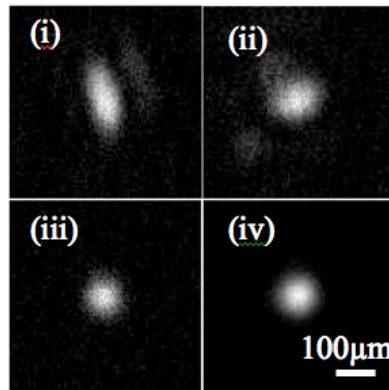


Figure 9.2. Reconstructed spots through a living rabbit ear (i) and (ii), a dead rabbit ear (iii), and tissue phantom of comparable properties (iv)

We were interested in measuring the sensitivity of the reconstructed TSOPC signal to tissue variations. To investigate the minimum length scale of the TSOPC perturbation, we mounted a 1.6 mm thick tissue phantom composed of polystyrene microsphere (1 micron in diameter, weight concentration 1.77%) suspended in a polyacrylamide hydrogel with $\mu_s L = 130$ on a translational stage driven by a piezo actuator. A laboratory-built laser fringe tracking system was employed to monitor the

stage position with better than 30 nm accuracy. After the holographic recording (experimental step one), we displaced the sample and monitored the TSOPC signal decay. Figure 9.3 shows the experimentally measured TSOPC signal as a function of sample displacement during TSOPC playback. Gaussian fitting (red line) yielded a FWHM of 523 nm.

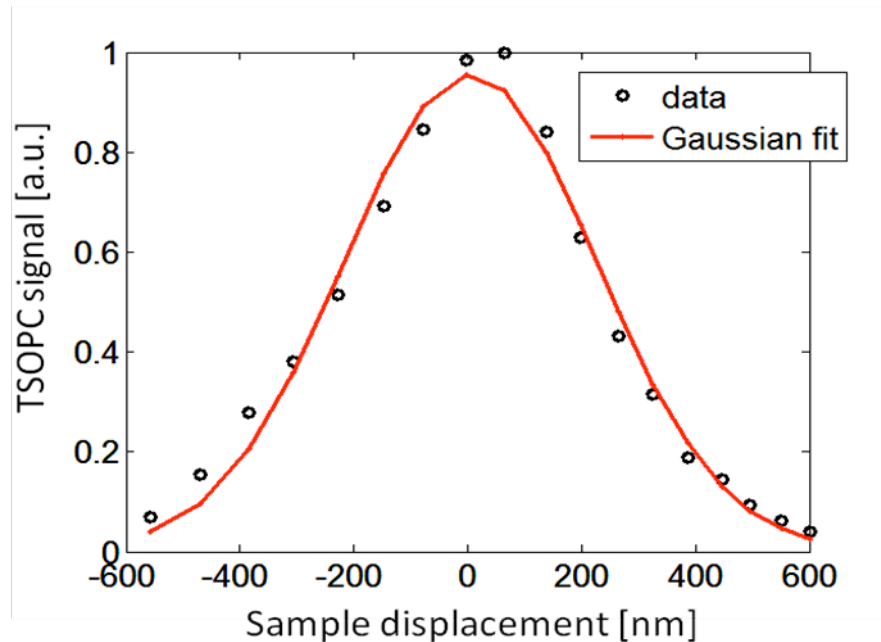


Figure 9.3. TSOPC signal versus sample displacement during playback. The data is fitted with a Gaussian function (red line).

The actual structural variations occurring inside the tissues are nevertheless different from the translational motion. First, the heart beat causes tissue vibration and bulk motion, which can move the tissue on a much greater length scale than the optical wavelength. Second, the cells within the tissue are undergoing active processes, and they vary their shape, size, and location over time. Third, living tissues are not solid like the hydrogel tissue phantoms. Figure 9.4 is a microscope image of a histology slide of the ear of the rabbit, showing complex structures in a fluidic environment. The Brownian motion

of the suspended particles can alter the tissue scattering. All of these factors can significantly perturb the time reversal process, and each has its own time scale.

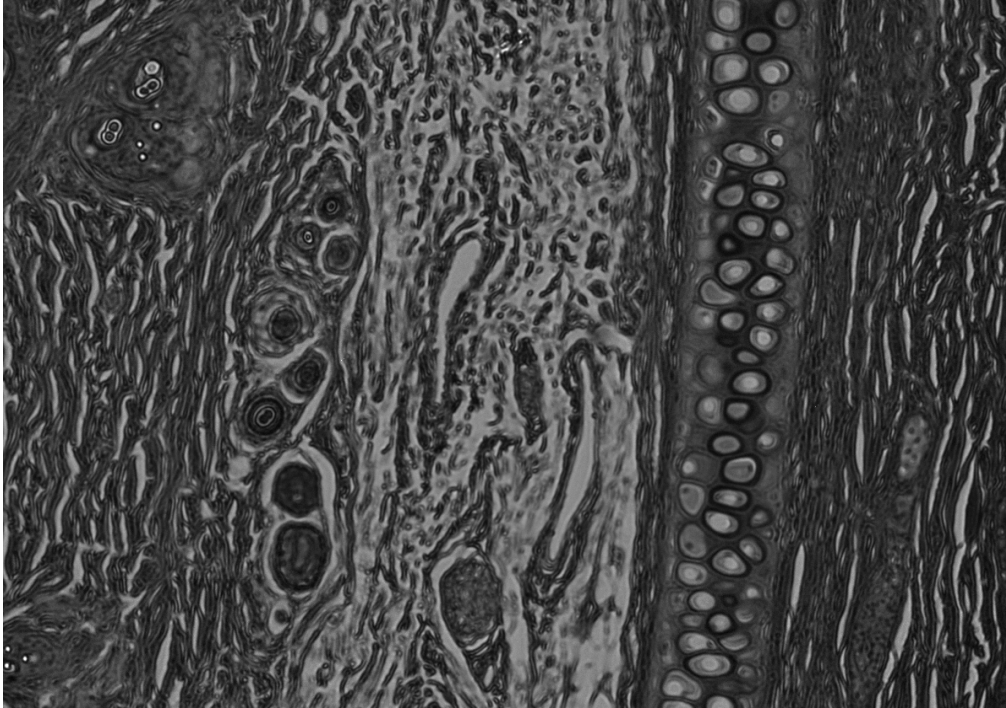


Figure 9.4. Histology of a cross section of the rabbit ear stained with hematoxylin and eosin. The vertical structure towards the right side of the image is cartilage. The circular structures on the left side of the image are blood vessels.

Figure 9.5 shows the TSOPC signal decay curves measured when the rabbit was alive, as well as 0.5, 1, 2, 3, and 24 hours after the ear was excised. An exponential function $a \cdot \exp(-t/\tau)$ was used to fit the decay and yield the decay constant τ . As we predicted from Fig. 9.2 (i, ii), the perturbation of a living rabbit ear (Fig. 9.5 (a) $\tau=1.5$ sec) was indeed faster than the holographic recording time (5 sec). After the excision, the decay time quickly increased and then gradually reached a plateau ($\tau=0.5$ min). To separate the decay caused by the tissue variation from the hologram decay and laser

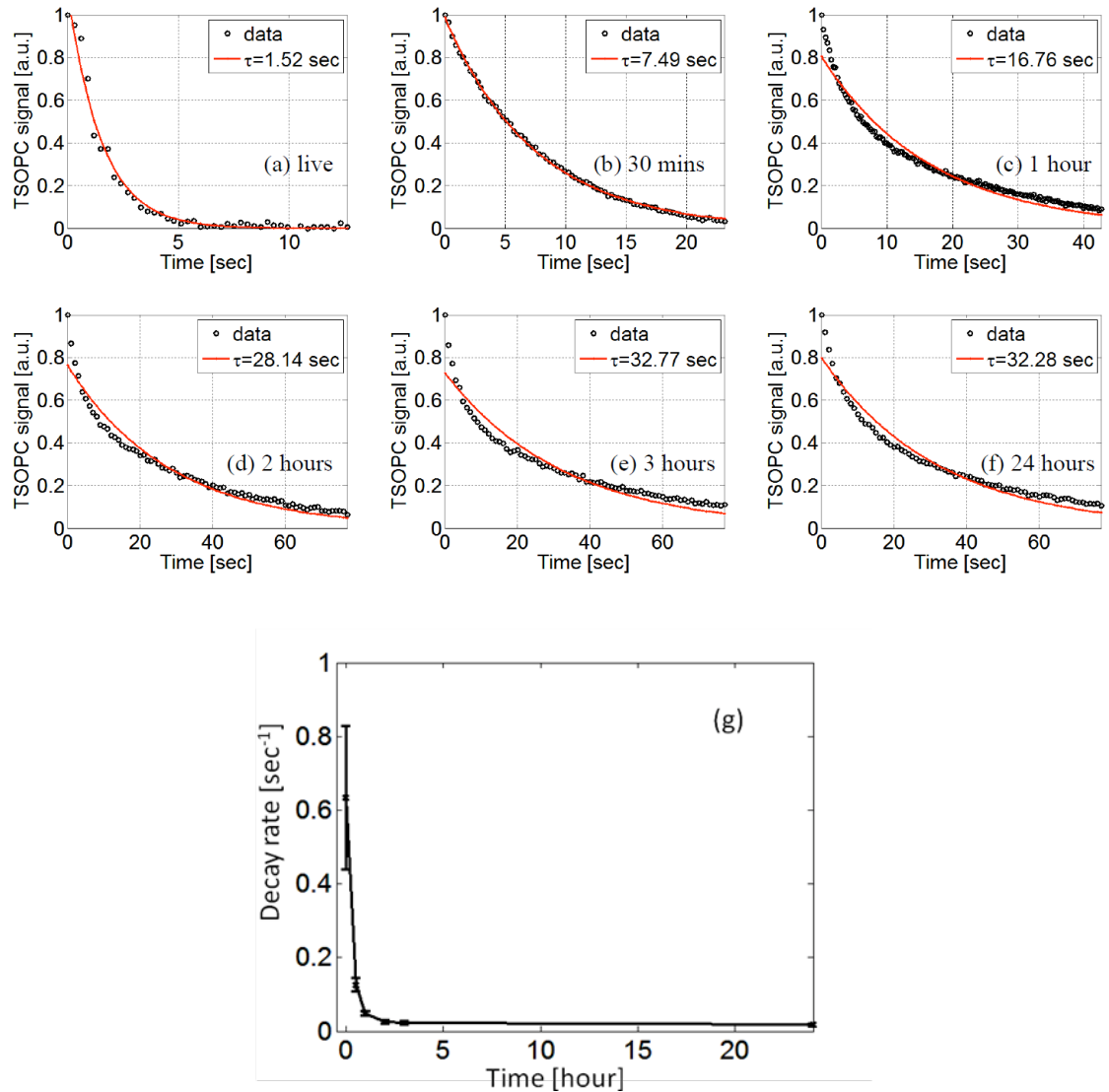


Figure 9.5 (a–f) TSOPC signal decay measured when the rabbit was alive and 0.5, 1, 2, 3, 24 hours after the ear is excised. The data is fitted with an exponential function (red line). (g) shows the decay rate variation as a function of the measurement time. The signal decay rate associated with the laser and mechanical instability is subtracted from the data.

and mechanical instabilities, we performed the TSOPC experiment without a scattering medium present, from which we identified a hologram life time of 6 min. We then measured the TSOPC signal decay as a function of time for a polyacrylamide tissue phantom with $\mu_s L$ comparable to the ear of the rabbit. The measured decay time ($\tau=2$ min) is due to the laser and mechanical instabilities. In Fig. 3 (g), we plotted the decay

rate ($1/\tau$) as a function of the measurement time and subtracted $1/(2 \text{ min})$ to account for the instabilities of the system. After the excision, the bulk motion due to muscle contractions no longer affected the ear, leading to the initial fast drop of the decay rate in Fig. 3 (g). The cells in the tissue, however, were still initially alive and gradually stopped their functioning. In ~ 2 hours, the decay rate reached a plateau that was still much faster than the decay rate of the tissue phantom. We attribute this effect to the fluidic environment inside the tissues and associated Brownian motion.

9.4 Conclusions

In conclusion, we performed *in vivo* TSOPC experiment on a living rabbit ear and monitored the signal decay as a function of time. We repeated the measurement after the ear was excised and identified three different mechanisms: heart beat, microscale cellular motion, and Brownian motion in the fluidic environment. In living tissues, bulk motion due to the heart beat and associated muscle contractions seem to be the dominant perturbation mechanism with the shortest decay time. Even so, the experimentally measured 1.5 second decay time showed that TSOPC is promising for *in vivo* applications. This time can be improved with a faster time reversal process such as four-wave mixing (FWM) or Brillouin scattering.

Chapter 10. Potential Applications and Future Work for TSOPC

10.1 Potential Applications

The preceding chapters describe proof-of-concept and characterization experiments for TSOPC. The ultimate goal of this work is to lay the groundwork for high-resolution deep tissue optical imaging. This is a significant challenge, however, and we have not yet formulated any reasonable methods to accomplish this feat. The following sub-sections will describe several preliminary scenarios in which TSOPC may prove to be useful in a biological setting. These experiments have not yet been attempted in the laboratory.

10.1.1 Light Concentrating Applications

An initial application involves the ability to focus light at specific locations within a scattering media or piece of tissue. Consider the experiment depicted in Fig. 10.1, noting that this experiment functions in a backscattering mode as opposed to the transmission mode experiments we have discussed thus far. The details of how a backscattering geometry may be experimentally implemented are described in the following Future Work

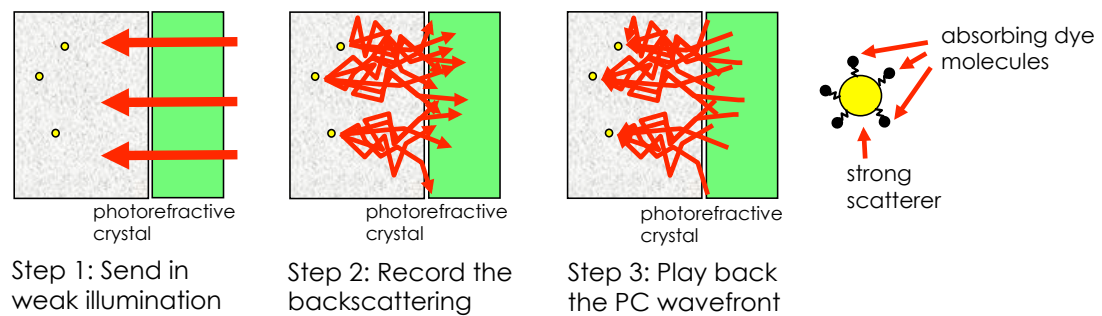


Figure 10.1. Diagram depicting potential light concentrating experiments

section. The experiment begins with a piece of tissue containing strong scatterers, such as gold nano-particles, injected into the region of interest. These particles scatter much more strongly than the background tissue scattering. A weak beam is used to illuminate the tissue (step 1), and the backscattering is recorded in a hologram or otherwise reflected off of a phase conjugate mirror (step 2). Upon playback (step 3), the phase conjugate beam must retrace its path through the sample, encountering each of the scatterers that the original incident beam encountered. The playback process will essentially focus light back to the strong scatterers in the sample.

We think the above scenario could potentially be useful in two types of situations. First, this may be useful for photodynamic therapy (PDT). We can envision coating strong scatterers with a dye, or other photoactivatable PDT agent, and optimizing our current system such that it is possible to replay the stored information at a high power. Thus, we could use weak illumination to probe the sample and encode the location of the strong scatterers, then play back a strong beam in order to release PDT agents or otherwise destroy the tissue locally. This would spare the remaining tissue a high dose of optical power. A variation on this idea is to use TSOPC to charge implantable photovoltaics. Through a similar scheme it should be possible to probe a tissue, determine the location of an implanted photovoltaic, then replay a strong beam directed to that area for charging purposes. This could potentially allow for implanted devices, such as pacemakers, to be charged internally.

In order to demonstrate that these applications are possible, we have several experiments in mind. The initial experiments will likely involve stationary tissue phantoms. One idea is to use a tissue phantom composed of strong scatterers tagged with

fluorescent molecules. If light is indeed preferentially focused back to these locations, the fluorophores should photobleach more quickly when illuminated with a phase conjugate beam than with plane wave illumination of the same power. By monitoring the fluorescent signal we can indirectly measure how much light is returning to the strong scatterers. Additionally, we would like to run the simple experiment of embedding a photodiode within a tissue phantom, and trying to determine whether it is possible to measure an increased signal using a phase conjugate beam as opposed to plane wave illumination. Success in these two experiments would mean that the applications described above are feasible in living tissues.

10.1.2 Absorption Amplification Applications

An additional application of TSOPC that we think may be useful in the short term involves the potential ability to highlight weak absorbers buried in a scattering medium. This would require our TSOPC experiment to be performed iteratively, as diagrammed in Fig. 10.2. For this application we revert back to the transmission mode experiment that we have been performing in previous work. In an iterative implementation of TSOPC, elastic scattering

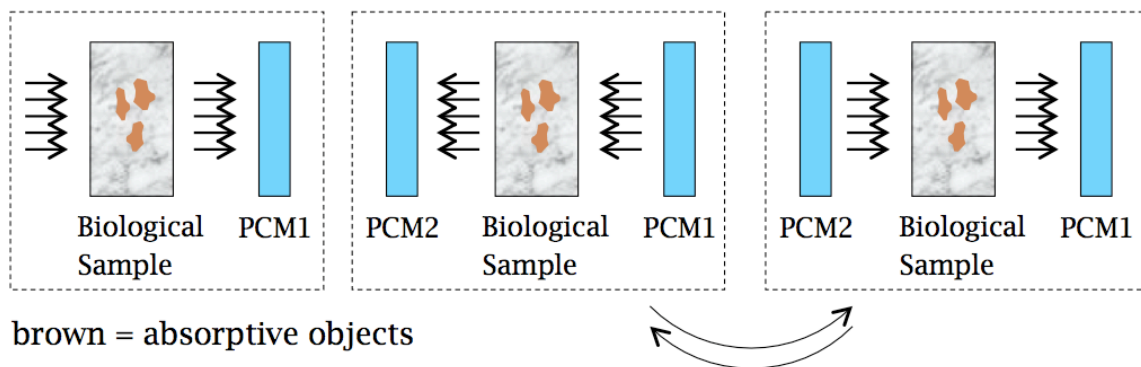


Figure 10.2. Diagram depicting potential absorption amplification experiments

would be time reversed on each round trip through the sample. However, absorption would occur during each pass. Thus, with each additional round trip, absorption in the sample would be amplified with respect to scattering. This could potentially allow for sensitive measurements of absorbers such as glucose through a non-invasive measurement. Although this measurement would be performed in transmission, there are several areas of the body that can be targeted for such a measurement, including the ear lobes and webbing between the fingers. Although conceptually simple, this may be a technically challenging experiment to implement as the phase conjugating devices must be appropriately synchronized in time.

10.1.3 Wavelength tuning for light selection

This sub-section details one of the few entirely independent ideas that I have had during my graduate career. The idea is to couple TSOPC to an imaging technique such as OCT, to increase the SNR and depth penetration.

The potential experiment is diagrammed in Fig. 10.3. Here, we will again be working in backscattering mode. We first probe the sample with an incident beam (Fig. 10.3(1)), and record the backscattering in a hologram (Fig. 10.3(2)). Then, as the scattered wavefront is played back into the tissue, the wavelength is slightly changed (shown as orange in Fig. 10.3(3)). The idea is that for tortuous paths through the sample, phase errors will add up, and the incident beam will not be reconstructed. However, the relatively straight paths through the sample will be largely unaffected by the wavelength change. The beam reconstructed by the shifted wavelength is split off by a beamsplitter and recorded in a second hologram (Fig. 10.3(3)). This hologram contains information about only the

relatively straight paths through the sample. The second hologram can then be played out and used for OCT imaging in which the majority of the incident power is directed into singly scattered paths. This could serve to dramatically increase the SNR and penetration depth of the OCT system.

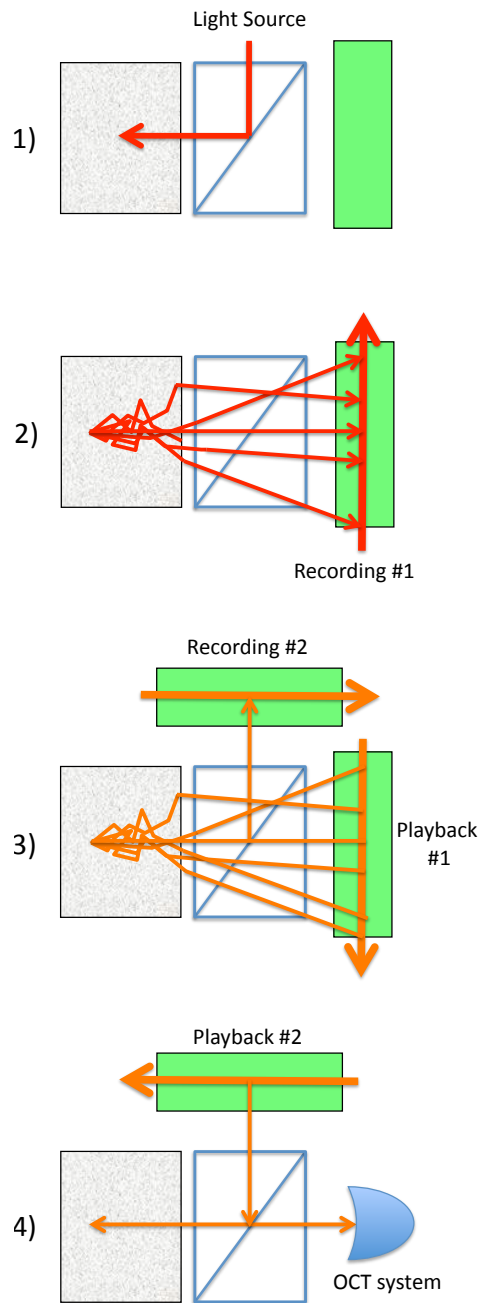


Figure 10.3. Diagram depicting wavelength tuning experiments

10.2 Future Work

Our proof-of-concept and characterizations experiments leave significant room for improvement. This section will describe some of the future work that we have planned in the context of the TSOPC experiment described in the preceding chapters.

An initial goal that we would like to accomplish is to build a TSOPC setup that functions in reflection mode. For these types of systems to be useful in realistic setting (and for human use), we would like to collect and replay light that has backscattered from the sample. This way our light delivery and collection optics can be located on one side of the sample, making experiments more practical. We would like our photorefractive crystal (or other holographic material) to be as close to the face of the sample as possible, in order to collect the maximum amount of light. This is difficult, however, because the crystal must share the same space as the light delivery optics. A separate beamsplitter and photorefractive crystal would require that the crystal be placed a distance equal to the size of the beamsplitter from the sample (similar to the setup shown in Fig. 10.3). One possible alternative solution is diagrammed in Fig. 10.4. Here, a holographic material is sandwiched between two glass prisms, effectively creating a beamsplitter. A portion of the incident beam is reflected towards the tissue, which interferes upon backscattering with the

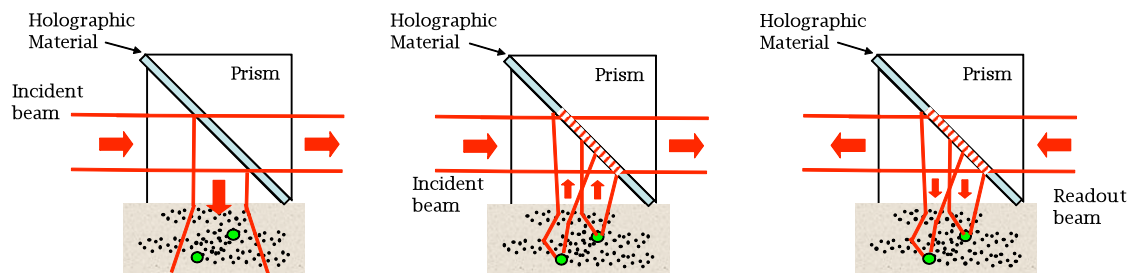


Figure 10.4. A potential experimental implementation of a reflection mode TSOPC system

light that had passed straight through the prisms. Playback of the phase conjugate field occurs as before, by reversing the direction of the reference beam.

A second major improvement that we would like to implement is the development of a digital version of the TSOPC experiment. The photorefractive crystal would be replaced by a CCD camera, used to record the interference fringes between the scattered and reference light field. A spatial light modulator (SLM) would be used to play back the phase conjugate field. The advantage over our current implementation is that we would be able to arbitrarily increase the power of the phase conjugate field, which is currently limited by erasure in the crystal. The challenge would be to adequately sample the interference pattern, which is essentially a speckle pattern for the case of a strongly scattering sample, and to replay the time reversed field with sufficient resolution. Our ability to succeed in this respect may be strongly linked to the state-of-the-art in SLM technology.

Additional improvements that we would like to integrate include faster holographic methods, such as photorefractive polymers, or real-time OPC methods, made possible through four-wave mixing or stimulated Brillouin scattering. The incorporation of reading and playback in two orthogonal polarization may also help us to increase the efficiency of our TSOPC experiment.

Chapter 11. Conclusions

In conclusion, we have tied together a relatively disparate set of experiments through the context of light scattering. Each individual experiment in this thesis is intended to help a reader contend with the challenge of light scattering in optical imaging experiments.

In the first half of this thesis, we pointed out several methods by which the SNR of a coherence domain imaging system can be optimized. This could be achieved by choosing optimal algorithms for signal reconstruction, making use of phase knowledge. Alternatively, these types of systems could be optimized by choosing appropriate detection parameters (specifically integration time) to limit the influence of $1/f$ noise. We gave the reader an outline in Chapter 5 for applying the various analyses to their own work.

In the second half of the document, we presented several experiments that we hope will lay the groundwork for high-resolution deep tissue optical imaging. We fully characterized our system to suppress turbidity in biological samples using optical phase conjugation, in terms of both amplitude and resolution trends. We found that our system is quite robust, and that high levels of scattering are actually beneficial in terms of signal collection. Finally, we showed the first set of results detailing time reversal in living tissues.

We hope that this work is generally useful for biophotonics researchers, and look forward to exciting results from the potential future experiments listed in Chapter 10.

References

1. Vo-Dinh T (2003) *Biomedical photonics handbook* (CRC Press, New York, New York).
2. The Warren Research Group at Duke University, <http://www.chem.duke.edu/~wwarren/tissueimaging.php>.
3. Wang LV, Wu H (2007) *Biomedical optics: Principles and imaging* (John Wiley & Sons, Inc., Hoboken, New Jersey).
4. Van de Hulst HC (1981) *Light scattering by small particles* (Dover Publications, Inc., New York, New York).
5. Prahl S, Mie scattering calculator, http://omlc.org.edu/calc/mie_calc.html.
6. Pyhtila JW, Wax A (2004) Rapid, depth-resolved light scattering measurements using Fourier domain, angle-resolved low coherence interferometry. *Optics Express* 12(25):6178–6183.
7. Brown WJ, Pyhtila JW, Terry NG, Chalut KJ, D'Amico TA, Sporn TA, Obando JV, Wax A (2008) Review and recent development of angle-resolved low-coherence interferometry for detection of precancerous cells in human esophageal epithelium. *IEEE Journal of Selected Topics in Quantum Electronics* 14(1):88–97.
8. Zevallos ME, Gayen SK, Das BB, Alrubaiee M, Alfano RR (1999) Picosecond electronic time-gated imaging of bones in tissues. *IEEE Journal of Selected Topics in Quantum Electronics* 5(4):916–922.
9. Chen H, Chen Y, Dilworth D, Leith E, Lopez J, Valdmanis J (1991) 2-dimensional imaging through diffusing media using 150-fs gated electronic holography techniques. *Optics Letters* 16(7):487–489.
10. Wang L, Ho PP, Liu C, Zhang G, Alfano RR (1991) Ballistic 2-D imaging through scattering walls using an ultrafast optical Kerr gate. *Science* 253(5021):769–771.
11. Marengo S, Pepin C, Goulet T, Houde D (1999) Time-gated transillumination of objects in highly scattering media using a subpicosecond optical amplifier. *IEEE Journal of Selected Topics in Quantum Electronics* 5(4):895–901.
12. Rao KD, Patel HS, Jain B, Gupta PK (2005) Time-gated optical imaging through turbid media using stimulated raman scattering: Studies on image contrast. *Pramana — Journal of Physics* 64(2):229–238.

13. Henyey LG, Greenstein JL (1941) Diffuse radiation in the galaxy. *Astrophysical Journal* 93(1):70–83.
14. Wang LH, Jacques SL, Zheng LQ (1995) MCML — monte-carlo modeling of light transport in multilayered tissues. *Computer Methods and Programs in Biomedicine* 47(2):131–146.
15. Prah SA, Keijzer M, Jacques SL, Welch AJ (1989) A monte carlo model of light propagation in tissue. *Dosimetry of laser radiation in medicine and biology*, eds Muller GJ & Sliney DH (SPIE Press), Vol IS5, pp 102–111.
16. Boas DA, Brooks DH, Miller EL, DiMarzio CA, Kilmer M, Gaudette RJ, Zhang Q (2001) Imaging the body with diffuse optical tomography. *IEEE Signal Processing Magazine* 18(6):57–75.
17. Pogue B, Testorf M, McBride T, Osterberg U, Paulsen K (1997) Instrumentation and design of a frequency-domain diffuse optical tomography imager for breast cancer detection. *Optics Express* 1(13):391–403.
18. Chance B, Anday E, Nioka S, Zhou S, Hong L, Worden K, Li C, Murray T, Ovetsky Y, Pidikiti D, Thomas R (1998) A novel method for fast imaging of brain function, non-invasively, with light. *Optics Express* 2(10):411–423.
19. Huang D, Swanson EA, Lin CP, Schuman JS, Stinson WG, Chang W, Hee MR, Flotte T, Gregory K, Puliafito CA, Fujimoto JG (1991) Optical coherence tomography. *Science* 254(5035):1178–1181.
20. Izatt JA, Kulkarni MD, Wang HW, Kobayashi K, Sivak MV (1996) Optical coherence tomography and microscopy in gastrointestinal tissues. *IEEE Journal of Selected Topics in Quantum Electronics* 2(4):1017–1028.
21. Fercher AF, Drexler W, Hitzenberger CK, Lasser T (2003) Optical coherence tomography — principles and applications. *Reports on Progress in Physics* 66(2):239–303.
22. Choma MA, Sarunic M, Yang C, Izatt JA (2003) Sensitivity advantage of swept source and Fourier domain optical coherence tomography. *Optics Express* 11(18):2183–2189.
23. de Boer JF, B. C, Park B, Pierce M, Tearney G, Bouma B (2003) Improved signal-to-noise ratio in spectral-domain compared with time-domain optical coherence tomography. *Optics Letters* 28(21):2067–2069.
24. Leitgeb R, Hitzenberger CK, Fercher AF (2003) Performance of Fourier domain vs. time domain optical coherence tomography. *Optics Express* 11(8):889–894.

25. Rollins AM, Izatt JA (1999) Optimal interferometer designs for optical coherence tomography. *Optics Letters* 24(21):1484–1486.
26. Johnson JB (1928) Thermal agitation of electricity in conductors. *Physical Review* 32(1):97–109.
27. Nyquist H (1928) Thermal agitation of electric charge in conductors. *Physical Review* 32(1):110–113.
28. van der Lee AM, Mieremet AL, van Exter MP, van Druten NJ, Woerdman JP (2000) Quantum noise in a laser with nonorthogonal polarization modes. *Physical Review A* 61(3):13.
29. American National Standards Institute (2000) Safe use of lasers. *Ansi z 136*, (Laser Institute of America, Orlando, Florida), pp 1–2000.
30. Jiao SL, Yu WR, Stoica G, Wang LHV (2003) Optical-fiber-based mueller optical coherence tomography. *Optics Letters* 28(14):1206–1208.
31. de Boer JF, Srinivas SM, Malekafzali A, Chen ZP, Nelson JS (1998) Imaging thermally damaged tissue by polarization sensitive optical coherence tomography. *Optics Express* 3(6):212–218.
32. Cang H, Sun T, Li ZY, Chen JY, Wiley BJ, Xia YN, Li XD (2005) Gold nanocages as contrast agents for spectroscopic optical coherence tomography. *Optics Letters* 30(22):3048–3050.
33. Morgner U, Drexler W, Kartner FX, Li XD, Pitris C, Ippen EP, Fujimoto JG (2000) Spectroscopic optical coherence tomography. *Optics Letters* 25(2):111–113.
34. Yang CH, McGuckin LEL, Simon JD, Choma MA, Applegate BE, Izatt JA (2004) Spectral triangulation molecular contrast optical coherence tomography with indocyanine green as the contrast agent. *Optics Letters* 29(17):2016–2018.
35. Sarunic MV, Applegate BE, Izatt JA (2005) Spectral domain second-harmonic optical coherence tomography. *Optics Letters* 30(18):2391–2393.
36. Applegate BE, Yang CH, Izatt JA (2005) Theoretical comparison of the sensitivity of molecular contrast optical coherence tomography techniques. *Optics Express* 13(20):8146–8163.
37. Davis A, Izatt J, Rothnerg F (2009) Quantitative measurement of blood flow dynamics in embryonic vasculature using spectral doppler velocimetry. *Anatomical Record — Advances in Integrative Anatomy and Evolutionary Biology* 292(3):311–319.

38. Herz PR, Chen Y, Aguirre AD, Fujimoto JG, Mashimo H, Schmitt J, Koski A, Goodnow J, Petersen C (2004) Ultrahigh resolution optical biopsy with endoscopic optical coherence tomography. *Optics Express* 12(15):3532–3542.
39. Han S, Sarunic MV, Wu J, Humayun M, Yang CH (2008) Handheld forward-imaging needle endoscope for ophthalmic optical coherence tomography inspection. *Journal of Biomedical Optics* 13(2):3.
40. McDowell EJ, Ellerbee AK, Choma MA, Applegate BE, Izatt JA (2007) Spectral domain phase microscopy for local measurements of cytoskeletal rheology in single cells. *Journal of Biomedical Optics* 12(4):11.
41. Choma MA, Ellerbee AK, Yang CH, Creazzo TL, Izatt JA (2005) Spectral-domain phase microscopy. *Optics Letters* 30(10):1162–1164.
42. Joo C, Akkin T, Cense B, Park BH, de Boer JE (2005) Spectral-domain optical coherence phase microscopy for quantitative phase-contrast imaging. *Optics Letters* 30(16):2131–2133.
43. McDowell EJ, Sarunic MV, Yaqoob Z, Yang C (2007) SNR enhancement through phase dependent signal reconstruction algorithms for phase separated interferometric signals. *Optics Express* 15(16):10103–10122.
44. Lai G, Yatagai T (1991) Generalized phase-shifting interferometry. *Journal of the Optical Society of America A — Optics Image Science and Vision* 8(5):822–827.
45. Yamaguchi I, Zhang T (1997) Phase-shifting digital holography. *Optics Letters* 22(16):1268–1270.
46. Post EJ (1967) Sagnac effect. *Reviews of Modern Physics* 39(2):475.
47. Jackson DA, Kersey AD, Lewin AC (1984) Fiber gyroscope with passive quadrature detection. *Electronics Letters* 20(10):399–401.
48. Sheem SK (1980) Fiberoptic gyroscope with [3x3] directional coupler. *Applied Physics Letters* 37(10):869–871.
49. Yaqoob Z, Wu JG, Cui XQ, Heng X, Yang CH (2006) Harmonically-related diffraction gratings-based interferometer for quadrature phase measurements. *Optics Express* 14(18):8127–8137.
50. Wu J, Yaqoob Z, Heng X, Cui X, Yang C (2007) Harmonically matched grating-based full-field quantitative high-resolution phase microscope for observing dynamics of transparent biological samples. *Optics Express* 15(26):18141–18155.

51. Yaqoob Z, Fingler J, Heng X, Yang C (2006) Homodyne *en face* optical coherence tomography. *Optics Letters* 31:1815–1817.
52. Choma MA, Yang CH, Izatt JA (2003) Instantaneous quadrature low-coherence interferometry with 3 x 3 fiber-optic couplers. *Optics Letters* 28(22):2162–2164.
53. Snyder AW (1972) Coupled-mode theory for optical fibers. *Journal of the Optical Society of America* 62(11):1267–1277.
54. Sheem SK (1981) Optical fiber interferometers with [3by3] directional-couplers — analysis. *Journal of Applied Physics* 52(6):3865–3872.
55. Sarunic MV, Choma MA, Yang CH, Izatt JA (2005) Instantaneous complex conjugate resolved spectral domain and swept-source OCT using 3x3 fiber couplers. *Optics Express* 13(3):957–967.
56. Sarunic MV, Applegate BE, Izatt JA (2006) Real-time quadrature projection complex conjugate resolved Fourier domain optical coherence tomography. *Optics Letters* 31(16):2426–2428.
57. Barry JR, Lee EA (1990) Performance of coherent optical receivers. *Proceedings of The IEEE* 78(8):1369–1394.
58. Kazovsky LG (1985) Optical heterodyning versus optical homodyning: A comparison. *Journal of Optical Communications* 6(1):18–24.
59. Personick SD (1971) Image band interpretation of optical heterodyne noise. *Bell System Technical Journal* 50(1):213.
60. Smith ME, Strange JH (1996) NMR techniques in materials physics: A review. *Measurement Science & Technology* 7(4):449–475.
61. Andersen AH, Kirsch JE (1996) Analysis of noise in phase contrast MR imaging. *Medical Physics* 23(6):857–869.
62. Constantinides CD, Atalar E, McVeigh ER (1997) Signal-to-noise measurements in magnitude images from nmr phased array. *Magnetic Resonance in Medicine* 38:852–857.
63. Erdogmus D, Yan R, Larsson EG, Principe JC, Fitzsimmons JR (2004) Image construction methods for phased array magnetic resonance imaging. *Journal of Magnetic Resonance Imaging* 20(2):306–314.
64. Aydin N, Markus HS (2001) Time-scale analysis of quadrature Doppler ultrasound signals. *IEE Proceedings — Science Measurement and Technology* 148(1):15–22.

65. McDowell EJ, Cui X, Yaqoob Y, Yang C (2007) A generalized noise variance analysis model and its application to the characterization of $1/f$ noise. *Optics Express* 15(7):3833–3848.
66. Dutta P, Horn PM (1981) Low-frequency fluctuations in solids — $1/f$ noise. *Reviews of Modern Physics* 53(3):497–516.
67. Press WH (1978) Flicker noises in astronomy and elsewhere. *Comments on Astrophysics* 7(4):103–119.
68. Weissman MB (1988) $1/f$ noise and other slow, nonexponential kinetics in condensed matter. *Reviews of Modern Physics* 60(2):537–571.
69. Li WT, Holste D (2005) Universal $1/f$ noise, crossovers of scaling exponents, and chromosome-specific patterns of guanine-cytosine content in DNA sequences of the human genome. *Physical Review E* 71(4).
70. Voss RF (1978) Linearity of $1/f$ noise mechanisms. *Physical Review Letters* 40(14):913–916.
71. Ivanov PC, Amaral LAN, Goldberger AL, Havlin S, Rosenblum MG, Stanley HE, Struzik ZR (2001) From $1/f$ noise to multifractal cascades in heartbeat dynamics. *Chaos* 11(3):641–652.
72. Musha T, Higuchi H (1976) $1/f$ fluctuation of a traffic current on an expressway. *Japanese Journal Of Applied Physics* 15(7):1271–1275.
73. Milotti E (2001) $1/f$ noise: A pedagogical review. (*invited talk to E-GLEA-2*).
74. Kaulakys B, Gontis V, Alaburda M (2005) Point process model of $1/f$ noise vs a sum of lorentzians. *Physical Review E* 71(5).
75. Johnson JB (1925) The schottky effect in low frequency circuits. *Physical Review* 26(1):0071–0085.
76. Schottky W (1926) Small-shot effect and flicker effect. *Physical Review* 28(1):74–103.
77. Siwy Z, Fulinski A (2002) Origin of $1/f(\alpha)$ noise in membrane channel currents. *Physical Review Letters* 89(15).
78. Greco V, Iemmi C, Ledesma S, Mannoni A, Molesini G, Quercioli F (1994) Multiphase homodyne displacement sensor. *Optik* 97(1):15–18.

79. Liu XQ, Clegg W, Jenkins DFL, Liu B (2001) Polarization interferometer for measuring small displacement. *IEEE Transactions on Instrumentation and Measurement* 50(4):868–871.
80. Wu CM, Su CS, Peng GS, Huang YJ (1996) Polarimetric, nonlinearity-free, homodyne interferometer for vibration measurement. *Metrologia* 33(6):533–537.
81. Chao C, Wang ZH, Zhu WG, Tan OK (2005) Scanning homodyne interferometer for characterization of piezoelectric films and microelectromechanical systems devices. *Review of Scientific Instruments* 76(6).
82. Mazzone DL, Davis CC (1991) Trace detection of hydrazines by optical homodyne interferometry. *Applied Optics* 30(7):756–764.
83. Beaurepaire E, Moreaux L, Amblard F, Mertz J (1999) Combined scanning optical coherence and two-photon-excited fluorescence microscopy. *Optics Letters* 24(14):969–971.
84. Choudhury N, Song GJ, Chen FY, Matthews S, Tschinkel T, Zheng JF, Jacques SL, Nuttall AL (2006) Low coherence interferometry of the cochlear partition. *Hearing Research* 220(1–2):1–9.
85. Salvade Y, Dandliker R (2000) Limitations of interferometry due to the flicker noise of laser diodes. *Journal of the Optical Society of America A — Optics Image Science and Vision* 17(5):927–932.
86. Hamstra RH, Wendland P (1972) Noise and frequency-response of silicon photodiode operational amplifier combination. *Applied Optics* 11(7):1539.
87. Clarke J, Hsiang TY (1976) Low-frequency noise in tin and lead films at superconducting transition. *Physical Review B* 13(11):4790–4800.
88. Keshner MS (1982) $1/f$ noise. *Proceedings of The IEEE* 70(3):212–218.
89. Pellegrini B, Saletti R, Terreni P, Prudenziati M (1983) $1/f$ -gamma noise in thick-film resistors as an effect of tunnel and thermally activated emissions, from measures versus frequency and temperature. *Physical Review B* 27(2):1233–1243.
90. Caloyannidea MA (1974) Microcycle spectral estimates of $1-f$ noise in semiconductors. *Journal of Applied Physics* 45(1):307–316.
91. Mandelbrot BB, Wallis JR (1969) Some long-run properties of geophysical records. *Water Resources Research* 5(2):321.

92. McDowell EJ, Ren J, Yang C (2008) Fundamental sensitivity limit imposed by dark $1/f$ noise in the low optical signal detection regime. *Optics Express* 16(10):6822–6832.
93. Flyckt SO, Marmonier C (2002) *Photomultiplier tubes: Principles and applications* (Photonis, Brive, France).
94. Teich MC, Matsuo K, Saleh BEA (1986) Excess noise factors for conventional and superlattice avalanche photodiodes and photomultiplier tubes. *IEEE Journal of Quantum Electronics* 22(8):1184–1193.
95. Allan DW (1966) Statistics of atomic frequency standards. *Proceedings of the Institute of Electrical and Electronics Engineers* 54(2):221.
96. Barnes JA, Chi AR, Cutler LS, Healey DJ, Leeson DB, McGuniga Te, Mullen JA, Smith WL, Sydnor RL, Vessot RFC, Winkler GMR (1971) Characterization of frequency stability. *IEEE Transactions on Instrumentation and Measurement* IM20(2):105.
97. Gradshteyn IS, Ryzhik IM (2007) *Table of integrals, series, and products* (Elsevier Inc., San Diego), 7th Ed.
98. Leith EN, Upatniek J (1966) Holographic imagery through diffusing media. *Journal of the Optical Society of America* 56(4):523.
99. Levenson MD (1980) High-resolution imaging by wave-front conjugation. *Optics Letters* 5(5):182–184.
100. Gower MC (1982) KrF laser-amplifier with phase-conjugate brillouin retro-reflectors. *Optics Letters* 7(9):423–425.
101. Tomov IV, Fedosejevs R, Mcken DCD, Domier C, Offenberger AA (1983) Phase conjugation and pulse-compression of krF-laser radiation by stimulated raman-scattering. *Optics Letters* 8(1):9–11.
102. Frejlich J (2007) *Photorefractive materials: Fundamental concepts, holographic recording and materials characterization* (John Wiley & Sons, Hoboken, NJ).
103. Boyd RW (2003) *Nonlinear optics* (Academic Press, San Diego), 2nd Ed.
104. Goodman JW (2005) *Introduction to Fourier optics* (Roberts and Company Publishers), 3rd Ed.
105. Leith EN, Upatnieks J (1962) Reconstructed wavefronts and communication theory. *Journal of the Optical Society of America* 52(10):1123.

106. Yariv A, Pepper DM (1977) Amplified reflection, phase conjugation and oscillation in degenerate four-wave mixing. *Optics Letters* 1(1).
107. Hellwarth RW (1977) Generation of time-reversed wave fronts by nonlinear refraction. *Journal of the Optical Society of America* 67(1):1–3.
108. Jensen SM, Hellwarth RW (1978) Observation of time-reversed replica of a monochromatic optical-wave. *Applied Physics Letters* 32(3):166–168.
109. Bloom DM, Bjorklund GC (1977) Conjugate wavefront generation and image-reconstruction by 4-wave mixing. *Applied Physics Letters* 31(9):592–594.
110. Yaqoob Z, Psaltis D, Feld MS, Yang C (2008) Optical phase conjugation for turbidity suppression in biological samples. *Nature Photonics* 2:110–115.
111. Jones DC, Ridley KD (1997) Experimental investigation by stimulated Brillouin scattering of incomplete phase conjugation. *Journal of the Optical Society of America B — Optical Physics* 14(10):2657–2663.
112. McMichael I, Ewbank MD, Vachss F (1995) Efficiency of phase-conjugation for highly scattered-light. *Optics Communications* 119(1–2):13–16.
113. Gibson AP, Hebden JC, Arridge SR (2005) Recent advances in diffuse optical imaging. *Physics in Medicine and Biology* 50(4):R1–R43.
114. Vellekoop IM, Mosk AP (2007) Focusing coherent light through opaque strongly scattering media. *Optics Letters* 32(16):2309–2311.
115. Vellekoop IM, Mosk AP (2008) Universal optimal transmission of light through disordered materials. *Physical Review Letters* 101(12):4.
116. Gu C, Yeh PC (1994) Partial phase-conjugation, fidelity, and reciprocity. *Optics Communications* 107(5–6):353–357.
117. Jakeman E, Ridley KD (1996) Incomplete phase conjugation through a random-phase screen. 1. Theory. *Journal of the Optical Society of America A — Optics Image Science and Vision* 13(11):2279–2287.
118. Ridley KD, Jakeman E (1996) Incomplete phase conjugation through a random phase screen. 2. Numerical simulations. *Journal of the Optical Society of America A—Optics Image Science and Vision* 13(12):2393–2402.
119. Yariv A (1978) Phase conjugate optics and real-time holography. *IEEE Journal of Quantum Electronics* 14(9):650–660.

120. Feinberg J, Hellwarth RW (1980) Phase-conjugating mirror with continuous-wave gain. *Optics Letters* 5(12):519–521.
121. Lind RC, Steel DG (1981) Demonstration of the longitudinal modes and aberration-correction properties of a continuous-wave dye-laser with a phase-conjugate mirror. *Optics Letters* 6(11):554–556.
122. Drummond PD, Friberg AT (1983) Specular reflection cancellation in an interferometer with a phase-conjugate mirror. *Journal of Applied Physics* 54(10):5618–5625.
123. Gower M, Proch D (1994) *Optical phase conjugation* (Springer-Verlag, New York, NY).

Appendix D1: Chapter 3 Derivations

D1.1 Derivation of Variance for Heterodyne Detection

$$E[M_{heterodyne}(N_i)] = E \left[\left(\sum_{i=1}^X (N_{i,1} - N_{i,2}) \cos(\Delta\omega_i) \right)^2 + \left(\sum_{i=1}^X (N_{i,1} - N_{i,2}) \sin(\Delta\omega_i) \right)^2 \right]$$

$$= E \left[\sum_{i=1}^X (N_{i,1}^2 + N_{i,2}^2) (\cos^2(\Delta\omega_i) + \sin^2(\Delta\omega_i)) \right] = 2X E[N_i^2] = 2X\sigma^2$$

$$E[M_{heterodyne}(N_i)^2] = E \left[\left(\left(\sum_{i=1}^X (N_{i,1} - N_{i,2}) \cos(\Delta\omega_i) \right)^2 + \left(\sum_{i=1}^X (N_{i,1} - N_{i,2}) \sin(\Delta\omega_i) \right)^2 \right)^2 \right]$$

$$= E \left[\begin{aligned} & \sum_{i=1}^X (N_{i,1} - N_{i,2})^4 \cos^4(\Delta\omega_i) \\ & + 3 \sum_{i=1}^X \sum_{\substack{j=1 \\ i \neq j}}^X (N_{i,1} - N_{i,2})^2 \cos^2(\Delta\omega_i) (N_{j,1} - N_{j,2})^2 \cos^2(\Delta\omega_j) \\ & + \sum_{i=1}^X (N_{i,1} - N_{i,2})^4 \sin^4(\Delta\omega_i) \\ & + 3 \sum_{i=1}^X \sum_{\substack{j=1 \\ i \neq j}}^X (N_{i,1} - N_{i,2})^2 \sin^2(\Delta\omega_i) (N_{j,1} - N_{j,2})^2 \sin^2(\Delta\omega_j) \\ & + 2 \sum_i^X (N_{i,1} - N_{i,2})^4 \cos^2(k\nu\tau_i) \sin^2(\Delta\omega_i) \\ & + 2 \sum_{i=1}^X \sum_{\substack{j=1 \\ i \neq j}}^X (N_{i,1} - N_{i,2})^2 \cos^2(\Delta\omega_i) (N_{j,1} - N_{j,2})^2 \sin^2(\Delta\omega_j) \\ & + 4 \sum_{i=1}^X \sum_{\substack{j=1 \\ i \neq j}}^X (N_{i,1} - N_{i,2})^2 \cos(\Delta\omega_i) \sin(\Delta\omega_i) (N_{j,1} - N_{j,2})^2 \cos(\Delta\omega_j) \sin(\Delta\omega_j) \end{aligned} \right]$$

where $E[(N_{i,1} - N_{i,2})^4] = 12\sigma^4$ and $E[(N_{i,1} - N_{i,2})^2] = 4\sigma^2$.

$$\begin{aligned}
&= 12\sigma^4 \sum_{i=1}^X \sum_{j=1}^X \cos^2(\Delta\omega_i) \cos^2(\Delta\omega_j) \\
&\quad + 12\sigma^4 \sum_{i=1}^X \sum_{j=1}^X \sin^2(\Delta\omega_i) \sin^2(\Delta\omega_j) \\
&\quad + 8\sigma^4 \sum_{i=1}^X \sum_{j=1}^X \cos^2(\Delta\omega_i) \sin^2(\Delta\omega_j) \\
&\quad + 16\sigma^4 \sum_{i=1}^X \sum_{j=1}^X \cos(\Delta\omega_i) \sin(\Delta\omega_i) \cos(\Delta\omega_j) \sin(\Delta\omega_j) \\
&= 12\sigma^4 \frac{X^2}{4} + 12\sigma^4 \frac{X^2}{4} + 8\sigma^4 \frac{X^2}{4} = 8\sigma^4 X^2
\end{aligned}$$

$$\sigma_{heterodyne}^2 = 8\sigma^4 X^2 - (2X\sigma^2)^2 = 4X^2\sigma^4$$

D1.2 Derivation of Variance for Heterodyne Detection with Phase Knowledge

$$\begin{aligned}
E[M_{heterodyne \text{ with phase knowledge}}(N_i)] &= E\left[\left(\sum_{i=1}^X (N_{i,1} - N_{i,2}) \cos(\Delta\omega_i)\right)^2\right] \\
&= E\left[\sum_{i=1}^X (N_{i,1}^2 + N_{i,2}^2) \cos^2(\Delta\omega_i)\right] = E[(N_{i,1}^2 + N_{i,2}^2)] \frac{X}{2} = 2\sigma^2 \frac{X}{2} = X\sigma^2
\end{aligned}$$

$$E[M_{heterodyne \text{ with phase knowledge}}(N_i)^2] = E\left[\left(\sum_{i=1}^X (N_{i,1} - N_{i,2}) \cos(\Delta\omega_i)\right)^4\right]$$

$$= E\left[\sum_{i=1}^X (N_{i,1} - N_{i,2})^4 \cos^4(\Delta\omega_i) + 3 \sum_{i=1}^X \sum_{\substack{j=1 \\ i \neq j}}^X (N_{i,1} - N_{i,2})^2 \cos^2(\Delta\omega_i) (N_{j,1} - N_{j,2})^2 \cos^2(\Delta\omega_j)\right]$$

$$= 12\sigma^4 \sum_{i=1}^X \sum_{j=1}^X \cos^2(\Delta\omega_i) \cos^2(\Delta\omega_j) = 12\sigma^4 \sum_{i=1}^X \cos^2(\Delta\omega_i) \sum_{j=1}^X \cos^2(\Delta\omega_j)$$

$$= 12\sigma^4 \frac{X^2}{4} = 3\sigma^4 X^2$$

$$\sigma_{\text{heterodyne with phase knowledge}}^2 = 3\sigma^4 X^2 - (X\sigma^2)^2 = 2X^2\sigma^4$$

D1.3 Derivation of Variance for Method 1

$$E[M_1(N_i)] = E\left[\frac{3}{2}(N_1^2 + N_2^2 + N_3^2)\right] = \frac{3}{2}E[N_i^2] = \frac{3}{2}\sigma^2$$

$$\begin{aligned} E[M_1(N_i)^2] &= E\left[\frac{9}{4}(N_1^2 + N_2^2 + N_3^2)^2\right] \\ &= E\left[\frac{9}{4}(N_1^4 + N_2^4 + N_3^4 + 2N_1^2N_2^2 + 2N_1^2N_3^2 + 2N_2^2N_3^2)\right] \end{aligned}$$

where $E[(N_i)^4] = 3\sigma^4$ and $E[(N_i)^2] = \sigma^2$

$$= \frac{9}{4}\left(3E[N_i^4] + 6E[N_i^2]E[N_i^2]\right) = \frac{81}{4}\sigma^4 + \frac{54}{4}\sigma^4 = \frac{135}{4}\sigma^4$$

$$\sigma_{M_1}^2 = \frac{135}{4}\sigma^4 - \frac{81}{4}\sigma^4 = \frac{27}{2}\sigma^4$$

D1.4 Derivation of Variance for Method 2

$$E[M_2(N_i)] = E\left[3(N_1^2 + N_2^2 + N_1N_2)\right] = 3\left(2E[N_i^2]\right) = 6\sigma^2$$

$$\begin{aligned} E[M_2(N_i)^2] &= E\left[9(N_1^2 + N_2^2 + N_1N_2)^2\right] \\ &= E\left[9(N_1^4 + N_2^4 + 3N_1^2N_2^2 + 2N_1^3N_2 + 2N_1N_2^3)\right] \\ &= 9\left(2E[N_i^4] + 3E[N_i^2]E[N_i^2]\right) = 54\sigma^4 + 27\sigma^4 = 81\sigma^4 \end{aligned}$$

$$\sigma_{M_2}^2 = 81\sigma^4 - (6\sigma^2)^2 = 45\sigma^4$$

D1.5 Derivation of Variance for Method 3

In order to derive the variance for Method 3 we will, for simplicity, choose $\theta=0$ (although any value of θ will give an equivalent solution), setting $a_1=2/3$, $a_2=1/6$, $a_3=1/6$.

$$\begin{aligned} E[M_3(N_i)] &= E\left[\frac{1}{4}\left(\frac{2/3 N_1}{1} + \frac{1/6 N_2}{-1/2} + \frac{1/6 N_3}{-1/2}\right)^2\right] = E\left[\frac{1}{4}\left(\frac{2}{3}N_1 - \frac{1}{3}N_2 - \frac{1}{3}N_3\right)^2\right] \\ &= \frac{1}{4}\left(\frac{4}{9}E[N_1^2] + \frac{1}{9}E[N_2^2] + \frac{1}{9}E[N_3^2]\right) = \sigma^2 + \frac{1}{4}\sigma^2 + \frac{1}{4}\sigma^2 = \frac{3}{2}\sigma^2 \end{aligned}$$

$$\begin{aligned} E[M_3(N_i)^2] &= E\left[\frac{81}{16}\left(\frac{4}{9}N_1^2 - \frac{4}{9}N_1N_2 - \frac{4}{9}N_1N_3 + \frac{2}{9}N_2N_3 + \frac{1}{9}N_2^2 + \frac{1}{9}N_3^2\right)^2\right] \\ &= \frac{81}{16}\left(\frac{18}{81}3\sigma^4 + \frac{54}{81}\sigma^4\right) = \frac{27}{4}\sigma^4 \end{aligned}$$

$$\sigma_{M_3}^2 = \frac{27}{4}\sigma^4 - \frac{9}{4}\sigma^4 = \frac{9}{2}\sigma^4$$

D1.6 Derivation of Variance for Method 3, n Ports

$$\begin{aligned} E[M_{3, n \text{ ports}}(N_i)] &= E\left[\frac{n^2}{4}\left(\sum_{i=1}^n \frac{a_i N_i}{\cos\left(\theta + \frac{2\pi}{n}(i-1)\right)}\right)^2\right] \\ &= E\left[\frac{n^2}{4}\sum_{i=1}^n \frac{a_i^2 N_i^2}{\cos^2\left(\theta + \frac{2\pi}{n}(i-1)\right)}\right] = \frac{n^2}{4}E[N_i^2] \sum_{i=1}^n \frac{1}{\cos^2\left(\theta + \frac{2\pi}{n}(i-1)\right)} \\ &= \frac{n}{2}E[N_i^2] = \frac{n}{2}\sigma^2 \end{aligned}$$

$$E[M_{3, n \text{ ports}}(N_i)^2] = E\left[\frac{n^4}{16}\left(\sum_{i=1}^n \frac{a_i N_i}{\cos\left(\theta + \frac{2\pi}{n}(i-1)\right)}\right)^4\right]$$

$$= E \left[\frac{n^4 2^4}{16n^4} \left(\sum_{i=1}^n \cos \left(\theta + \frac{2\pi}{n} (i-1) \right) N_i \right)^4 \right]$$

This equation is of the same form as the heterodyne detection method described in Section D1.2, and can be solved in a similar manner

D1.7 Derivation of variance for Methods 4 and 5

Beginning with the reconstruction methods defined in Eqs. 3.36 and 3.40, as well as the signal and noise at each port given by Eqs. 3.2 and 3.3 where $n=3$, the expected value and variance of the noise for these methods can be determined following the analysis in section D1.1 and D1.2.

Appendix D2: Chapter 8 Derivation and Model

This derivation and model was developed by Ivo M. Vellekoop, a collaborator from the Physics Institute at the University of Zurich.

TSOPC Amplitude Derivation and Model

We consider the situation in which a phase conjugate mirror (PCM) is placed behind a scattering medium. The PCM can be any phase conjugating device including the holographic setup employing a photorefractive crystal described in this thesis. Light that propagates through the medium is phase conjugated and retraces its path back through the scattering medium to refocus at its origin. This section describes the trend of the intensity of the refocused light, for samples ranging from thin (transmission is mostly ballistic) to optically thick (transmitted light is completely diffuse). We assume that light propagation in the medium is reciprocal and that there are no nonlinear effects. We make no assumptions about absorption, efficiency of the PCM, light propagation, etc., unless explicitly stated.

Following the conventions of Gu and Yeh (116), we define the incident field E_1 , the transmitted field E_2 , the phase conjugated field E_3 and the field that has been transmitted back through the sample E_4 . Scattering in the sample is described by the scattering function, h , such that:

$$E_2(x',y') = \iint E_1(x,y)h(x,y,x',y')dxdy, \quad (\text{D2.1})$$

with input coordinates (x,y) and output coordinates (x',y') . Because of reciprocity, propagation back is described by:

$$E_4(x, y) = \iint E_3(x', y') h(x, y, x', y') dx' dy'. \quad (\text{D2.2})$$

For simplicity, we take the incident field to be a delta function¹ with amplitude $E_{in} \equiv \sqrt{P_{in}}$, where P_{in} is the total incident power.

The fields propagating toward the PCM are now given by:

$$E_1(x, y) = E_{in} \delta(x, y), \quad (\text{D2.3})$$

$$E_2(x', y') = E_{in} h(0, 0, x', y'). \quad (\text{D2.4})$$

At the PCM, the field is reflected and phase conjugated. Since the PCM is not perfect, the reflected field has a certain envelope $\alpha\rho(x', y')$, where $\rho(0, 0) = 1$ and α is the overall reflection coefficient of the phase conjugation². If the PCM reflects the field with exactly the same amplitude, $\alpha = 1$.

$$E_3(x', y') = \alpha\rho(x', y') E_2^*(x', y'). \quad (\text{D2.5})$$

For the reconstructed field E_4 , we are only interested in the part that overlaps with the incident field. The total power in this overlapping portion is given by:

$$P_{TSOPC} \equiv \iint \delta(x, y) |E_4(x, y)|^2 dx dy = |E_4(0, 0)|^2, \quad (\text{D2.6})$$

with

$$E_4(0, 0) \equiv \alpha E_{in} \iint \rho(x', y') |h(0, 0, x', y')|^2 dx' dy', \quad (\text{D2.7})$$

where (D2.2), (D2.4), and (D2.5) were used.

¹ In reality the incident field will not be a delta function. Regardless of the actual shape of the incident field, we are free to choose a coordinate system where the incident field corresponds to a delta function by applying an arbitrary unitary transform. Therefore, the results derived here are generally valid.

² In practice, α is not exactly constant over different experiments due to a number of reasons including the non-uniformity of the PCM, power fluctuations of the laser, and experimental human error from run to run. These fluctuations are visible in the data shown in this manuscript.

Two other important quantities in the experiment are the total transmitted power, P_T (P_2), and the total power exiting the PCM, P_{OPC} (P_3). These can be described as follows:

$$\begin{aligned} P_T &= \iint |E_2(x', y')|^2 dx' dy' \\ &= P_{in} \iint |h(0, 0, x', y')|^2 dx' dy', \\ &= P_{in} T \end{aligned} \quad (D2.8)$$

where T is the total (angle integrated) transmission. To simplify this notation we define:

$$|h(0, 0, x', y')|^2 \equiv TF(x', y'), \quad (D2.9)$$

where F is the intensity profile of the transmitted light, normalized such that

$\iint F(x', y') dx' dy' = 1$. Using this notation, the power exiting the PCM is given by:

$$\begin{aligned} P_{OPC} &= \iint |E_3(x', y')|^2 dx' dy' \\ &= \alpha^2 P_{in} \iint \rho^2(x', y') |h(0, 0, x', y')|^2 dx' dy', \\ &= \alpha^2 P_{in} TC_3 \end{aligned} \quad (D2.10)$$

where

$$C_3 \equiv \iint \rho^2(x', y') F(x', y') dx' dy'. \quad (D2.11)$$

C_3 describes the fraction of light that is ‘seen’ by the PCM. In Gu and Yeh, C_3 is approximated as a/A , where a is the surface area of the PCM and A is the total surface area of the diffuse light.

Using the same notation, Eq. D2.6 can be rewritten as:

$$P_{TSOPC} = \alpha^2 P_{in} T^2 C_4^2, \quad (D2.12)$$

where

$$C_4 \equiv \iint \rho(x', y') F(x', y') dx' dy'. \quad (D2.13)$$

Note that $C_3 \neq C_4$. C_3 describes the fraction of the intensity that is reflected, while C_4 can be thought of as the fraction of the amplitude. In the special case described by Gu and Yeh,

which includes a sharp aperture and uniform phase conjugation (i.e., $\rho=1$ or $\rho=0$), $C_3=C_4$.

In general, however, they are different.

We can now predict the trend of the TSOPC power by combining (D2.11) and (D2.13):

$$P_{TSOPC} = P_{OPC} T \frac{C_4^2}{C_3}. \quad (\text{D2.14})$$

The difficulty with this form is that a measurement of the total transmission, T , is very hard. In our experiments, the transmission is measured over a defined aperture associated with the photodetector, chosen to be approximately the same shape as the reference beam in the photorefractive crystal. The transmission measured in this manner, T_{meas} , is related to the total transmission, T , according to:

$$T_{meas} = \frac{1}{P_{In}} \iint \rho_{meas}^2(x', y') |E_2(x', y')|^2 dx' dy' = TC_2, \quad (\text{D2.15})$$

where ρ_{meas}^2 is the (intensity) profile of the aperture over which the transmission is measured and:

$$C_2 \equiv \iint \rho_{meas}^2(x', y') F(x', y') dx' dy'. \quad (\text{D2.16})$$

Finally, we can write the TSOPC amplitude trend as a function of the measured values, T_{meas} and P_{OPC} :

$$P_{TSOPC} = P_{OPC} T_{meas} \frac{C_4^2}{C_2 C_3}. \quad (\text{D2.17})$$

The constant $C_4^2/C_2 C_3$ must be determined experimentally.

In the diffuse regime, we can use Eq. D2.17 to predict the trend of the TSOPC amplitude. However, when the samples are so thin that the ballistic contribution becomes visible, the distribution of the transmitted intensity, F , will be different than in the diffuse

case. As a result, the constants above will depend on the thickness of the samples. To deal with this complication, we introduce a simple model. We assume that there are only two contributions to the transmission: completely ballistic and completely diffuse. Thus, we can write:

$$TF(x',y') = T_{ball}\delta(x',y') + T_{diff}F_{diff}(x',y'), \quad (D2.18)$$

where $F_{diff}(x',y')$ is the normalized profile of the diffuse transmission: $\iint F_{diff}(x',y')dx'dy' \equiv 1$. For thick samples, $F \rightarrow F_{diff}$. The Beer-Lambert law gives us the transmission coefficient for the ballistic component, and the transmission for the diffusive component follows from our assumptions above:

$$T_{ball} \equiv \exp(-\mu_s L), \quad (D2.19)$$

$$T_{diff} \equiv T - T_{ball}. \quad (D2.20)$$

Through this model, the total transmission remains equal to T. The values for C_2 , C_3 , and C_4 follow by inserting the model (D2.18) into their respective definitions:

$$TC_2 = T_{ball} + T_{diff}C'_2, \quad (D2.21)$$

$$TC_3 = T_{ball} + T_{diff}C'_3, \quad (D2.22)$$

$$TC_4 = T_{ball} + T_{diff}C'_4, \quad (D2.23)$$

where the ballistic component is always completely detected/reflected since $\rho(0,0) = \rho_{meas}(0,0) = 1$. The constant C'_2 is defined as:

$$C'_2 = \iint \rho_{meas}^2(x',y')F_d(x',y')dx'dy', \quad (D2.24)$$

analogous to Eq. D2.16, and similarly for C'_3 and C'_4 . These constants are calculated for the only diffuse portion of the distribution and therefore do not depend on the sample thickness.

To predict the trend of the TSOPC power, we use the following procedure to process the measurements. First, we take the measured OPC power (P_{OPC}),

$$P_{OPC} = P_{In} \alpha^2 [T_{ball} + T_{diff} C'_3], \quad (D2.25)$$

and normalize it by the OPC power when no sample is present ($P_{norm} = P_{In} \alpha_0^2$) where α_0 is the value of α for the first measurement in the series (i.e., no sample). We then subtract the ballistic transmission to arrive at:

$$\frac{P_{OPC}}{P_{norm}} - T_{ball} = \left[\frac{\alpha^2}{\alpha_0^2} - 1 \right] T_{ball} + \frac{\alpha^2}{\alpha_0^2} T_{diff} C'_3 \approx \frac{\alpha^2}{\alpha_0^2} T_{diff} C'_3. \quad (D2.26)$$

We must assume here that α does not fluctuate too wildly ($\alpha \approx \alpha_0$) so that the ballistic component can be removed. We do the same for the measured transmission, T_{meas} (no normalization required):

$$T_{meas} - T_{ball} = T_{diff} C'_2. \quad (D2.27)$$

We now multiply (D2.26) and (D2.27) before taking the square root such that the resulting value scales linearly with α and T_{diff} :

$$\sqrt{\left(\frac{P_{OPC}}{P_{norm}} - T_{ball} \right) (T_{meas} - T_{ball})} = \frac{\alpha}{\alpha_0} T_{diff} \sqrt{C'_2 C'_3}. \quad (D2.28)$$

Our equation for the TSOPC power reads as follows after substituting (D2.23) into (D2.12):

$$P_{TSOPC} = P_{In} \alpha^2 [T_{ball} + T_{diff} C'_4]^2. \quad (D2.29)$$

We can determine this value by multiplying (D2.28) by $X \equiv C'_4 / \sqrt{C'_2 C'_3}$, adding T_{ball} and taking the square:

$$\begin{aligned}
\left[T_{ball} + X \sqrt{\left(\frac{P_{OPC}}{P_{norm}} - T_{ball} \right) (T_{meas} - T_{ball})} \right]^2 &= \left[T_{ball} + \frac{\alpha}{\alpha_0} T_d C'_4 \right]^2 \\
&\approx [T_{ball} + T_d C'_4]^2 \quad . \quad (D2.30) \\
&= \frac{P_{TSOPC}}{\alpha^2 P_{In}} = \frac{P_{TSOPC}}{P_{norm}}
\end{aligned}$$

The left hand side of this equation is fit to our data in Chapter 8, and the value of X is fit. X scales the contribution of the diffuse light based on the various aperture functions described in this derivation. If the aperture of the PCM is sharp, then C'_3 and C'_4 are equal. In this case, X^2 is the ratio of the active area of the PCM to the active area of the photodetector.